Photon Factory Activity Report 2001 #19B
–Users' Report–

136 Ultrasonic effect for the acceleration of polymorphic crystallization of fats
Satoru UENO, Morio TAKEUCHI, Jun-ichi SAKATA, Yoshinobu NOZUE, Yoshiyuki AMEMIYA, Kiyotaka SATO
15A/2000G066

137 EXAFS studies of the formation mechanisms of metal clusters in micelles of surfactants
Masafumi HARADA, Takashi YAMAMOTO, Tsunehiro TANAKA
7C,10B,12C/2000G076

138 EXAFS study on the spin crossover complex film, [Fe(II)(R-trz)$_3$]-Nafion
Akio NAKAMOTO, Yuuki ONO, Daiju MATSUMURA, Toshihiko YOKOYAMA, Norimichi KOJIMA
10B/2000G081

139 EXAFS study of reduced $Ce_{1-x}Ln_xO_{2.00-y}$(Ln=Y,Sm,Gd and Yb)(III)
Tsuneo MATSUI, Yuji ARITA, Satoshi YAMAZAKI, Hiroyuki KONISHI, Katsumi KOBAYASHI
27B,9A/2000G086

140 Polymorphism of syndiotactic polystyrene from the molten state observed by the simultaneous DSC-XRD
Hirohisa YOSHIDA, Takafumi WATANABE, Tomoko YOSHII, Gongzheng ZHANG
10C/2000G100

141 Local structure of solid and molten strontium dichloride
Yoshihiro OKAMOTO, Tsuyoshi YAITA, Haruhiko MOTOHASHI, Katsumi KOBAYASHI, Noriko USAMI
27B/2000G105

142 Time resolved simultaneous SAXS/DSC study on oil crystallization in O/W monodispersed emulsion
Naohiko KAWASAKI, Satoru UENO, Mitsutoshi NAKAJIMA, Atsuo IIDA, Yoshiyuki AMEMIYA
4A,15A/2000G159

143 Investigation of Ni magnetic moment in Ni_2Gd Laves phase through MCP
Kazuo YANO, Yoshikazu TANAKA, Isao MATSUMOTO, Hiromichi ADACHI, Izuru UMEHARA, Hiroshi KAWATA
NE1/2000G169

144 The influence of copper addition on the phase decomposition in Al-Zn-Mg-Cu-Mn alloys
Hiroki ADACHI, Junya ISOGAI, Kozo OSAMURA
15A/2000G204

145 Analysis of crystal structure for bismuth layer-structured oxides
Yuji NOGUCHI, Masaru MIYAYAMA, Tetsuichi KUDO
4B2/2000G215

146 Structural study of transition metal chalcogenide nanoclusters confined in the zeolite cages
Kenji MARUYAMA, Makoto YAMAZAKI, Yuji KUROGOUCHI, Hideoki HOSHINO, Takefumi MIYANAGA
10B/2000G238

147 Structural study of NIPA/SA gel with low water content
Masaaki SUGIYAMA, Masahiko ANNAKA, Kazuhiro HARA
10C/2000G242

148 Structural analysis of C14-type Laves $TiMn_2$ alloy by XAFS
Naoya MASAHASHI, Satoshi SEMBOSHI, Masaki SAKURAI, Shuji HANADA
12C/2000G246

149 EXAFS study of liquid Se-Te mixture
Takafumi MIYANAGAI, Hideoki HOSHINO, Hiroyuki IKEMOTO, Hirohisa ENDO
10B/2000G253

150 Mn and Fe K-edges XAFS study of Sn added Mn-Zn ferrite
Masahiro OISHI, Keiichi FUKUDA, Yasuko TERADA, Izumi NAKAI
12C/2000G255

151 Population of 5-fold coordinated Ti in mesoporous titania
Hideaki YOSHITAKE, Tae SUGIHARA, Yasuhide GOA, Takashi TATSUMI
9A/2000G269

152 Dynamic layer response of electroclinic effect in ferroelectric liquid crystals by time resolved X-ray micro-diffraction
Yumiko TAKAHASHI, Atsuo IIDA, Yoichi TAKANISHI, Michi NAKATA, Megumi TOSHIMITSU, Ken ISHIKAWA, Hideo TAKEZOE
4A/2000G279

153 EXAFS study on local structure of Fe in nano-structured Al alloy
Masaki SAKURAI, Eiichiro MATSUBARA, Makoto MATSUURA, Kazuhiko KITA, Hiroyuki SASAKI, Junichi NAGAHORA
12C/2000G287

154 Dynamic and static disorder of alkali halide solid solutions studied by temperature-dependent extended X-ray-absorption fine structure
Manabu KIGUCHI, Koichiro SAIKI, Atsushi KOMA
12C/2000G288

155 Co 2p x-ray absorption spectrum of $LaCoO_3$
Yukihiro TAGUCHI, Kojiro MIMURA, Yoshinao OKABAYASHI, Katsuyuki KITAMOTO, Yoko WATANABE, Kouichi ICHIKAWA, Shuichi KAWAMATA, Osamu AITA
19B/2001G011

156 Rocking curves of iron borate single crystal in rf magnetic field
Takaya MITSUI, Yasuhiko IMAI
14B/2001G031

157 An order-disorder phase transition in Al-Ni-Co decagonal quasicrystals by anomalous-X-ray scattering
Hiroshi ABE, Yoshie MATSUO, Ken-ichi OHSHIMA, Hiroyuki SAITOH, Hironori NAKAO
4C/2001G036

158 K emission spectra of lanthanide compounds
Masaaki HARADA, Kenji SAKURAI
14A/2001G045

159 Recipe for SR Laue topography of protein crystals
Haruhiko KOIZUMI, Takashi UCHIDA, Mitsunori ISHIMOTO, Miki SHIMIZU, Takashi ANEZAKI, Natsuko AOTA, Satoshi KURITA, Ken-ichi KOBAYASHI, Masaru TACHIBANA, Kenichi KOJIMA
15B1/2001G062

160 Pressure effect on the magnetism and structure of a spin-Peierls substance:MEM-$\{TCNQ\}_2$
Kouji EJIMA, Takayuyki TAJIRI, Hiroyuki DEGUCHI, Masaki MITO, Seishi TAKAGI, Kenji OHWADA, Hironori NAKAO, Youichi MURAKAMI
1B/2001G064

161 Charge-density distribution in calcium titanate perovskite $CaTiO_3$
Masatomo YASHIMA
4B2/2001G070

162 Recovery of x-ray energy responses of neutron irradiated semiconductors
Junko KOHAGURA, Teruji CHO, Mafumi HIRATA, Tomoharu NUMAKURA, Ryutaro MINAMI, Hiroyuki WATANABE, Maiko YOSHIDA, Hirokazu ITO, Kiyoshi YATSU, Syoichi MIYOSHI, Junichi HORI, Takashi KONDOH, Takeo NISHITANI, Keiichi HIRANO, Hideki MAEZAWA
15C/2001G071

163 Crystallization process of poly(ε-caprolactone)-*block*-polybutadiene in a spherical microdomain structure
Satoshi TANIMOTO, Shintaro SASAKI, Shuichi NOJIMA
10C/2001G076

164 Ti K-edgeEXAFS on the local structural change of $PbTiO_3$
Takafumi MIYANAGA, Kei SATO, Shigenobu MATSUDA, Djibril DIOP
9A/2001G087

165 Local structure around non-crystallized transition metals incorporated in hydroxyapatites
Shigeru SUGIYAMA, Takuya ICHII, Tomotaka SHONO, Masayoshi FUJISAWA, Daisaku MAKINO, Toshihiro MORIGA, Hiromu HAYASHI
9A,10B/2001G090

166 Structural analysis of Noble metal nanoparticles under supercritical conditions by means of EXAFS

Masafumi HARADA, Yoshifumi KIMURA, Tsutomu OHMORI

7C,10B,12C/2001G099

167 XAFS characteristion of PtIn catalysts supported on activated carbon

Diego CAZORLA, M.Carmen ROMÁN, Juan A. MACIÁ, Hiromi YAMASHITA, Yuichi ICHIHASHI, Masakazu ANPO

9A,7C/2001G119

168 Arsenate-iron complex in the pore of functionalized MCM-41

Hideaki YOSHITAKE, Toshiyuki YOKOI, Takashi TATSUMI

12C,10B/2001G133

169 Morphology and compositional distribution of Cu-Zn growing electrodeposits

Hiromi EBA, Kenji SAKURAI

4A/2001G144

170 Magnetic EXAFS for Ni-Mn alloys

Takafumi MIYANAGA, Teiko OKAZAKI, Ryota MARUKO, SHin-ichi NAGAMATSU, Takashi FUJIKAWA

28B/2001G232

171 High-pressure x-ray diffraction study on $Pr_{0.65}Ca_{0.35}MnO_3$

Susumu SHIMOMURA, Kengo NISHIMOTO, Tetsuji OGATA, Yasushi YAMANAKA, Yoshiaki NAITO, Keisuke TAJIMA, Nobuyoshi WAKABAYASHI, Ryoko TAZAKI, Hiroshi SAWA, Hironori NAKAO, Yasuhide TOMIOKA, Yoshinori TOKURA

1B/2001G245

172 X-ray fluorescence holography of Nd_2CuO_4

Kouichi HAYASHI, Yukio TAKAHASHI, Ei-ichiro MATSUBARA, Takehara MORI, Masahiko TANAKA, Hirotaka YAMAGUCHI

3A/2001G246

173 Study on crystallization and spherulite growth of poly(ethylene) in phase-separated polymer blends

Shinichi SAKURAI, Kyoko HAYASHI, Shigeo HARA, Katsuhiro YAMAMOTO, Shigeru OKAMOTO

9C,15A/2001G269

174 Structural analysis of a thin film of an SEBS triblock copolymer forming spherical microdomains

Shinichi SAKURAI, Akiko SAKAMOTO, Shigeru OKAMOTO

9C,10C/2001G270

175 Effective pair potentials of molten CuI estimated from the experimental partial structure factors

Pavlin D. MITEV, Masatoshi SAITO, Kazumasa SUGIYAMA, Yoshio WASEDA

7C/2001G273

176 Local structure around Si atoms in GeSi alloy semiconductors

Ichiro YONENAGA, Masaki SAKURAI

11B/2001G274

177 Time-resolved small- and wide-angle X-ray scattering studies on structure formation in crystalline grat copolymers

Katsuhiro YAMAMOTO, Shigeru OKAMOTO, Kenji NAGATA, Shin-ichi SAKURAI, Shigeo HARA, Yusuke SUGINO, Masashi MOURI

9C,15A/2001G275

178 Structural development of sodium-form gellan gum gels on cooling

Yuji JINBO, Yusaku SUGIURA, Hisanori WATANABE, Hideto NIWA, Katsumi WATANABE, Yoshinobu IZUMI

10C/2001G279

179 Local structure of Lu doped in high creep resistant Al_2O_3

Masaki SAKURAI, Eiichiro MATSUBARA, Hideo YOSHIDA, Yuichi IKUHARA, Taketo SAKUMA

12C/2001G281

180 A grazing-incidence SAS measurement of Ge Islands capped with Si
Hiroshi OKUDA, Shojiro OCHIAI, Yoshiyuki AMEMIYA
15A/2001G285

181 Conformation of humic acids from soils of different age studied by synchrotron X-ray scattering
Alexander TIMCHENKO, Igor SERDYUK, Kazumoto KIMURA, Hiroshi KIHARA, Rudolf OBERTHUR
15A1/2001G302

182 EXAFS studies on the sprayed Pt catalyst prepared from PVP-stabilized colloid
Nobuyuki ICHIKUNI, Yasuko TAKAGI, Shogo SHIMAZU, Takayoshi UEMATSU
10B/2001G321

183 Effective pair potentials in $BaTiO_3$, $PbTiO_3$ and related perovskite-type compounds
Akira YOSHIASA, Maki OKUBE, Hiroki OKUDERA, Masatomo YASHIMA, Roushown ALI, Kazumasa NAKAMURA, Atsushi SAKAI, Mizuki MORI
9A/2001G322

184 Ion beam irradiation effects of oxide thin films formed by oxygen cluster ion beam assisted deposition
Yutaka SHIMIZUGAWA, Jiro MATSUO, Toshio SEKI, Tatsuya ASANUMA, Kohei KADONO, Tomonari TAKEUCHI, Hiroyuki KAGEYAMA
7C,9A/2001G326

185 *In situ* XAFS study on molybdenum oxide catalysts supported on zirconia by moten salt preparation
Nobuyuki MATSUBAYASHI, Motoyasu IMAMURA, Koichi SATO, Tomoaki TANAKA, Kyoko K. BANDO, Hiromichi SHIMADA, Pavel AFANASIEV, Christophe GEANTET
7C,10B/2001G327

186 Structure of bicelle formed by mixed surfactants
Kenji KUBOTA, Kousirou TAYA, Rio KITA, Kenji OCHIAI, Kaori WAKAMATSU
10C/2001P014

187 Resonant x-ray scattering study on the filled skutterudite $PrFe_4P_{12}$
Kenji ISHII, Toshiya INAMI, Youichi MURAKAMI, Lijie Hao, Kazuaki IWASA, Masahumi KOHGI, Yuji AOKI, Hitoshi SUGAWARA, Hideyuki SATO, Shin IMADA, Hironori NAKAO, Yusuke WAKABAYASHI, Hiroshi SAWA
4C,16A2/2001S2-002

188 Resonant X-ray studies of orbital ordering systems
Youichi MURAKAMI, Hironori NAKAO, Takeshi MATSUMURA, Kazuma HIROTA, Yusuke WAKABAYASHI, Hiroshi SAWA, Hiroyuki OHSUMI, Masato KUBOTA, Takahisa ARIMA, Makoto IZUMI, Yasujiro TAGUCHI, Yoshinori TOKURA, Fumitoshi IGA
4C,16A2/2001S2-002

189 Stress measurement of tetragonal $Pb(Zr_{1-x}Ti_x)O_3$ thin films grown on Pt electrode
Kenji NOMURA, Naoki AWAJI
17A,17C/2001Y003

190 Anisotropy of substructure in secondary recrystallized grain in 3%Si-Fe
Yoshiyuki USHIGAMI, Shuich NAKAMURA, Noriaki OTA, Masao KIMURA
15B/2001C001

191 $Fe(O,OH)_6$ network nanostructure of rusts formed on weathering steel
Masao KIMURA, Tamaki SUZUKI, Hiroshi KIHIRA
12C/2001C001

192 *In-situ* observation of heat/draw deformation behavior of *isotactic* polypropylenes by SAXS measurements
Takashi SAKURAI, Tatsuya KASAHARA, Noboru YAMAGUCHI, Kohji TASHIRO, Yoshiyuki AMEMIYA
15A/2001C006

▶*Surface and Interface*

9A/1999G052

Anomalous rapid change of site preference of Ga at the beginning of recombination in the HDDR for $Nd_{12.5}Fe_{bal}Ga_{0.3}Nb_{0.2}B_{6.2}$ magnets

Kazuya KONNO[*1], Makoto MATSUURA[1], Kaku ASADA[1], Nobuyuki IKUTA[1], Masaki SAKURAI[2]
[1]Miyagi National College of Technology, Natori, Miyagi 981-1239, Japan
[2]Institute for Materials Research, Katahira-chyo, Sendai, Miyagi 980-8577, Japan

Introduction

Recently, Mishima et al. developed the HDDR process with a slow reaction rate, i.e. dynamic HDDR (d-HDDR) [1]. They reported that the addition of nearly 0.3% Ga and 0.2% Nb in $Nd_{12.5}Fe_{bal}B_{6.2}$ increased $(BH)_{max}$ about 40% by using d-HDDR. In order to know the role of Ga in the HDDR process precisely, we carried out XAFS measurements of the Ga K edge for the samples at the various recombination stages: 0, 1, 1.5, 2, and 6 min after the start of dehydrogenation.

Experiment

An ingot of $Nd_{12.5}Fe_{bal}Ga_{0.3}Nb_{0.2}B_{6.2}$ alloys was prepared by arc melting under Ar gas atmosphere, subsequently homogenized in Ar gas at 1140ºC for 40h. Hydrogenation is done under 0.1MPa hydrogen at R.T. for the homogenized sample. Disproportionation is carried out under the low hydrogen pressure of 0.03MPa at 820ºC for the slow decomposition reaction. The recombination is done at 820ºC for 0, 1, 1.5, 2, and 6 min under the relatively higher hydrogen pressure of 3 kPa in order to proceed at a low reaction rate. Results of the X-ray diffraction using Cu Ka radiation show the existence of three phases of α-Fe, NdH_2, and Fe_2B for the disproportionated sample as shown Fig. 1, and the disproportionated state was preserved until about 2 min after the start of the dehydrogenation.

XAFS measurements of the Ga K edge were carried out at the temperature 20 K at BL9A by fluorescence method. Incident energy was selected by a double Si(111).

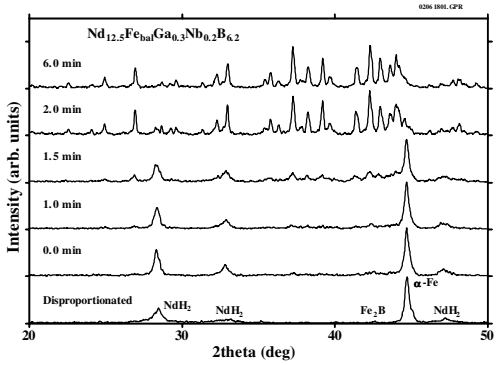

Fig. 1. X-ray diffraction patterns for the disproportionated state and the 0, 1, 1.5, 2, and 6 min after the start of dehydrogenation of $Nd_{12.5}Fe_{bal}Ga_{0.3}Nb_{0.2}B_{6.2}$.

Results and Analysis

After the usual background subtraction and normalization χ(k) was deduced using program AUTOBK. Fig. 2 shows the observed χ(k) curves (solid line) for the Ga K edge of the $Nd_{12.5}Fe_{bal}Ga_{0.3}Nb_{0.2}B_{6.2}$ for the disproportionated state and the various recombination stages. Fitting calculations to these observed XAFS curves were done using FEFFIT program. The best fitting was obtained by putting Ga at α-Fe for the disproportionated and Fe(4c) site in $Nd_2Fe_{14}B$ structure for the recombined state, respectively.

The most significant future of these XAFS results is that as soon as the recombination starts (0 min), XAFS spectrum changes abruptly from those for the disproportionated state to that for the fully recombined state (6 min). This seems very strange because it takes at least 2min. until recombined $Nd_2Fe_{14}B$ structure appears in the X-ray diffraction results (see Fig.1). This result suggests that the portion of α-Fe in which Ga includes preferentially recombined to $Nd_2Fe_{14}B$ at the early stage of recombination.

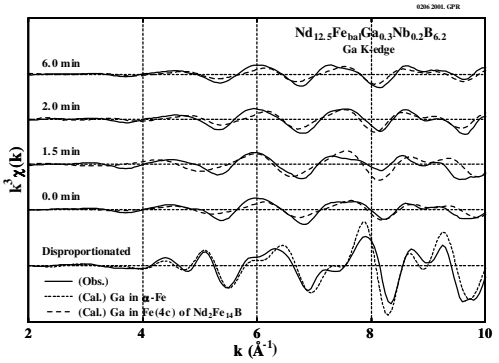

Fig. 2. XAFS spectra of the Ga K edge of $Nd_{12.5}Fe_{bal}Ga_{0.3}Nb_{0.2}B_{6.2}$ for the disproportionated state and the various recombination states (0, 1.5, 2, and 6 min after the start of the dehydrogenation). The solid lines are the observed results, and the broken lines the calculated ones for Ga in α-Fe (at the disproportionated) and in the Fe(4c) site of $Nd_2Fe_{14}B$ (at the 0, 1.5, 2, and 6 min).

References

[1] C. Mishima, M. Hamada, H. Mitarai, and Y. Honkura, proceedings of the 16th International Workshop on R. E. Magnets and Their Applications, Sendai Japan, 873 (2000).

* kazuya@miyagi-ct.ac.jp

14A/1999G190

Structural solution of a new mesoporous $Rb_3Ta_5O_{14}$ phase

Douglas DU BOULAY[1], Katsumi SUDA[1], Nobuo ISHIZAWA*[1]
[1]Materials and Structures laboratory, Tokyo Institute of Technology 4259 Nagatsuta, Midori-Ku, Yokohama 226-8503, Japan

Introduction

In exploring the Ca-Rb-Ta-O phase diagram and attempting to grow new four layered members of the technologically interesting $Rb_2Ca_2Ta_4O_{13}$ perovskite family, a new structural phase was encountered. Initial XRF and EDAX analyses indicated only Rb and Ta components. Single crystal synchrotron X-ray data using BL-14A [1] was measured for the new compound at 0.85Å wavelength, chosen to avoid the 0.81Å Rb absorption edge [2]. Our use of the synchrotron was essential because only a few crystals smaller than 0.05^3 mm^3 were of suitable quality for study. The Diff14A Software [3] was used to drive the horizontal-type 4-circle diffractometer and an eight channel avalanche photodiode detector was used for photon counting [4].

The $Rb_3Ta_5O_{14}$ structure was solved from a half sphere of reflection data using SHELXS97 [5]. Subsequent refinement was done with Xtal3.7 [6]. Absorption coefficients [2] and anomalous dispersion coefficients [7] were taken from the tables of Sasaki. The results have been published [8].

Structure

$Rb_3Ta_5O_{14}$ is a mesoporous material comprised of a network of six distinct TaO_6 octahedra and one TaO_5 trigonal bipyramid which delimit the boundaries of three large Rb filled cavities, as well as the channels that link them. The Ta-O framework appears laminar and consists of two six-membered and one eight membered pyrochlore-like ring system, as indicated in Figure 1. These layers are stacked with a small offset leading to orthorhombic Pnma symmetry and dimensions a=7.3677(3), b=14.7904(19) and c=25.379(3)Å.

The structure refined well with wR=0.047 but large residual densities were observed for two of the four Rb atoms and all four exhibit very large vibrational motion. This suggests that some degree of static or dynamic disorder is associated, could be associated with their coordinating environment. If the Rb atom disorder is static then it may be that the m-symmetry is broken.

The Rb atom environments also appear unusual in that there are chains of Rb-Rb contacts extending through the structural cavities and channels. These have contacts in the range 3.5-4.1Å, significantly shorter than the 4.95Å Rb-Rb bonds in metallic (bcc) Rb. This suggests that the chains of Rb atoms in this lattice might behave as one dimensional wires, perhaps exhibiting some unusual conduction properties.

The mesoporous lattice could also be amenable to Li ion replacement, providing a solid electrolyte matrix within which Li ions could be re and de-intercalated as conduction ions.

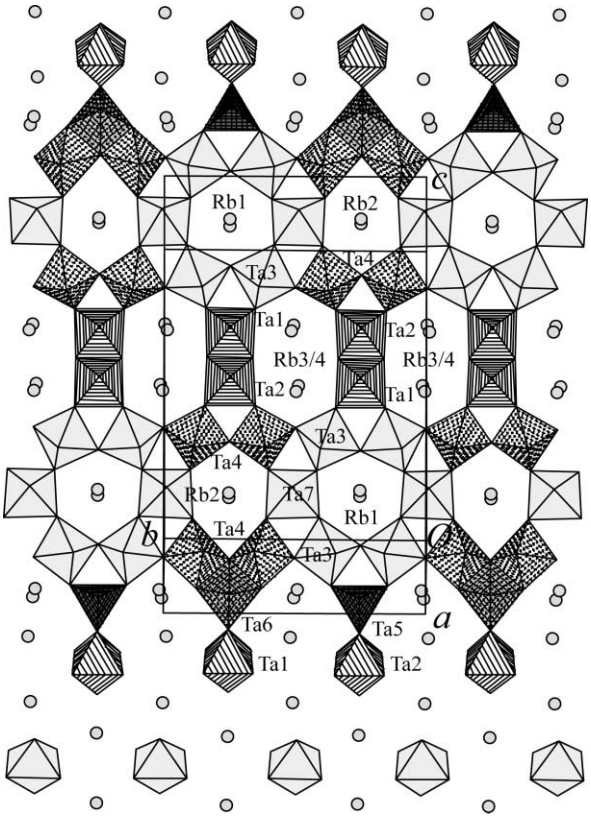

Fig. 1 Pyrhochlore like layering in $Rb_3Ta_5O_{14}$

References

[1] Y. Satow & Y. Iitaka, Rev. Sci. Instrum. **60**, 2390 (1989).
[2] S. Sasaki, KEK Report 5-24 (1989).
[3] T.P. Vaalsta & J.R. Hester Diff14A Software.
[4] S. Kishimoto et al., Rev. Sci. Instrum. **69**, 384 (1998).
[5] G.M. Sheldrick SHELXS97 Gottingen, Germany (1997)
[6] Hall et al., Xtal3.7 http://xtal.crystal.uwa.edu.au/ (2000)
[7] S. Sasaki, KEK Report 7-26 (1990).
[8] D. du Boulay et al., Acta. Cryst., **C58**, i40 (2002).

* nishizaw@n.cc.titech.ac.jp

3A/1999G208

Crystal structure of spinel type compound $CuIr_2S_4$ at low temperatures

Hiroki ISHIBASHI*
Osaka Prefecture Univ., Gakuen-cho, Sakai, Osaka 599-8531, Japan
Rutgers Univ., Piscataway, NJ 08854, USA

Introduction

A spinel-type compound $CuIr_2S_4$ is known to show a metal-insulator transition (MIT) at T = 226 K, which is accompanied by a structural transition[1]. This transition is considered to be due to charge ordering of Ir^{3+} and Ir^{4+} ions at low temperatures. Further, the local magnetic moment of Ir^{4+} (S = 1/2) vanishes at low temperature simultaneously, which is suggested to make spin dimerization of the Ir^{4+} ions. However, the detailed structure such as the atomic position of Ir has not been determined except for the symmetry [2]. It is important to clarify the crystal structure in order to make the mechanism of the MIT clear. In the present study, the structural analysis is performed for the low temperature phase of $CuIr_2S_4$.

Experimental

The $CuIr_2S_4$ sample was prepared by heating the mixture of high purity Cu, Ir and S powder in evacuated quartz tube. The powder diffraction experiment at 50 K was performed using high-resolution diffractometer installed at a beam line of BL-3A station. A wavelength of incident beam used was 1.5470 Å. A flat Si(111) crystal analyzer was used in order to obtain the data with high angular resolution. The powder pattern was collected in the angular range of $15° < 2\theta < 57°$ in $2\theta/\theta$ step scanning with a step width of 0.004° in 2θ and a counting time of 4 s at each step. The Rietveld refinements were carried out using the program GSAS.

Results and Discussion

The low temperature phase of $CuIr_2S_4$ has a triclinic symmetry as reported previously[2]. The refined lattice constants are a = 11.92776(9) Å, b = 6.98016(8) Å, c = 11.92776(9) Å, α = 91.0550(7)°, β = 108.4672(6)° and γ = 91.0320(7)°. There are eight independent Ir sites in the unit cell if the space group P-1 is assumed. Table 1 shows the atomic position of Ir atoms. For this structural model, all reflections including superlattice and forbidden peaks can be indexed. Table 2 shows the atomic distances between Ir and Ir atoms. From table 2, there are two pairs whose atomic distances are shorter than the others, i.e., Ir1-Ir4 and Ir2-Ir3. If we assume that Ir1, Ir2, Ir3 and Ir4 has a valence +4 and that the pairs of Ir1-Ir4 and Ir2-Ir3 are dimerized, we can explain the physical properties of $CuIr_2S_4$ at low temperatures; The MIT is caused by the charge ordering of Ir^{3+} (S = 0) and Ir^{4+} (S = 1/2) and the vanishing the local magnetic moment of Ir^{4+} is due to spin dimerization of Ir^{4+}. The charge-ordering pattern for both Ir^{3+} and Ir^{4+} forms octamers with isomorphic $Ir^{3+}{}_8S_{24}$ and $Ir^{4+}{}_8S_{24}$. The direction of the dimerization is along [110] or [-110] for pseudo-cubic notation. This result indicates that $CuIr_2S_4$ shows a simultaneous charge-ordering and spin-dimerization. Not only this phenomena but the charge-ordering pattern is unique and this pattern provides a new way to look at the spinel structure. The detail of the above results is reported in elsewhere[3].

Table 1: Atomic position of Ir

	x	y	z
Ir1	0.2336(4)	0.0106(6)	0.7530(4)
Ir2	0.2483(4)	0.0204(6)	0.2330(4)
Ir3	0.2499(4)	0.2296(6)	0.0158(4)
Ir4	0.0111(4)	0.2177(6)	0.7557(4)
Ir5	0.2460(5)	0.5021(6)	0.7497(4)
Ir6	0.2498(4)	0.5181(6)	0.2483(5)
Ir7	0.5080(4)	0.2403(6)	0.2519(4)
Ir8	0.7551(5)	0.2335(8)	0.5022(4)

Table 2: bond length of Ir-Ir

Ir1-Ir3	3.464(7)	Ir5-Ir7	3.478(7)
Ir1-Ir4	3.012(5)	Ir5-Ir8	3.493(5)
Ir2-Ir3	2.956(5)	Ir6-Ir7	3.602(5)
Ir2-Ir4	3.582(7)	Ir6-Ir8	3.487(7)
Ir3-Ir4	3.490(8)	Ir7-Ir8	3.470(9)
Ir1-Ir5	3.551(7)	Ir2-Ir8	3.605(7)
Ir1-Ir5	3.437(7)	Ir3-Ir5	3.658(5)
Ir1-Ir7	3.540(7)	Ir3-Ir6	3.458(8)
Ir1-Ir8	3.554(7)	Ir3-Ir7	3.458(7)
Ir2-Ir6	3.507(6)	Ir4-Ir5	3.486(7)
Ir2-Ir6	3.483(6)	Ir4-Ir6	3.581(5)
Ir2-Ir7	3.432(7)	Ir4-Ir8	3.554(8)

This work was done in collaboration with P. G. Radaelli, Y.Horibe, M. J. Gutmann, C. H. Chen, R. M. Ibberson, Y. Koyama, Y-S. Hor, V. Kiryukhin and S-W. Cheong .

References

1) T. Furubayashi et al, J. Phys. Soc. Jpn., 63, 3333 (1994)
2) H. Ishibashi et al, J. Mag. Mag. Mater. 226-230, 233 (2001)
3) P. G. Radaelli et al, Nature 416, 155 (2002)

* hiroki@ms.cias.osakafu-u.ac.jp

3A/99G272, 2001G070

High-resolution synchrotron X-ray powder diffraction study of the orthorhombic-tetragonal phase transition in $La_{0.64}Ti_{0.92}Nb_{0.08}O_3$

Mizuki MORI, Masatomo YASHIMA*, Rowshown ALI, Atsushi SAKAI,
Masahiko TANAKA[1], Takeharu MORI[1], and Satoshi SASAKI[2]

Department of Materials Science and Engineering, Interdisciplinary Graduate School of Science and Engineering, Tokyo Institute of Technology, 4259 Nagatsuta-cho, Midori-ku, Yokohama, 226-8502, Japan
[1]Photon Factory, High Energy Accelerator Research Organization, Oho, Tsukuba, Ibaraki 305-0801, Japan
[2]Materials and Structures Laboratory, Tokyo Institute of Technology, 4259 Nagatsuta-cho, Midori-ku, Yokohama, 226-8503, Japan

Introduction

Doped $La_{2/3}TiO_3$ compounds have perovskite-type structure and exhibit electrical and dielectrical properties. Thermal expansion and temperature dependence of lattice parameters are important factors in designing the components of solid oxide fuel cells. Conventional X-ray diffractometer produces double wavelengths of $K\alpha_1$+$K\alpha_2$, and broad diffraction peaks with asymmetric shape, which lead inaccuracy in determining the peak positions and thus lattice parameters. Here, we have used synchrotron X-ray powder diffraction technique, having higher angular resolution and simple peak shape (no $K\alpha_2$ peak), compared with conventional X-ray diffractometry, to determine precise lattice parameters of $La_{0.64}Ti_{0.92}Nb_{0.08}O_3$ as a function of temperature and to investigate the phase transition temperature.

Experiments

The synchrotron X-ray diffraction data were collected using beam line BL-3A installed at Photon Factory, KEK, Tsukuba. The wavelength was determined to be λ=1.38010(4) Å after the calibration with NIST CeO_2 sample (a=5.41129 Å). Experimental conditions were: step interval = 0.004˚ and counting time = 10 or 20s. The 004, 020 and 200 reflections were monitored. Peak positions were determined using a profile fitting program *PRO-FIT* (Toraya 1986).

Results and discussion

Peak splitting between orthorhombic 020 and 200 reflections was clearly observed at lower temperatures but it merged at higher temperatures (Fig. 1). With increasing temperature 020 and 200 peaks approached and became single between 355˚ and 388˚C. Although near the transition temperature these two peaks seemed single, but up to 355˚C the profile was able to be decomposed into 020 and 200 peaks successfully.

Figure 2 shows the temperature dependence of lattice parameters of $La_{0.64}Ti_{0.92}Nb_{0.08}O_3$ compound. With increasing temperature, a and c/2 parameters increased considerably compared with b parameter, resulting that a and b parameters coincided above 355˚C, indicating that the orthorhombic phase transformed to tetragonal symmetry. (1) The lattice parameters increased continuously, while b/a ratio decreased continuously with temperature and became unity at the orthorhombic-tetragonal transition point. (2) Good agreement was obtained in the lattice parameter values between heating and cooling. These results of (1) and (2) indicate that the orthorhombic-tetragonal phase transition is continuous.

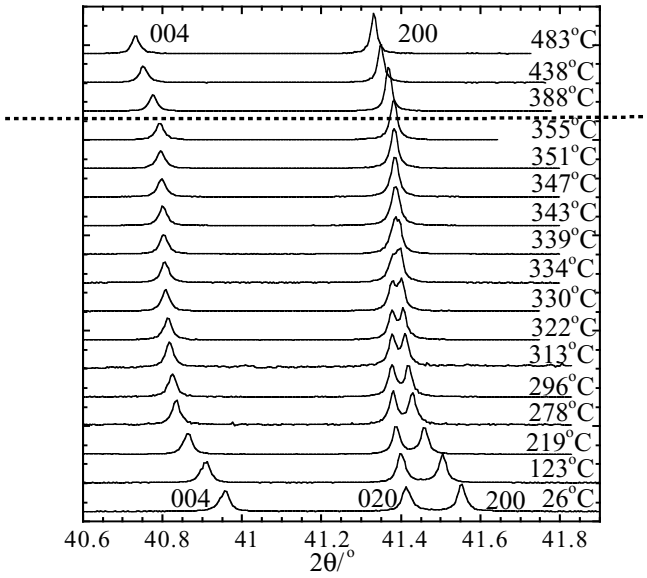

Fig.1. Temperature dependence of 004, 020 and 200 peak profiles of $La_{0.64}Ti_{0.92}Nb_{0.08}O_3$.

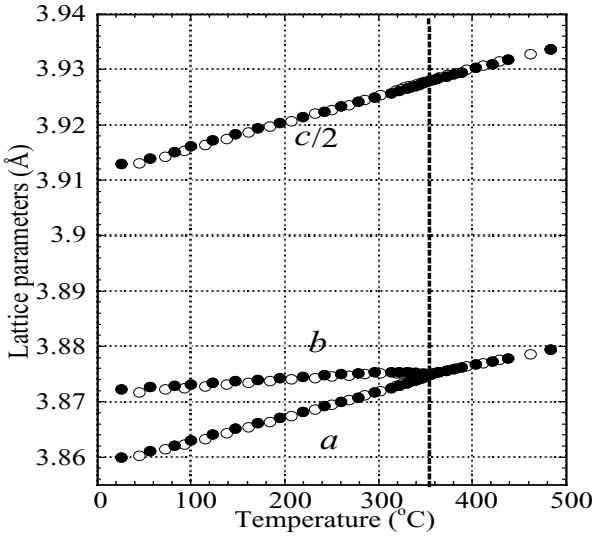

Fig.2. Temperature dependence of lattice parameters of $La_{0.64}Ti_{0.92}Nb_{0.08}O_3$. Filled and open circles denote heating and cooling data, respectively.

* yashima@materia.titech.ac.jp

3A/1999G272, 2001G070

High-temperature synchrotron X-ray powder diffraction study of the orthorhombic-tetragonal phase transition in lanthanum titanate perovskite $La_{0.68}(Ti_{0.95},Al_{0.05})O_3$

Masatomo YASHIMA*, Roushown ALI, Masahiko TANAKA[1], Takeharu MORI[1]
Department of Materials Science and Engineering, Interdisciplinary Graduate School of Science and Engineering, Tokyo Institute of Technology, 4259 Nagatsuta-cho, Midori-ku, Yokohama, 226-8502, Japan
[1]Photon Factory, High Energy Accelerator Research Organization, Oho, Tsukuba, Ibaraki 305-0801, Japan

Introduction

Doped $La_{2/3}TiO_3$ compounds have double perovskite-type structure and exhibit excellent electrical and dielectric properties. Thermal expansion and temperature dependence of lattice parameters are important factors in designing the components of solid oxide fuel cells. Conventional X-ray diffractometer produces double wavelengths of $K\alpha_1$+$K\alpha_2$, and broad diffraction peaks with asymmetric shape, which lead inaccuracy in determining the peak positions and thus lattice parameters. Here, we have used synchrotron X-ray diffraction technique, having higher angular resolution and simple peak shape (no $K\alpha_2$ peak) compared with conventional X-ray diffractometry, to determine precise lattice parameters of $La_{0.68}(Ti_{0.95},Al_{0.05})O_3$ as a function of temperature and to investigate the phase transition temperature.

Experiments

To obtain higher angular resolution as possible with good counting statistics, we performed synchrotron X-ray powder diffraction experiments for $La_{0.68}(Ti_{0.95},Al_{0.05})O_3$ at the beam line BL-3A at the Photon Factory, High Energy Accelerator Research Organization (KEK), Japan. A monochromatized 1.37852(6) Å X-ray was used for high-temperature diffraction experiments. To improve the angular resolution a Si (111) analyzer crystal was installed between the sample and the scintillation counter. The angular resolution $\Delta d/d$ was estimated to be 0.0002 from the peak width for the standard CeO_2 powders where d is the lattice spacing.

Results and discussion

Figure 1a shows the conventional laboratory-based X-ray powder diffraction profile for 004, 020 and 200 reflections of $La_{0.68}(Ti_{0.95},Al_{0.05})O_3$ measured at 200°C. The splitting into 020 and 200 reflections was not so clear in the conventional diffraction profile. On the contrary, the corresponding split was clear for the synchrotron X-ray powder diffraction profile measured at the same temperature (Fig. 1b). This clear splitting is ascribed to (1) much narrower peak width and to (2) no splitting as $K_{\alpha1}$ and $K_{\alpha2}$. The full width at half maximum for 020 synchrotron X-ray diffraction peak 0.0209(6) deg. was much narrower than that obtained by the conventional diffractometer, 0.119(5) deg. Therefore, the resultant unit-cell parameters estimated by the synchrotron diffraction technique had smaller error bars: a=3.85926(3), b=3.87045(4) and c=7.77595(5) Å, comparing with those by the conventional diffractometer: a=3.8600(2), b=3.8711(1) and c=7.7731(2) Å. These results indicate that the present synchrotron X-ray powder diffraction technique is very powerful to decompose the peaks with very small difference in peak positions, compared with the conventional laboratory-based X-ray powder diffraction method. The unit-cell parameters a, b and c increased with an increase of temperature. Unit-cell parameter a increased considerably compared with b parameter, resulting that these two parameters became closer continuously with an increase of temperature and that coincided at 350 ± 2°C. The c/a ratio was almost independent of temperature, while the b/a decreased continuously with an increase of temperature and became unity at 350°C. Unit-cell parameters determined from the data measured on heating exhibited fairly good agreements with those measured on cooling. Taking account into the results, (I) Good agreement between the unit-cell parameters obtained from the heating and cooling data, (II) Continuous change in unit-cell parameters with temperature, the orthorhombic-tetragonal phase transition is strongly suggested to be continuous and reversible.

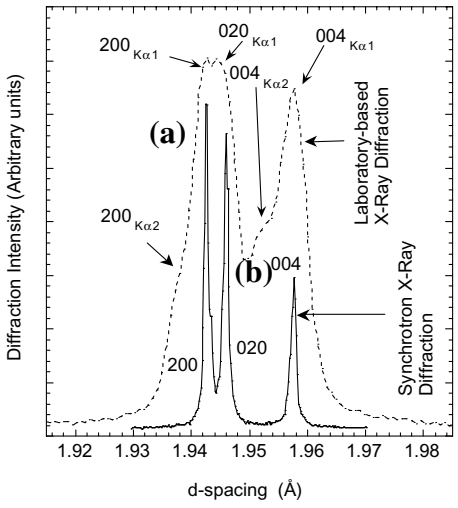

Fig.1. Comparison between synchrotron and conventional X-ray diffraction profile of 004, 020 and 200 reflection peaks of $La_{0.68}(Ti_{0.95}Al_{0.05})O_3$. The lattice spacing d value in the horizontal axis was obtained from the diffraction angle 2θ by using Bragg's equation $\lambda = 2d \sin\theta$ where the values λ =1.54056 Å and λ=1.37852 Å were used for the conventional and synchrotron data, respectively.

* yashima@materia.titech.ac.jp

10B/1999G283

Hydration of Mo species in Mo dispersed in SBA-1

Hideaki YOSHITAKE[1], SungHyun LIM[2], Takashi TATSUMI*[2]
[1]Graduate School of Environment and Information Sciences, Yokohama National University, Yokohama 240-8501, Japan
[2]Graduate School of Engineering, Yokohama National University, Yokohama 240-8501, Japan

Introduction

The working of active atoms during heterogeneous catalytic reactions has been a topic on the supported Mo catalysts. The size of the ensembles depends on the preparation procedure. Direct incorporations of Mo into the framework of mesoporous silica are a technique newly developed. SBA-1 is synthesized in acid conditions, which is favorable to incorporate significant amount of Mo into the silica pores. We study the dispersion of Mo in hydrated and dehydrated states by EXAFS spectroscopy.

Method

Mo-SBA-1 was prepared as follows. An aqueous solution of hexaammonium heptamolybdate (AHM) and tetraethyl orthosilicate (TEOS) was added to an aqueous solution of CTEABr acidified with HCl with stirring vigorously at 273 K. The mixture was kept at 273 K for 4 d. Yellow precipitates were filtered, dried and calcined. The Mo content in Mo-SBA-1 was determined by ICP. Mo/SBA-1 was prepared by impregnating respective mesoporous silicas with an aqueous solution of AHM acidified with HCl, dried, and calcined.

Samples for spectroscopic measurements were pretreated by heating at 673 K in oxygen and evacuation at room temperature. These dehydrated catalysts were transferred into suitable spectroscopic cells without exposure to air. Hydration treatments were conducted in the atmospheric environment, i.e. at 298 K and 50-70 % of humidity. X-ray absorption experiments were carried out in a transmission mode at BL-10B. The data were processed by EXAFS analysis program REX 2000 (Rigaku). k^3–Weighted EXAFS oscillation, $k^3\chi(k)$, in the 35 – 135 nm^{-1} region was Fourier transformed to a radial distribution function. Peak due to Mo-Mo bonds were separately inverse Fourier transformed into k space where the curve fitting analyses were done. The amplitude and phase-shift functions for Mo-Mo were extracted from the spectra of Mo foil.

Results and Discussion

Table 1 shows the coordination number of Mo nearest neighbour in Mo K-edge EXAFS. Comparing under the same preparing conditions, the coordination number is larger in the direct incorporation catalyst than in the impregnation one. For example, dehydrated 6.25 wt % Mo-SBA-1 and Mo/SBA-1 show N(Mo-Mo) = 0.7 and 0.4, respectively. Hydration increases not only r(Mo-Mo) but also N(Mo-Mo) and the degree of the enhancement is larger in the direct incorporation catalyst than in the impregnation one. Mo-Mo bond was not detected in the radial distribution function for dehydrated 1.69 wt % Mo-SBA-1, while it clearly appeared after hydration.

Table 1. Curve fitting results of Mo K-edge EXAFS of Molybdosilicates

condition	catalyst	wt%	N	Mo-Mo r /nm	Dw
dehydrated	Mo-SBA-1	1.06	(0)		
		1.69	(0)		
		3.85	0.6^3	0.324	0.091
		6.25	0.7^3	0.326	0.090
dehydrated	Mo /SBA-1	2.95	(0)		
		6.25	0.4^2	0.327	0.071
hydrated	Mo-SBA-1	1.06	(0)		
		1.69	0.6^2	0.330	0.066
		3.85	1.1^4	0.331	0.064
		6.25	1.4^4	0.331	0.075
hydrated	Mo /SBA-1	2.95	(0)		
		6.25	0.5^2	0.331	0.067

N: coordination number, r: interatomic distance and Dw: relative Debye-Waller factor against that of the reference samples (Dw_{ref} = 0.06). The superscripts of the data are estimated errors. That for r(Mo-Mo) is 0.003 nm.

Hydration likely results in a bridging reaction of MoO_x units on the pore surface such as

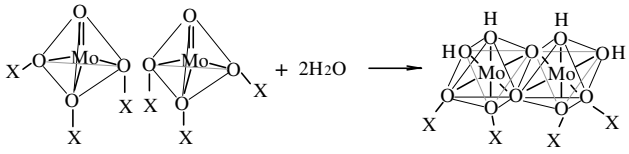

Especially for Mo-SBA-1, the ensemble of MoO_x units remains even without the chemical bond, which implies the possibility of the activation of a molecule by more than two MoO_x units working in a corporation. The lower dispersion by the direct incorporation is likely caused by a partial inclusion AHM molecular ion in the pore wall during hydrothermal synthesis while it is just adsorbed on the pore wall during impregnation.

* ttatsumi@ynu.ac.jp

13C/2000G024

Study on SCN⁻ metal complexes by NEXAFS and resonant photoelectron spectroscopy

Nobuyuki MATSUBAYASHI[*1], Motoyasu IMAMURA[1], Tomoaki TANAKA[1], Hiromi IKEURA-SEKIGUCHI[1], Hiromichi SHIMADA[1]

[1]*National Institute of Advanced Industrial Science and Technology, Tsukuba, Ibaraki 305-8565, Japan*

Introduction

Thiocyanic ion is used as analytical reagent as well as reagent for various synthesis. Its peculiar chemical property is come from three heteroatoms form a linear molecule. To clarify the specific electronic state of SCN^- ion, NEXAFS spectra and resonant photoemission spectra (RPES) of the SCN^- in various salts on S L , N K, C K and the absorption edge of the metal were measured in this research.

Experimental

All the experiments were done at the BL-13C with PHI 1600C. The photoelectron take-off angle was 54.7° relative to the surface normal. The laminar type gratings with a cylindrical surface of 50m-radius grooved 750 l/mm for N K-edge and 350 l/mm for C K-edge were used. The samples were dispersed on Au plate to avoid charging up.

Results and discussion

Figure 1 shows the changes in the valence-band photoemission spectra recorded by changing excitation energy near N K-edge of NaSCN with absorption spectra of the N K-edge by total electron yield. A large enhancement of auger spectra of N KVV with two peaks and one shoulder was observed at 399.6 eV corresponding to π^* transition. The valence peak at 7 eV is also enhanced at the energy. The peak energy did not change at the beginning of increase indicating contribution of photoelectron.

Figure 2 shows the changes in the valence-band photoemission spectra recorded by changing excitation energy near C K-edge of NaSCN with absorption spectra of the C K-edge by total electron yield. The C KVV auger spectra showed an enhanced peak at 287.2 eV corresponding to π^* transition followed an increasing peak corresponding to absorption at σ^* transition with an energy shift as a normal auger peak as increasing excitation energy. The valence peak at 9 eV is also enhanced at the energy. The net peak intensity of Na 2p at 32eV was not affected by resonant effect in both of N K-edge and C K-edge.

Slightly different valence-band photoemission spectra spectra on the absorption edges and metals were observed.

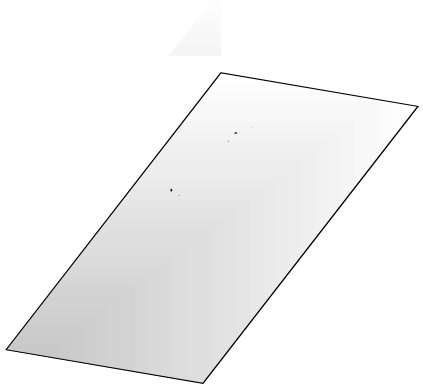

Fig. 1 The valence-band photoemission spectra recorded on N K-edge of NaSCN with absorption spectra of the N K-edge by total electron yield.

Fig.2 The valence-band photoemission spectra recorded on C K-edge of NaSCN with absorption spectra of the C K-edge by total electron yield.

References

[1] N.Matsubayashi, T. Tanaka, M. Imamura, H. Shimada, and T. Saito, *Analitical Sciences*, **17**, i119(2001).

* n-matsubayashi@aist.go.jp

10C, 15A/2000G040

Time-resolved WAXS and SAXS measurements for structural study of crystallization and ferroelectric phase transition of fluorine polymers

Kohji TASHIRO*[1], Seishi SARAGAI[1], Kazunori FUKUDA[1], Sono SASAKI[1], Tatsuya KAWAGUCHI[1], Yayoi YOSHIOKA[1], Katsuhisa HAMA[1], Katsumi KOBAYASHI[2], Kazuki ITO[2], Hironari KAMIKUBO[2], and Yoshiyuki AMEMIYA[3]

[1] Graduate School of Science, Osaka University, Toyonaka, Osaka 560-0043, Japan
[2] High Energy Accelerator Research Organization, Tsukuba, Ibaraki 305, Japan
[3] Faculty of Engineering, the University of Tokyo, Hongo, Bunkyo, Tokyo 113-8656, Japan

Vinylidene fluoride - trifluoroethylene (VDF-TrFE) copolymers exhibit the ferroelectric phase transition between polar low-temperature (LT) phase and nonpolar high-temperature (HT) phase at a Curie transition temperature (Tc). The structural change has been investigated in detail by combining various kinds of techniques [Ferroelectric Polymers: Chemistry, Physics, and Technology (H. S. Nalwa edt.), Marcel Dekker Inc., p.63 (1995)]. But, in order to clarify the transition mechanism in more detail, we need to investigate the kinetics of this phase transition. Then we have carried out the time-resolved measurements of wide-angle X-ray scattering (WAXS) and small-angle X-ray scattering (SAXS) in the course of crystallization and ferroelectric phase transition though the temperature jump from the molten state.

The temperature jump could be made at a rate of 600 –1000°C/min, during which the WAXS and SAXS data were collected every 3 – 10 sec. When the temperature jump was made from the melt to the temperature region of HT phase, the crystallization of the HT phase could be observed clearly as judged from the evolution of the sharp (100) reflection. Half width of the reflection was wide in the earliest stage of crystallization but decreased gradually with a passage of time. At the same time the peak position was found to shift to higher angle direction. On the other hand, when the jump was made to the region of LT phase below Tc, it was confirmed that the reflection of the HT phase appeared at first and then was replaced by the reflection of LT phase. The behavior of the HT reflection was essentially the same with the case of above-mentioned jump to the HT phase, but the reflection of the LT phase was found to be almost constant and quite broad compared with the width of the HT phase reflection. These observations allowed us to speculate the structural change shown in Figure. At first the HT phase is crystallized from the melt, but the crystallite size is small and chain packing is not tight. As the passage of time the crystallite size becomes larger and the chain packing becomes tighter. In this crystallite the phase transition from HT to LT phase occurs, just when the LT phase forms small domains with parallel dipole arrays, giving broad reflection of the LT phase. The number of these small domains increases gradually and the whole crystallite becomes an aggregation of domains of different dipole arrays or forms the so-called multi-domain structure.

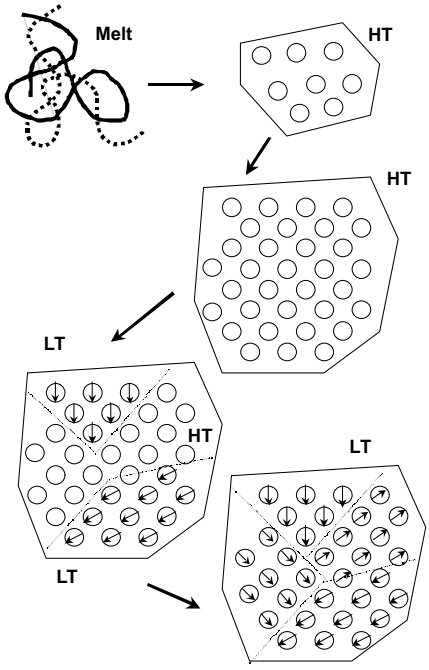

*ktashiro@chem.sci.osaka-u.ac.jp

14A/2000G043

X-ray diffraction studies of vanadium oxygen bronzes: $M_xV_2O_5$

Victor A. STRELTSOV*[1], Ruslan OZEROV[2] and Nobuo ISHIZAWA[3]
[1]Crystallography Centre, University of Western Australia, Nedlands, 6907, Australia.
[2]Mendeleev University of Chemical Technology of Russia, 125047 Moscow, Russia.
[3]Materials and Structures Laboratory, Tokyo Institute of Technology 4259 Nagatsuta, Japan.

Introduction

The triple metal oxides $nM_2O.mV_2O_4.pV_2O_5$ (M = Li, Na, K, Ag or Cu) with monoclinic structures exhibit unique physical (electrical, optical, mechanical etc) and chemical (high resistance to acids) properties and are often called "bronzes" due to their similarity to tungsten bronzes [1]. Their applications include electric batteries and selective electrodes in chemistry. The distorted VO_6 octahedra with common edges and corners form a rigid cage with tunnels spread along the monoclinic axis in the structure. The M metals are located in those tunnels. It is generally believed that unusual properties originate from special electronic states of the M and V atoms. These structures are quasi-one-dimensional conductors due to high anisotropy of the electric conductivity in the monoclinic direction. Such anisotropy can be explained by the existence of the V^{4+}–V^{4+} spin-singlet pairs (bipolarons) formed by strong electron-phonon coupling [2] which travel along the monoclinic axis. The conductivity in the other directions is due to diffusive electron hopping motion. The polaron condensation and ordering phenomena were observed by NMR and X-ray diffuse scattering, and some satellite reflections were detected in several alkali bronze β-phases [3] possibly due to the bipolaron ordering. The aim of this study is to re-examine the crystal structure and the electron density in several $M_xV_2O_5$ in attempt to improve our understanding of the chemical bonding in these compounds.

Experimental

Synchrotron X-ray diffraction data sets for β-$Na_xV_2O_5$ (x=0.28), $Ag_xV_2O_5$ (x=0.33) and β'-$Cu_xV_2O_5$ (x=0.65) were collected over complete spheres up to $(\sin\theta/\lambda)_{max}$=1.1 Å^{-1} at room temperatures with λ= 0.7Å radiation using the BL14A beam line four-circle diffractometer. In order to reduce absorption and extinction effects, a tiny, naturally faced specimen with dimensions less than 50 μm was used. Analytical absorption, Lorentz and polarization corrections and anomalous dispersion were applied. Symmetrically equivalent reflections were averaged. Independent structural parameters, including the scale factor, positional and thermal displacement parameters for all atoms were refined by conventional full-matrix least squares. Charge density multipole refinements were performed for β-$Na_{0.28}V_2O_5$ and and β'-$Cu_{0.65}V_2O_5$ structures so far.

Results and discussion

The Na isomorph is the most studied β-phase. The three different types of V atoms, the Na atom and the seven different O atoms occupy the 4i (m) crystallographic positions in the unit cell (sp.gr. C2/m). The Na atom positions are approximately half occupied. The eighth O atom is in 2a (2/m) position with fixed parameters. One of the conductivity models suggests the ordered alternation of the Na sites occupations along the monoclinic axis. This requires the doubling of the b cell parameter. However, no superstructure reflections related to this doubling has been detected for β-$Na_{0.28}V_2O_5$. The second model suggests the random alternation of the Na sites occupations and no changes of the unit cell parameters are required. This model places the Na atoms one under another along the y-axis.

The Cu atoms in β'-$Cu_{0.65}V_2O_5$ (sp. gr. C2/m), contrary to the Na compound, occupy three positions: one Cu1 is in 4(i) position with coordinates x=0.541, y=0 and z =0.344 and two Cu2 atoms in 8(j) position with coordinates x=0.529, y=0.038 and z =0,358 (shifted away from the mirror plane and symmetry related).

Static deformation charge density maps (Δρ) in the (010) plane (contours 0.2e/Å^3) for β-$Na_{0.28}V_2O_5$ and β'-$Cu_{0.65}V_2O_5$ in figure below were calculated after multipole refinement. The Δρ map for β-$Na_{0.28}V_2O_5$ is appeared to be highly anisotropic. The positive Δρ (more

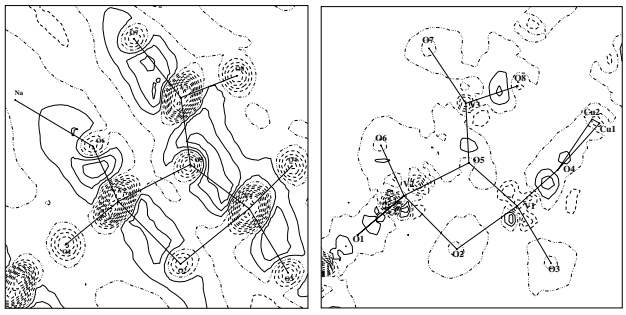

β-$Na_{0.28}V_2O_5$ β'-$Cu_{0.65}V_2O_5$

covalency) is predominant in the approximate (20 0 1) plane. This reflects the strong bonds between atoms in the plane, whereas there are no such 'covalent' bonds between these planes or sheets. The excess Δρ-density in the V-O bonds forms the extended regions of the positive density along the monoclinic b axis. The atomic charges were estimated from the multipole model, however there is no correlation between the atomic charges and the expected positions for the five- and the four-valence vanadium atoms.

References

[1] R.P. Ozerov. Kristallografia. 2, 226 (1957).
[2] B.K., Chakraverty et al., Phys. Rev. 17B, 3781 (1978).
[5] Y. Kanai et al., J. Phys. Soc. Japan. 51, 697 (1982).

*strel@crystal.uwa.edu.au

15A/2000G061

SAXS studies of the formation mechanisms of metal clusters in micelles of surfactants

Masafumi HARADA*[1], Kenji SAIJO[2], Mikihito TAKENAKA[2], and Takeji HASHIMOTO[2]
[1]Department of Textile and Apparel Science, Faculty of Human Life and Environment, Nara Women's University, Nara 630-8506, Japan
[2]Department of Polymer Chemistry, Graduate School of Engineering, Kyoto University, Kyoto 606-8501, Japan

Introduction

Hydrophobic field produced by the micelles of surfactants in aqueous solutions plays an important role for the control of size and dispersity of the metal nanoparticles when prepared [1]. Colloidal dispersions of platinum and gold particles can be prepared by photo-reduction of $H_2PtCl_6 \cdot 6H_2O$ and $HAuCl_4 \cdot 4H_2O$, respectively, in the presence of stabilizer such as surfactants [2]. In the photo-reduction process, we attempt to characterize the structures of primary metal particles and secondary metal particles (aggregated particles) [3] in solution of various surfactants as well as the change of average particle size in reduction by means of small angle X-ray scattering (SAXS).

Experimental

Platinum and gold colloidal dispersions (0.66mM) were prepared from $H_2PtCl_6 \cdot 6H_2O$ and $HAuCl_4 \cdot 4H_2O$ by irradiation of 500W super-high-pressure mercury lamp in 5 wt% aqueous solution, with benzoin as a photo-activator, of fluorinated surfactants (FTERGENT 110 and FTERGENT 250) kindly provided from NEOS Co. Ltd. Similarly, these Pt and Au colloids in emulsions were also prepared by the photo-reduction in 500 mM AOT(bis(2-ethylhexyl) sodium sulfosuccinate) solutions of the mixture of benzene and water. These reduced samples prepared in quartz cell at the designated duration of reduction were then poured into cells (optical length: 1mm) sealed with Kapton film for SAXS measurements.

SAXS measurements were performed at BL-15A station. X-ray beam was monochromatized to 0.150 nm in wavelength and the scattering data was collected by the position sensitive proportional counter (PSPC). The accumulating time for an intensity measurements of each sample was 600 sec.

Results and Discussion

Figure 1 shows SAXS profiles (log I(q) vs. q) of $HAuCl_4 \cdot 4H_2O$ (before reduction) and Au colloids (after reduction) prepared in FT 110 aqueous solutions. Here q is the magnitude of the scattering vector, defined as $q = (4\pi/\lambda)\sin(\theta/2)$ where θ is the scattering angle and is the wavelength of X-ray. The intensity tends to increase with the reduction time increasing. At a small q range ($q < 0.5$ nm^{-1}), the scattered intensity of solution after reduction (reduction time longer than 1 hour) is much stronger than that of $HAuCl_4 \cdot 4H_2O$ solution before reduction (reduction time = 0).

On the other hand, the maximum intensity appears around $q = 0.8$ nm^{-1} (before reduction) and $q = 0.7$ nm^{-1} (after reduction), respectively, although the reference solution has the maximum intensity at $q = 0.9$ nm^{-1}. This indicates that the addition of Au ions to micelles of FT 110 reference solution leads to change the size of micelles created in solution and Au particles created after photo-irradiation make the size of micelles much larger. Thus, the Au ions as well as Au particles are strongly stabilized in micelles of fluorinated surfactant without precipitates. The similar trends are also observed in the case of Au colloids in AOT/ H_2O/Benzene emulsion system.

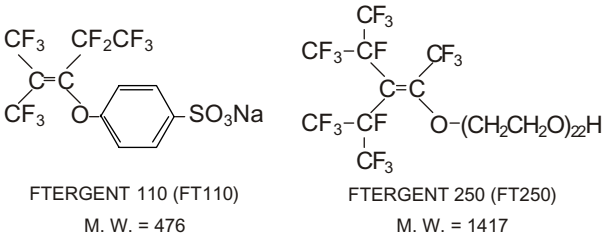

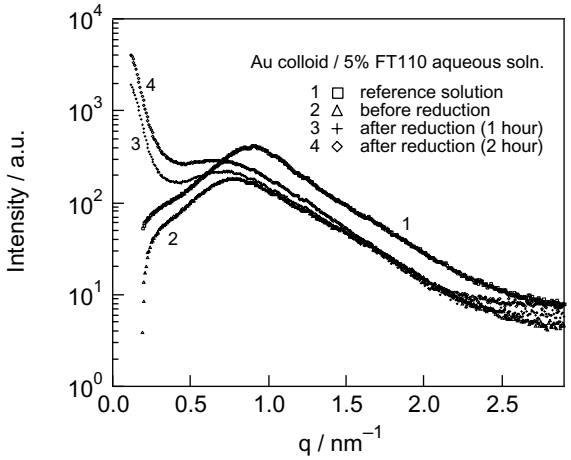

Fig. 1 SAXS profiles obtained from Au solutions dissolving FT 110 before and after photo-reduction.

References

[1] N. Toshima et al., Chem. Lett., 1245 (1985).
[2] A. Henglein, J. Phys. Chem., **97**, 5457 (1993).
[3] T. Hashimoto et al., J. Chem. Phys. **109**, 5627 (1998).
* harada@cc.nara-wu.ac.jp

15A/2000G066

Ultrasonic effect for the acceleration of polymorphic crystallization on fats

Satoru UENO*[1], Morio TAKEUCHI[2], Jun-ichi SAKATA[1], Yoshinobu NOZUE[2], Yoshiyuki AMEMIYA[2], Kiyotaka SATO[1]
[1]Hiroshima Univ., Higashi-Hiroshima, 739-8528, Japan
[2]The Univ. of Tokyo, Hongo, Bunkyo-ku, Tokyo 113-8656, Japan

Introduction

A considerable interest has been shown recently in the use of high power ultrasound for encouraging nucleation and for modifying crystal growth [1]. It has been demonstrated that a high power ultrasound (sonication) can increase significantly the rate of nucleation in a crystallisation medium (sono-crystallisation) [2]. Quite recently, sono-crystallisation has been examined in confectionery fats, indicating the possibility that tempering is achieved by sono-crystallisation [3]. However, the events accompanying sono-crystallisation processes in fats still remain mysterious with the need to understand them in order to achieve the control.

This paper presents experimental studies on the effects of high power ultrasound on the crystallisation behaviour of the typical triacylglycerols, tripalmitin (PPP) and trilaurin (LLL), examined *in-situ* by time-resolved SAXS and WAXS techniques. An attempt is made to suggest a mechanism by which a sonication leads to the formation of a particular polymorph in these materials.

Experimental Section

Tripalmitin (PPP) and trilaurin (LLL) were used as the samples and were purchased from Sigma Chem.Co (St. Louis, MO). Both of them had a purity of more than 99% and were used without further purification.

Experiments were carried out using *in-situ* synchrotron radiation time resolved small angle X-ray scattering and wide angle X-ray scattering (SAXS/WAXS) simultaneous measurement combined with a sono-crystallisation system assembled from commercial components; a computer-controlled ultrasound generator (model DG-100-20; Telsonic Co., Bronschhoften, Switzerland) at 20 kHz and 100W. The duration of sonication was 2 s. The sample of 5 ml was put in a handmade special glass cell jacketed by circulating water and connected to two thermostats: one for melting (hot) and the other for crystallisation (cool). The window of the cell was made of Capton film of 25 μm thickness. A sample thickness exposed to a synchrotron X-radiation was 3 mm. In both cases, without and with sonication, the sample was first melted and heated up to 80 ℃ for (PPP) and 60°C for (LLL), then the sample was cooled down with jacketed water to a desired level. Experiments presented in this work were performed at BL-15A. Camera length of the SAXS was 1.1 m. For the WAXS, this length was 0.27 m for both samples. The system was operating at a wavelength of 0.15 nm.

Results and Discussion

Without ultrasound application, both polymorhic forms β' and β crystallised in the melt of each substance.

With ultrasound treatment of the melt the following effects were observed: (i) a marked decrease of induction times for crystallisation of both (PPP) and (LLL), (ii) an increased nucleation rate, and (iii) a crystallisation of only β forms for both (PPP) and (LLL) under conditions of initial crystallisation temperature of 50 ℃ and 30 ℃, respectively, and applied ultrasound of 2 s. The last finding demonstrates that ultrasound irradiation can be used as an efficient tool for controlling polymorphic crystallisation of fats. In addition to this, a crystallisation of (LLL) under lower initial crystallisation temperature of 25 ℃ and with the same ultra-sonication time of 2 s, revealed the presence of both β' and β polymorphs. This suggests that crystallisation of only β form depends on the initial temperature of crystallisation as well as on the duration of ultrasound treatment of the melt.

When a sonication is applied to the melt, three major simultaneous processes are taking place: (1) the local changes of compression, (2) absorption of energy from the applied sounds waves, and (3) cavitation. The effect (1) is manifested by a corresponding increase in local pressure. This will result in a local increase of melting points. As a consequence, the corresponding supercoolings with respect to the selected initial crystallisation temperature will increase, too. The higher supercoolings will lead to: (a) a higher probability for nucleation, (shorter induction time), and (b) an increase of nucleation rate. As for explanation of the nucleation of only form, we need to consider the additional effect (2), which is a consequence of interaction of ultrasound wave with a melt. The effect (2) causes the increase of temperature of samples. This results in a larger number of melting of β' clusters than that of β cluster.

As for the effect (3), cavitation, it is a future study for involving it to explain the results in this work.

References

[1] T.J. Mason et al., Ultrasonics Sonochem. **3**, S253 (1996).
[2] K. Ohsaka et al., Appl. Phys. Lett. **73**, 129 (1998).
[3] J.F. Baxter et al., EU-Patent Appl.: 95306833.5(1995).

* sueno@hiroshima-u.ac.jp

7C, 10B, 12C/2000G076

EXAFS studies of the formation mechanisms of metal clusters in micelles of surfactants

Masafumi HARADA*[1], Takashi YAMAMOTO[2], and Tsunehiro TANAKA[2]
[1]Department of Textile and Apparel Science, Faculty of Human Life and Environment, Nara Women's University, Nara 630-8506, Japan
[2]Department of Molecular Engineering, Graduate School of Engineering, Kyoto University, Kyoto 606-8501, Japan

Introduction

Colloidal dispersions of nanometer-sized platinum and gold clusters are of wide interest because of their specific functions which are different from those of either bulk metal solids or metal atoms. Surfactants are known to have the function to solubilize hydrophobic substances in aqueous solutions. The method to prepare colloidal dispersions of metal clusters in the hydrophobic field produced by the micelles of surfactants is important for the purpose of control of size and dispersity of the obtained metal clusters [1]. Colloidal dispersions of platinum and gold clusters could be prepared by photo-reduction of $H_2PtCl_6 \cdot 6H_2O$ and $HAuCl_4 \cdot 4H_2O$, respectively, in the presence of stabilizer such as polymers [2]. The aim of this study is the determination of the particle formation mechanisms in micelles of various surfactants as well as the change of average particle size in solution at the photo-reduction process.

Experimental

Platinum and gold colloids (0.66mM) were prepared from $H_2PtCl_6 \cdot 6H_2O$ and $HAuCl_4 \cdot 4H_2O$ by irradiation of 500W super-high-pressure mercury lamp in 100mM aqueous solution of surfactants (SDS: Sodium Dodecyl Sulfate, DTAC: Dodecyltrimethylammonium Chloride, PEG: Polyethylene Glycol Lauryl Ether) with benzoin, respectively. The reduced samples prepared in quartz cell at the designated duration of reduction were then poured into cells for EXAFS measurements.

Pt-L_3 and Au-L_3 edge EXAFS spectra were collected at the BL-7C and/or BL-12C. The EXAFS measurements of the metal colloids were carried out at room temperature in a fluorescence mode using a Lytle type detector to estimate their formation mechanism of colloids.

Results and discussion

Figure 1 shows the Pt-L_3 edge EXAFS Fourier transforms for 0.66mM Pt colloids stabilized by PEG after 5 hour's photo-reduction, comparing with that for Pt foil. The main peak is assigned to a Pt-Pt bond, which was determined to be 0.276 nm in distance by curve-fitting analysis. In the case of the Pt colloids stabilized by SDS and DTAC, Pt-Pt bond is mainly observed as shown in Table 1. Their coordination numbers (C.N.) and bond distances (R) obtained from the curve-fitting are listed.

On the other hand, the curve-fitting analysis of photo-reduced Au colloids stabilized by SDS, PEG, and DTAC was conducted with the model parameters extracted from the reference compounds of Au foil and $HAuCl_4 \cdot 4H_2O$ solid powder. As for any surfactants, the Au-Au bond distance values for Au colloids coincided with the value of 0.287 nm for Au foil, but the coordination numbers were in the range of 6.0 – 8.1, that were apparently smaller than that (C.N. = 12) of Au foil. Therefore, the Au colloids are strongly stabilized in micelles of surfactants in solution and they become very stable.

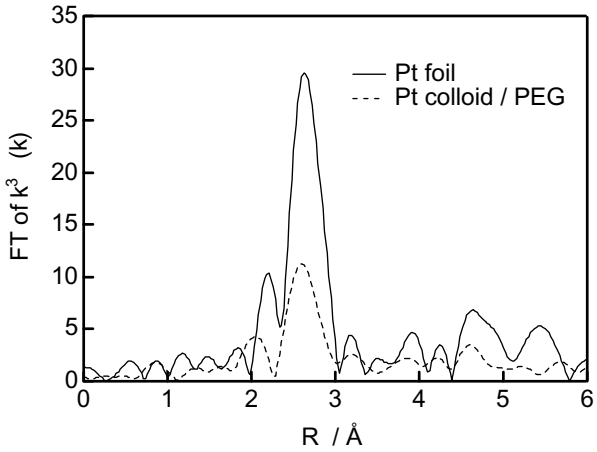

Fig.1 Fourier transforms of Pt-L_3 edge for Pt foil and Pt colloids.

Table 1. Curve-fitting results for Pt and Au colloids

Sample	Bond	R / Å	C.N.	σ^2 / Å ^{2}	R factor
Pt / SDS100	Pt - Pt	2.76	5.5	1.23×10^{-3}	0.263
Pt / PEG100	Pt - Pt	2.76	6.4	1.28×10^{-3}	0.305
Pt / DTAC100	Pt - Pt	2.76	2.7	3.59×10^{-3}	0.314
	Pt - Cl	2.33	1.6	1.10×10^{-4}	
Au / SDS100	Au - Au	2.85	7.7	-1.68×10^{-3}	0.297
Au / PEG100	Au - Au	2.85	6.0	-2.83×10^{-3}	0.515
Au / DTAC100	Au - Au	2.87	8.1	-1.67×10^{-3}	0.216

References

[1] H. Hirai and N. Toshima, Colloidal Metal, Polymeric Materials Encyclopedia, J. C. Salamone, Ed. CRC Press, Boca Raton, FL, Vol. 2/c, (1996) pp 1310-1316.
[2] M. Harada et al., J. Phys. Chem. **98**, 2653 (1994).
*harada@cc.nara-wu.ac.jp

10B/2000G081

EXAFS study on the spin crossover complex film, [Fe(II)(R-trz)$_3$]-Nafion

Akio NAKAMATO[1], Yuuki ONO[1], Daiju Matsumura[2], Toshihiko Yokoyama[3], Norimichi KOJIMA*[1]

[1]Graduate School of Arts and Sciences, The University of Tokyo, Komaba 3-8-1, Meguro-ku, Tokyo, 153-8902, Japan

[2]Department of Chemistry, Graduate School of Science, The University of Tokyo, Hongo, Bunkyo-ku, Tokyo, 113-0033, Japan

[3]Institute for Molecular Science, Myodaiji, Okazaki, 444-8585, Japan

Introduction

Spin crossover complexes [Fe(II)(R-trz)$_3$]X$_2$ nH$_2$O (trz = triazole, R = H, NH$_2$, etc.; X = ClO$_4$, C$_n$H$_{2n+1}$SO$_3$, etc.) are attracting much attention from the viewpoint of molecular devices due to the large thermal hysteresis of spin transition around room temperature [1,2]. In order to realize molecular devices, the transparent film or single crystal is indispensable. However, the single crystal has not yet been obtained. We have synthesized the spin crossover complex film of [Fe(II)(H-trz)$_3$] using ion exchange resin (Nafion) as counter anion, and measured the magnetic susceptibility and Fe *K*-edge EXAFS spectra for [Fe(II)(H-trz)$_3$]-Nafion.

Experimental

Nafion is composed of a polytetrafluoroethylene backbone with perfluorinated ether side chains terminated by sulfonic acid group as shown below,

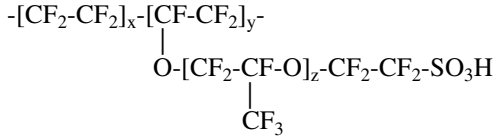

[Fe(II)(R-trz)$_3$]-Nafion was prepared in the following way. The acid form of Nafion was immersed in an aqueous solution of FeSO$_4$. After being immersed in the solution for 2 hours, the membrane was rinsed in methanol, and then it was immersed in methanol solution of Htrz at 330 K for 1 hour.

The temperature dependent magnetic susceptibility was measured by a Quantum Design MPMSXL SQUID susceptometer. Fe *K*-edge EXAFS spectra were taken in the conventional transmission mode at BL-10B in Photon Factory (operation energy of 2.5 GeV and stored current of 400-200mA) in Institute of Materials Structure Science. A water-cooled Si(311) channel-cut crystal was employed as a monochromator.

Results and discussion

Fe *K*-edge EXAFS spectra of [Fe(R-trz)$_3$]-Nafion (R = H, NH$_2$) are shown in Fig. 1. The peak around 7 Å corresponds to the Fe-Fe-Fe multiple scattering. Therefore, it is proved from this fact that the linear chain of [Fe(R-trz)$_3$] exists in Nafion. The magnetic susceptibility as a function temperature implies the gradual low spin (LS) – high spin (HS) transition around 260 K, where the thermal hysteresis vanishes.

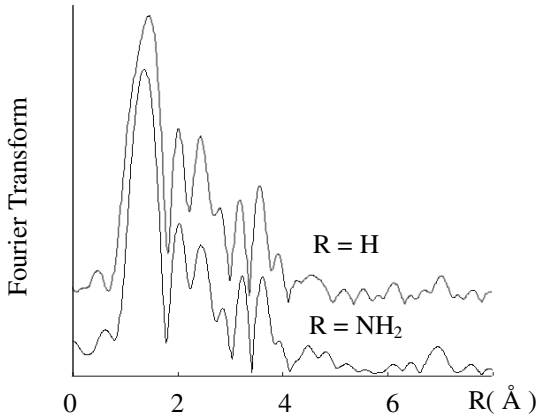

Fig. 1. Fourier Transform of EXAFS spectra of [Fe(R-trz)$_3$]-Nafion at 85 K

From the temperature dependence of χT for [Fe(H-trz)$_3$]-Nafion, it was found that even at 10 K, the HS still remains by ~40 %. The residual HS fraction would be attributed to the terminal Fe(II) site in the oligomer of [Fe(II)(H-trz)$_3$]$_n$ on Nafion film. In connection with this, the following should be mentioned. Fe(II) trimer complex, [Fe$_3$(Et-trz)$_6$(H$_2$O)$_6$](CF$_3$SO$_3$)$_6$ (Et-trz = 4-ethyl-1,2,4-triazole), the central Fe(II) site undergoes the LS-HS transition at about 200K, while the spin state of the terminal Fe(II) sites is the HS state between 2K and 300K [3]. It is considered that the mean size of [Fe(H-trz)$_3$]$_n$ oligomer is about n = 5 ~ 6. The disappearance of hysteresis suggested that interchain interaction play an important role in the hysteresis effect.

References

[1] J. Kröber, E. Codjovi, O. Kahn, F. Groliere, C. Jay, J. Am. Chem. Soc. **115**, 9810 (1993).

[2] Y. Murakami, T. Komatsu, N. Kojima, Synthetic Metals **103**, 2157 (1999).

[3] G. Vos, R. A. G. Graaff, J. G. Haasnoot, A. M. Kraan, P. Vaal, J. Reedijk, Inorg. Chem. **23**, 2905 (1984).

* cnori@mail.ecc.u-tokyo.ac.jp

9A,27B/2000G086

EXAFS study of reduced $Ce_{1-x}Ln_xO_{2.00-y}$ (Ln = Y, Sm, Gd and Yb) (III)

Tsuneo Matsui*[1], Yuji Arita[2], Satoshi Yamazaki[1], Hiroyuki Konishi[3], Katsumi Kobayashi[4]
[1]Department of Quantum Engineering, Graduate School of Engineering, Nagoya University, Furo-cho, Chikusa-ku, Nagoya 464-8603, Japan
[2]Research Center for Nuclear Materials Recycle, Nagoya University, Furo-cho, Chikusa-ku, Nagoya 464-8603, Japan
[3]Kansai Research Establishment Synchrotron Radiation Research Center, Japan Atomic Energy Research Institute, 1-1-1, Koto, Sanmyo-cho, Sayo-gun, Hyogo 679-5148, Japan
[4]Photon Factory, Institute of Materials Structure Science, High Energy Accelerator Research Organization, 1-1, Oho, Tsukuba, Ibaraki 305-0801, Japan

Introduction

Anomalous increases in the heat capacity curves of some reduced ceria doped with Gd were observed at temperatures around 860-960 K, depending on both the Gd concentration and the oxygen deficiency[1+ oe r i d4 n

10C/2000G100

Polymorphism of syndiotactic polystyrene from the molten state observed by the simultaneous DSC-XRD

Hirohisa YOSHIDA*, Takafumi WATANABE, Tomoko YOSHII, Gongzheng ZHANG
[1]Graduate School of Engineering, Tokyo Metropolitan University, Hachioji, Tokyo 192-0397, Japan

Introduction

Syndiotactic polystyrene (SPS) shows four polymorphisms, two crystalline forms containing molecular chains in TTTT conformation and two in TTGG conformation designated α, β, γ and δ, respectively. The former conformation is formed in the bulk polymerization. In this study, the crystallization process of SPS from the molten state was investigated by the simultaneous DSC-XRD measurement.

Experimental

SPS (Mn=17 x 10^4, Mw/Mn=2.3) used in this study was kindly supplied from Asahi Chemical Industry Co. Ltd. The amorphous press film was obtained by quenching from the molten state at 573 K. The amorphous SPS showed glass transition at 373 K, cold-crystallization at 419 K and melting at 548 K observed at 5 K/min. The DSC-XRD instrument was setting on SAXS optics at BL-10C, PF, KEK. The wavelength of X-ray was 0.1488 nm monochromated by double Si crystals. The size of X-ray was 0.6 x 0.6 mm.

After melting at 573 K for 5 mins, SPS was cooled to 473 K at various scanning rate from 1 K/min to 10 K/min. SPS was heated again to 573 K at 5 K/min immediately after arrived at 473 K. The time resolution of a XRD profile was 30 sec.

Results and discussion

Upon cooling a monotropic exothermic peak was observed on DSC curve in the temperature range from 515 K to 530 K depending on the cooling rate. However, two kinds of XRD diffraction peak at 0.7 nm^{-1} and 0.76 nm^{-1} were observed at the same temperature region. These XRD peaks were assigned to β(020) and α(110), respectively. On the other hand, two endothermic peaks sue to the melting were observed at 535 and 546 K on heating. The rate of both endothermic peak areas was influenced by the cooling rate. With increasing the cooling rate, the area of endothermic peak at 535 K and the XRD peak intensity of β(020) increased.

The DSC-XRD results for SPS cooled at 10 K/min and 2.5 K/min are shown in Fig.1 and 2, respectively. The temperature changes of XRD peak intensity of β(020) and α(110) are also plotted in figures. On Crystallization, the XRD peak of β(020) appears slightly faster than the XRD peak of a(110). However, both crystal forms grow at the same time on cooling. On heating, the XRD peak of β(020) started to decrease at the endothermic peak of the lower temperature and then the XRD peak at a(110) started to decrease at the higher endothermic peak. This result suggests that the endothermic peak at 535 K is due to the melting of b-form. However, the XRD peak of b(020) remains until the higher endothermic peak temperature. The crystal form obtained was determined not only by thermodynamic stability but also by kinetic process of crystallization.

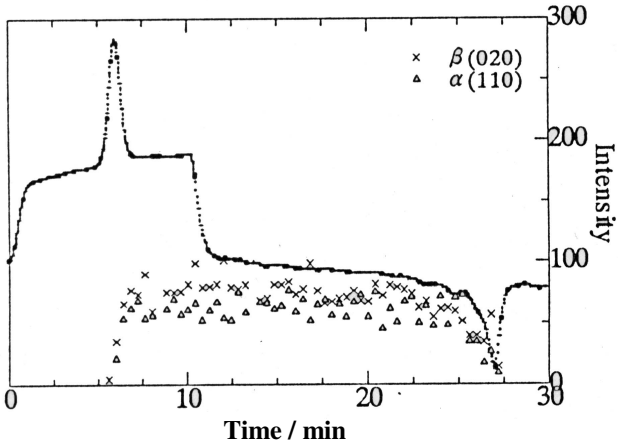

Fig.1 The DSC-XRD results of SPS obtained by cooling at 10 K/min and heating at 5 K/min

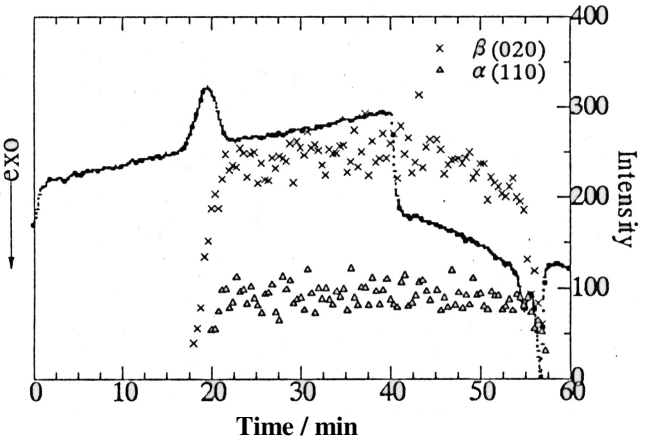

Fig.2 The DSC-XRD results of SPS obtained by cooling at 2.5 K/min and heating at 5 K/min

* yoshida-hirohisa@c.metro-u.ac.jp

27B/2000G105

Local structure of solid and molten strontium dichloride

Yoshihiro OKAMOTO[1*], Tsuyoshi YAITA[1], Haruhiko MOTOHASHI[2], Katsumi KOBAYASHI[3], Noriko USAMI[3]

[1]Japan Atomic Energy Research Institute, Tokai-mura, Naka-gun, Ibaraki 319-1195, Japan
[2]SPring-8 Service Corporation, Kouto, Mikazuki-cho, Hyogo, 678-1205, Japan
[3]KEK-PF, Tsukuba, Ibaraki 305-0801, Japan

Introduction

We have studied the local structure of molten salt systems by high temperature XAFS technique[1]. In the present study, we report the local structure of solid and molten $SrCl_2$.

Experimental

The XAFS measurements of solid and molten $SrCl_2$ (Sr K-dege) were performed in transmission method at the BL27B station in the KEK-PF. The samples were sealed off in the quartz cell under reduced pressure($<10^{-5}$Torr). Details of the XAFS measurement of molten salts are described in ref.[2]. The XAFS spectra were obtained at room temperature, 1073 and 1273K. The XAFS data was analyzed by using WinXAS code[3].

Results and discussions

The Fourier transform magnitude |FT| functions for solid and molten $SrCl_2$ are shown in Fig.1. Structural parameters of the nearest Sr^{2+}-Cl^- correlation determined from the curve fitting are listed in Table 1. The averaged distance does not change by melting. On the other hand, the coordination number decreases from 8 to 6.6. It corresponds to the volume change $\Delta V_m/V=0.13$ at melting. At 1073K, it can be considered that the sample is in a superionic state because of increasing in Debye-Waller factor and unchanged coordination number.

The molecular dynamics calculation of solid and molten $SrCl_2$ was performed by using pair potentials proposed by Gillan and Dixon[4]. The XAFS function $k^3\chi(k)$ was synthesized by using the GNXAS[5] from the MD results. The XAFS functions at 1073 and 1273K were successfully reproduced by the MD simulation as shown in Fig.2.

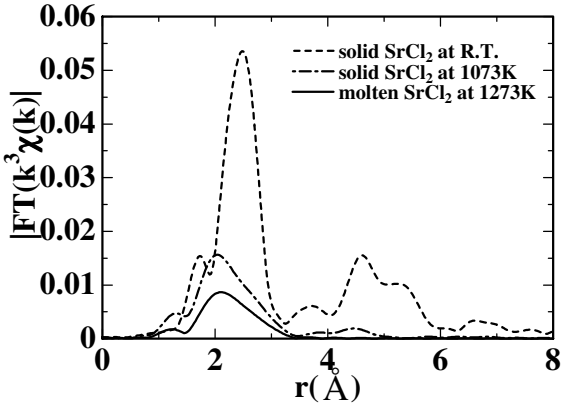

Fig.1 XAFS function $k^3\chi(k)$ and Fourier transform magnitude |FT| of $SrCl_2$

Table 1 Structural parameters (N: coordination number, r: interionic distance, σ^2: Debye-Waller factor, C3,C4: 3rd and 4th cumulants) of the nearest Sr^{2+}-Cl^- correlation in $SrCl_2$

	N	r(Å)	σ^2(Å^2)	C3(Å^3)	C4(Å^4)
R.T.	8.0(fix)	3.00	0.0159	---------	--------
1073K	8.1	3.07	0.0416	8.5×10^{-3}	7.1×10^{-4}
1273K	6.6	2.99	0.0574	6.8×10^{-3}	1.5×10^{-3}

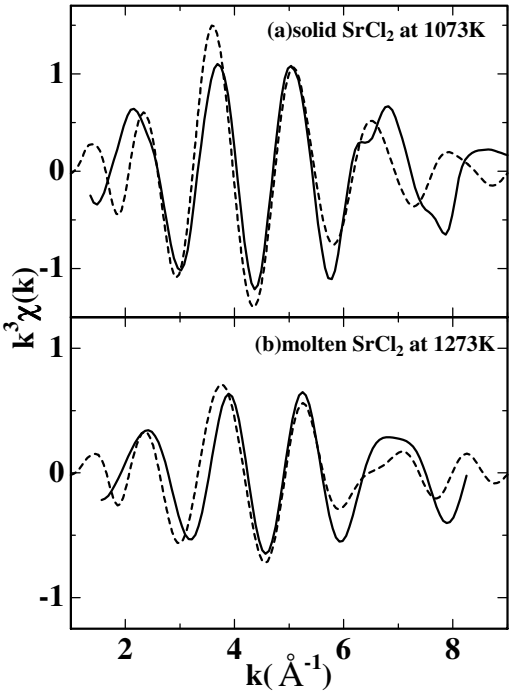

Fig.2 XAFS function $k^3\chi(k)$
solid : experimental, dashed : MD+GNXAS

References

[1]Y.Okamoto et al., J.Synchrotron Rad., **8**, 1191(2001).
[2]Y.Okamoto et al., Nucl. Instr. Meth. Phys. Res., A, **487**, 232(2002).
[3]T.Ressler, J.Phys., IV 7, c2-269(1997).
[4]M.J.Gillan and M.Dixon, J.Phys. C: Solid St. Phys., **13**, 1901(1980).
[5]A.Di Cicco, Physica B, **208&209**, 125(1995).
* okamoto@molten.tokai.jaeri.go.jp

4A, 15A/2000G159

Time resolved simultaneous SAXS/DSC study on oil crystallization in O/W monodispersed emulsion

Naohiko Kawasaki[1], Satoru Ueno[2], Mitsutoshi Nakajima[3], Atsuo Iida[4], Yoshiyuki Amemiya*[1]
[1]Department of Frontier Sciences, The University of Tokyo, Tokyo, 113-8656, Japan
[2]Faculty of Applied Biological Science, Hiroshima Univ, [3]National Food Research Institute, Tsukuba
[4]Photon factory, Institute of Materials Structure Science, Tsukuba

Introduction

Oil crystallization in oil-in-water (O/W) emulsions has been studied extensively in terms of the emulsion stability. However, past researches were carried out with emulsion samples having a wide distribution of particle size. So, the information from these researches was that averaged over various sizes of emulsions, and hence was ambiguous. Here, we have used monodispersed emulsions, which have a narrow distribution of particle size so that we could discuss the behavior of oil crystallization in O/W emulsions in relation to their sizes. Here, we will report on the behavior of oil crystallization in well-defined-sized emulsions observed by time resolved simultaneous SAXS /DSC (Difference Scanning Calorimetry) measurement.

Experimental

O/W emulsion samples were made by micro-channel emulsification method [1] at National Food Research Institute. Samples consisted of n-hexadecane (oil phase), distilled water (continuous phase), and Tween20 (emulsifier). Emulsion sizes were 40 and 10 μm in diameter. We also made samples, in which olephilic surfactant, DAS-750, was added to the oil phase as an additive, because it was reported that adding DAS-750 accelerates crystallization of n-hexadecane [2]. The simultaneous SAXS/DSC measurements were carried out at BL-15A, at a cooling rate of 2 degrees/min from room temperature. X-ray beam size was about $1\times1mm^2$.

Results and discussion

Fig.1 shows DSC profiles and temperature dependence of integrated intensity of the SAXS peak from n-hexadecane lamellar structure (≅20A), in the case of 40 m emulsions. In Fig.1, the integrated intensity increases with two steps, and DSC profiles have corresponding two peaks. So, it is obvious that crystallization of n-hexadecane in emulsion system includes two different behaviors. Crystallization at a higher temperature takes place at 14℃, which is exactly equal to the crystallization temperature of n-hexadecane in bulk system. So, it is considered that crystallization at a higher temperature is analogous to that in bulk system. On the other hand, crystallization at a lower temperature is specific to emulsion system. And adding DAS-750 raises the temperature of this crystallization.

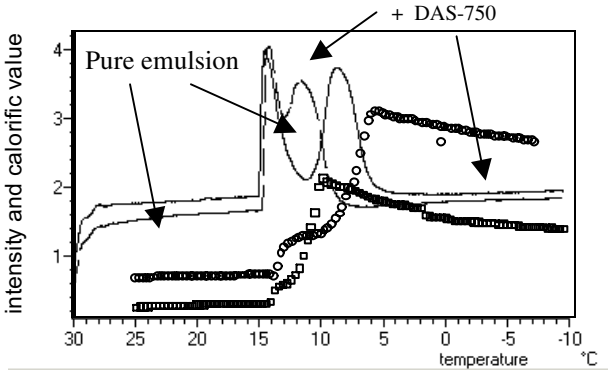

Fig.1 DSC profiles and temperature dependence of the integrated intensity of SAXS n-hexadecane peak (40μm emulsion).

In previous experiments [2] carried out with much smaller-sized emulsions (0.9μm), only crystallization specific to emulsion system was observed. However, we have found that bulk-like crystallization also takes place in larger-sized (40 and 10μm) emulsions. In the experiment with 10μm emulsions, integrated intensity of the peak hardly increase at 13 °C, at which lower-temperature crystallization takes place (not shown). But it isn't reasonable to interpret that the rate of the bulk-like crystallization depends on emulsion size. So, we would interpret that the integrated intensity of n-hexadecane peak in Fig.1 reflects the product of the number and the volume of emulsions in which n-hexadecane is crystallized, rather than genuine crystallization rate. In some emulsions, bulk-like crystallization takes place, whereas in other emulsions, crystallization specific to emulsion system does. Because crystallization takes place within the volume of individual emulsions, when macroscopically observed, it seems that crystallization rate is lower in the case of smaller-sized (10μm) emulsions.

SAXS profiles showed another peak at a smaller angle (≅22A) when DAS-750 was added (not shown). This peak was observed also in the previous report [2], but in this experiment, it disappeared on the way of cooling process. It seems this behavior of the smaller angle peak is also specific to large-sized monodispersed emulsion samples.

References

[1] T.Kawakatsu et al., J.Chem.Eng.Jpn. **32**, 241 (1999).
[2] T.Aoyama et al., J. Oleo. Sci. **49**, 809 (1999).
* amemiya@k.u-tokyo.ac.jp

AR-NE1/2000G169

Investigation of Ni magnetic moment in Ni_2Gd Laves phase through MCP

Kazuo YANO*[1], Yoshikazu TANAKA[2], Isao MATSUMOTO[3],
Hiromichi ADACHI[3], Izuru UMEHARA[4], and Hiroshi KAWATA[3]
[1]Nihon Univ., Narashinodai, Funabashi, Chiba 274-8501, Japan
[2]The Institute of Physical and Chemical Research, Sayou-gun, Hyougo 679-5143, Japan
[3]KEK-PF, Tsukuba, Ibaraki 305-0801, Japan
[4]Yokohama National Univ., Tokiwadai, Yokohama, Kanagawa 240-8501, Japan

Introduction

Vast amounts of papers have been published in the investigation of magnetic properties of transition metal-rare earth (TM-RE) alloys in both crystalline and non-crystalline ones. Through every side of investigation, many interesting results were discovered and some important pictures have been established. One of these pictures is the vanishment of magnetic moment of the Ni when the RE content increases and reaches to the Laves phase[1]. However there have been no decisive evidences for this phenomenon. If the Ni possesses a magnetic moment of about 0.2 (μ_B) which corresponds to the value of Ni magnetic moment of Ni_3Gd, the Ni_2Gd behaves like a ferromagnetism and shows such as Curie Weiss law since the Gd magnetic moment is predominantly greater than that of the Ni. The assumption that the Ni retains a magnetic moment is consistent with the ever-known experimental facts. In this report, we examine whether the Ni does retain a magnetic moment or not in the Ni_2Gd Laves phase through the magnetic Compton Profile (MCP) [2].

Experimental

The polycrystalline Ni_2Gd Laves phase was prepared from Gd metal of 99.9% purity and Ni metal of 99.999% purity by arch-melting under an Argon atmosphere. The ingots obtained were annealed for three days at 900 degrees and X-ray powder diffraction at room temperature showed only reflections of a cubic C15 $MgCu_2$ type crystal structure. The obtained ingots consisted of fairly large single crystalline grains, which shows the high quality of these polycrystalline samples.

The MCP of the Ni_2Gd was measured at the AR-NE1 beamline. Circularly polarized X-ray from an elliptical multi-pole wiggler was monochromized and focused by a single channel-cut bent Si crystal. The energy of incident X-ray employed was 135 keV. The magnetization direction of the sample was reversed applying magnetic field of 1T by a superconducting magnet and the sample was cooled at 30K during the measurement.

Results and Discussions

The experimental results of the MCP obtained are shown in Fig.1 together with the analytical ones. The open circles are the experimentally obtained MCP data and the experimental ones apparently seem to be the MCP of 4f electrons of Gd calculated by Biggs et al [3]. The fitting of the calculated MCP of 4f electrons to the experimental one was carried out in the region of $|P_Z| \geq 5$ (solid line) since the MCP of 3d electrons of Ni (dotted line) [3] can affect on the profile of the experimental result in $|P_Z| \leq 5$. From the figure, it can be seen that the calculated MCP of 4f electrons of Gd fails to reproduce the experimental result. In order to explain this discrepancy, the calculated MCP of 3d electrons of Ni was taken into consideration. Considering that the magnetic structure of Ni-Gd system is ferrimagnetism [4], we subtract the MCP of calculated 3d from that of 4f. The result is shown in the figure by the one dotted line and it can reproduce the experimental result fairly well in $|P_Z| \geq 2$. The gap in $|P_Z| \leq 2$ corresponds to the s, p electrons contribution. This result implies that the Ni does retain the magnetic moment even in the concentration of Ni_2Gd Laves phase.

References

[1] K.N.R. Taylor, Advan. Phys. **20**, 603 (1971).
[2] N.Sakai, Mat. Sci. Forum **105-110**, 431 (1992).
[3] F.Biggs, L.B.Mendelsohn and J.B.Mann, Atomic Data and Nuclear Data Tables **16**, 201 (1975).
[4] K.N.R. Taylor, Advan. Phys. **20**, 605 (1971).

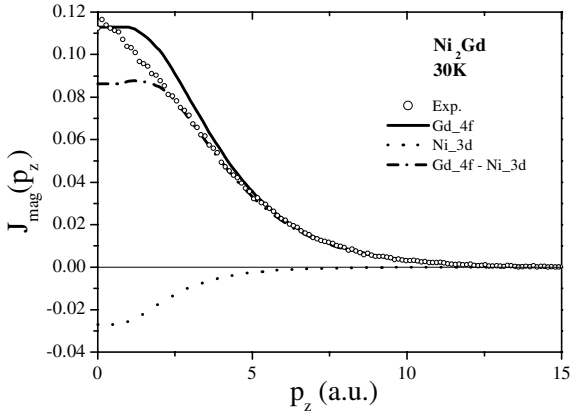

Fig.1 The MCP of Ni_2Gd Laves phase at 30K. Open circles are the experimental results and the solid, dotted and one dotted lines are the calculated 4f of Gd, 3d of Ni and subtracted MCP.

* kyano@phys.ge.cst.nihon-u.ac.jp

15A/2000G204

The influence of copper addition on the phase decomposition in Al-Zn-Mg alloys

Hiroki Adachi*, Junya Isogai*, Kozo Osamura*
*Department of Materials Science and Engineering, Kyoto University , Kyoto 606-8501,Japan

Introduction

Al-Zn-Mg alloys are precipitation-hardening type alloys of which hardness increases, when η' or T' metastable phase precipitates. And it is also well known that the amount of precipitation strengthening increase by addition of Cu. However, addition of Cu decreases the solubility limit of Zn and Mg. It is considered that decrease of the amount of addition of Zn and Mg reduces the volume fraction of precipitation, and also reduces the amount of precipitation strengthening. However, with the commercial Al-Zn-Mg-Cu alloy, since resistance to SCC remarkably falls by addition to the solubility limit of Zn and Mg, the amount of addition of Zn and Mg is stopped by about 70 percent of the solubility limit. However, since P/M alloy has more fine grain as compared to I/M alloy, it has high resistance to SCC. Therefore, if it adds Zn and Mg to the solubility limit, the alloy with high resistance to SCC is obtained. In this research, the change of metastable precipitate is investigated by addition of Cu into the alloy, which added Zn and Mg to the solubility limit.

Experimental

The alloys were prepared by powder metallurgy. The composition is shown in Table 1. The alloys were solution-treated at 763K for 72ks and then quenched into water. Then isothermal aging was carried out at 383K for various times (0~360ks). The SR small angle scattering measurements were carried out at BL-15A of Photon Factory in KEK. The detector is one-dimentional PSPC and the camera length is 1140mm. The hardness test was carried out for the investigating the mechanical property.

Table 1 Chemical composition of alloys (at%)

sample	Zn	Mg	Cu	Ag	Al
Cu-add	4.08	3.43	0.70	0.01	bal.
Cu-free	4.73	3.88	tr.	0.01	bal.

Result

The as-quenched hardness of Cu-free alloy and Cu-add alloy is 165 and 130, respectively. By aging, the hardness increases and show maximum at 108ks aging and then falls by overaging. Maximum hardness of Cu-free alloy and Cu-add alloy is 230 and 209, respectively. The maximum hardness of Cu-free alloy is ten percent higher than that of Cu-add alloy.

From the intensity profile of small angle scattering, the Guinier radius of the precipitate was calculated and the change by aging has been investigated. Pair correlation function with respect to spatial distribution of precipitates was calculated from the intensity profile. And the mean nearest neighbour distance among precipitates was estimated. Then the volume fraction was calculated by the Guinier radius and mean distance. The volume fraction doesn't depend on aging time and is fixed. The volume fraction of metastable phase for Cu-free alloy and Cu-add alloy are 3.8vol.% and 2.7vol.%, respectively. The volume fraction of Cu-free alloy is 40% larger than that of Cu-add alloy.

Discussion and conclusion

The increase of volume fraction by no addition of Cu is considered to be the cause of an increase of the highest hardness. However, the total solute atom, Zn, Mg and Cu, in Cu-free alloy and Cu-add alloy are 8.61at% and 8.21at%, respectively. The amount of solute increased 1.05 times. On the other hand, the volume fraction of precipitate increased 1.4 times. The quantity of solute change is not comparable to the quantity of volume fraction change. Therefore, it is considered that the reason that the volume fraction increases has a cause also besides the increase of solute atom.

The difference of electron density between matrix and precipitate can be calculated by integration intensity and volume fraction. Since the structure and composition determine the electron density, change of structure and composition can be guessed by change of the difference of electron density. The calculated difference of electron density for Cu-free alloy and Cu-add alloy is 43.0 and 56.7 a.u., respectively. This large change of difference of electron density means that the different metastable phase precipitates in these alloys. In Cu-free alloy and Cu-add alloy, it is considered that T' phase and η' phase have precipitated, respectively. Thus, since the kind of metastable phase changed with existence of Cu, the volume fraction is considered to have changed a lot in spite of a few change of quantity of solute atom.

* adachi@kumax.mtl.kyoto-u.ac.jp

4B/2000G215

Analysis of crystal structure for bismuth layer-structured oxides

Yuji NOGUCHI[*1], Masaru MIYAYAMA[2], Tetsuichi KUDO[2]
[1] Department of Applied Chemistry, School of Engineering, The University of Tokyo, 7-3-1 Hongo, Bunkyo-ku, Tokyo 113-8656, Japan
[2] Institute of Industrial Science, The University of Tokyo, 7-22-1 Roppongi, Minato-ku, Tokyo 106-8558, Japan

Introduction

Ferroelectric $SrBi_2Ta_2O_9$ (SBT), one of the promising candidate materials for nonvolatile random-access memories, has a layered structure. Thin films with compositions deviating from the stoichiometry of SBT have been extensively studied to improve ferroelectric properties. Noguchi *et al.*[1] reported that the remanent polarization (P_r) of the films with Sr-deficient and Bi-excess composition, $Sr_{0.8}Bi_{2.2}Ta_2O_9$, is larger than that of stoichiometric SBT. In spite of extensive efforts to improve the ferroelectric properties of thin films, the fundamental nature and the crystal structure of Sr-deficient and Bi-excess SBT have not yet been elucidated. This report describes the results of the structure refinement for stoichiometric SBT and $Sr_{0.73}Bi_{2.18}Ta_2O_9$ through the Rietveld analysis of synchrotron-radiation diffraction.

Experimental

Ceramic samples with nominal compositions of $SrBi_2Ta_2O_9$ (stoichiometric SBT), $SrBi_{2.04}Ta_2O_9$ (Bi-ex. SBT), $Sr_{0.73}Bi_{2.27}Ta_2O_9$ and $Sr_{0.73}Bi_{2.18}Ta_2O_9$ were prepared by the conventional solid-state reaction from ground powders of $SrCO_3$, Bi_2O_3, and Ta_2O_5 of 99.99% purity. The final sintering was performed at 1200 °C for 4 h. The samples obtained had a density of over 98 % of the theoretical density. For diffraction measurements, the calcined powder was fired at 1100 °C for 4 h to prevent grain growth and preferred orientation.

Synchrotron-radiation diffraction patterns were obtained using a powder diffractometer with a multiple-arm system at BL-4B2 of the Photon Factory in KEK[16]. The patterns obtained were analyzed by the Rietveld method (the RIETAN program) using the $A2_1am$ orthorhombic symmetry. For the values of anomalous scattering factors, f' and f'', a table calculated by Sasaki was used.

Results and Discussion

Figure 1 shows the result of the Rietveld analysis of the powder diffraction pattern. In the analysis, excess Bi was assumed to be substituted with cation vacancies at the perovskite *A*-site. The calculated pattern fits the observed data fairly well, confirming a single phase with SBT structure. The composition at the *A*-site determined by the Rietveld analysis was $(Sr_{0.73(3)}Bi_{0.18(3)}\square_{0.09})$, where $\square$ indicates cation vacancies. This analysis reveals that the charge neutrality in the crystal of $Sr_{0.73}Bi_{2.18}Ta_2O_9$ is satisfied through the substitution of Bi with cation vacancies at the *A*-site. Thus, these Rietveld results become direct evidence that Bi ions are substituted as *trivalent ions* with cation vacancies at the *A*-site [2].

In the SBT structure with the $A2_1am$ orthorhombic symmetry, the ***a*** axis is the polar axis, and constituent ions are displaced along the ***a*** axis. The spontaneous polarization (P_s) can be calculated by:

$$P_s = \Delta_i (m_i \times \Delta x_i \times Q_i e) / V, \quad (1)$$

where m_i is the site multiplicity, Δx_i is the atomic displacement along the *a* axis from the corresponding position in the parent tetragonal ($I4/mmm$) structure, $Q_i e$ is the ionic charge for the *i*th constituent ion, and V is the volume of the unit cell. Using the formal charge (+2 for Sr, +3 for Bi, +5 for Ta, –2 for O) in the calculation, P_s of stoichiometric SBT was estimated to be 16 μC/cm^2, which agrees well with the value determined from the data on the basis of the single-crystal structure analysis performed by Rae *et al.*.[5] For *A*-def. SBT, P_s was found from calculation to be 20 μC/cm^2 using the result of our Rietveld analysis, and this increase in P_s is consistent with our polarization hysteresis measurements shown in Fig. 3. The structural analysis indicates that the substitution of Bi with cation vacancies at the *A*-site enhances the intrinsic ferroelectricity of SBT.

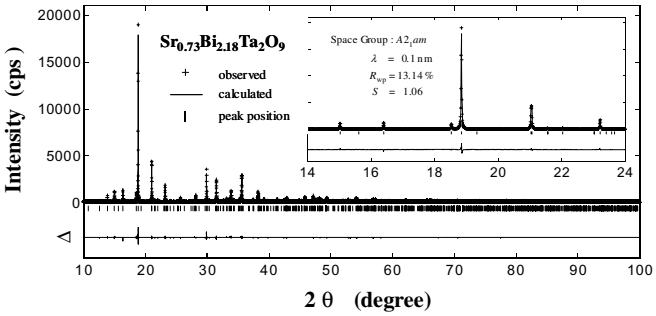

Fig. 1 Result of the Rietveld analysis of the powder synchrotron-radiation diffraction pattern for $Sr_{0.73}Bi_{2.18}Ta_2O_9$. A wavelength of 0.1 nm was used to collect the diffraction data. Δ indicates the difference between the observed and calculated values.

References

[1] T. Noguchi et al., Jpn. J. Appl. Phys., **35**, 4900 (1996).
[2] Y. Noguchi et al., Phys. Rev. B, **63**, 214102 (2001).

* ynoguchi@iis.u-tokyo.ac.jp

10B/2000G238

Structural study of transition metal chalcogenide nanoclusters confined in the zeolite cages

Kenji MARUYAMA*[1], Makoto YAMAZAKI[1], Yuji KUROGOUCHI[1],
Hideoki HOSHINO[2], Takefumi MIYANAGA[2]
[1]Niigata Univ., 8050 Igarashi-2, Niigata, 950-2181, Japan
[2]Hirosaki Univ., 1 Bunkyo-cho, Hirosaki, 036-8560, Japan

Introduction

Transition metal chalcogenides show the very interesting properties. In case of $NiS_{2-x}Se_x$, for example, its magnetism changes from Pauli para- to antiferromagneitic with increasing the value of x at low temperature. These features may be attributable to the interaction between 3d electrons of transition metal and lone pair electrons of chalcogen. So we expect that the nanocluster of these compounds show the new interesting properties by changing the interactions between adjacent clusters.

Recently we have succeeded to produce transition metal chalcogenide nanoclusters in the cage of zeolite LTA(11Å diameter). In order to investigate the structures of these nanoclusters and its temperature dependence, we have performed EXAFS mesurements for Ni-Se nanoclusters with various compositions.

Experimental

The Na^+ cations of zeolite LTA were exchanged with Ni^{2+} ions by using the aqueous $Ni(NO_3)_2$ solution. Zeolite powder was dehydrated at 400 ℃ under vacume of 10^{-6} Torr. Then it was heated with the weighed Se up to 450 ℃ in order to conne Se clusters in the cages. After that, it was heated in H_2 gas up to 350 ℃ for two hours. The obtained Ni-Se clusters were denoted as Se_y-A(Ni_x)red., where x and y represent the number of Ni and Se atoms per cage, respectively, which were determined with ICP mass analysis.

EXAFS spectra around Ni and Se K edge were mesured by using BL10B beam line. The samples were packed into a Teon cell in a glovebox to prevent containing water.

Results and discussion

EXAFS oscillation $\chi(k)$ of Se_y-A($Ni_{3.8}$) obtained around Ni K-edge at 20K were shown in Fig. 1. After the reduction, the prol e of $\chi(k)$ changes very much. The $\chi(k)$ of $Se_{7.6}$-A($Ni_{3.8}$)red. has larger amplitude in high k region (k>10Å^{-1}) than that of $Se_{3.8}$-A($Ni_{3.8}$)red, which suggests the change of the coordination number of Se atoms around Ni atom.

Fig. 2 shows the $\chi(k)$ around Se K-edge for the same samples as Fig. 1. After the reduction, the amplitude of $\chi(k)$ in low k region becomes larger, which suggests the forming of Se-Ni bonds. With increasing the Se, the amplitude of $\chi(k)$ around 5Å^{-1} becomes larger. This indicates that the structure of cluster was changed when the composition was changed.

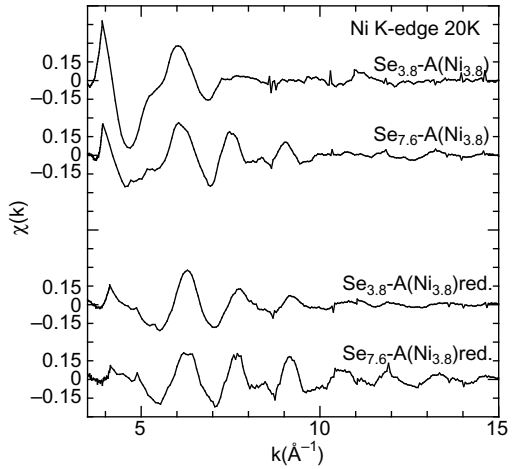

Fig. 1: The EXAFS oscillation $\chi(k)$ of Ni-Se clusters around Ni K-edge at 20K.

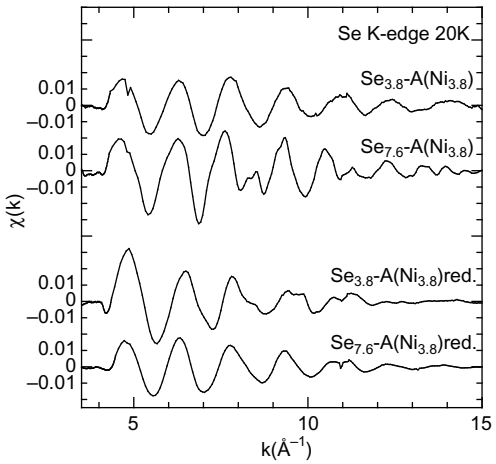

Fig. 2: The EXAFS oscillation $\chi(k)$ of Ni-Se clusters around Se K-edge at 20K.

*maruken@chem.sc.niigata-u.ac.jp

10C/2000G242

Structural study of NIPA/SA gel with low water content

Masaaki SUGIYAMA*[1], Masahiko ANNAKA[2], Kazuhiro HARA[1]
[1]Kyushu Univ., Hakozaki, Higashi-ku, Fukuoka 812-8581, Japan
[2]Chiba Univ., Yayoicho, Inage-ku, Chiba 263-8522, Japan

Introduction

Recently, it has been observed by a small-angle x-ray scattering (SAXS) that a gel with competing bases, such as hydrophobic and hydrophilic bases, in its polymer network exhibits microphase separation by dehydration[1]. The mechanism of this micrpohase separation is considered as follows: because the network of the gel consists of the hydrophobic and hydrophilic moieties, the solvent (water) can not evaporate homogeneously via the different interaction degrees with the hydrophobic and hydrophilic parts in the gel network, therefore as a result, a heterogeneous structure like the islands in the sea can be generated.

Therefore, it is inevitable to observe the structural evolution on dehydration for proof of this hypothesis. In this study, we measured the structure of an *N*-isopropylacrylamide /sodium acrylate (NIPA:hydrophobic, SA:hydrophilic) gel with various water content by the SAXS experiments.

Experimental

Firstly, we prepared for the dehydrated NIPA gels with NIPA/SA ratio of 4:3. Secondly, we added water to the dehydrated gel to reproduce the intermediate state on the dehydration. The amounts of the added water are 0.0 w, 0.5 w, 1.0 w, 1.5 w and 2.0w: w is weight of the dehydrated gel. SAXS experiments are carried out with SAXS apparatus in BL10C of Photon Factory.

Results and discussion

Figure 1(a) shows SAXS profiles of the re-moistened NIPA gel. As you can see, a peak is observed around 0.020 A^{-1}. This means that the gel makes microphase separation. In addition, the peak position is shifted to lower q-region and its intensity shows the maximum between the amounts of the added water of 0.5 w and 1.0w as shown in Fig. 1 (b). The peak position indicates the size of the cluster. Therefore, the cluster consists of SA-rich network part and water complex domain. With increase of the water, the SA and water complex domain gets bigger and at one critical point the relation between water-rich domain (including a lot of SA parts) and water-poor domain (including a lot of NIPA parts) is inversed. In other words, the water-poor domain (including a lots of NIPA parts) is isolated in matrix of water-rich domain in the gel with a lots of the water. We consider that the critical point locates between 0.5w and 1.0w.

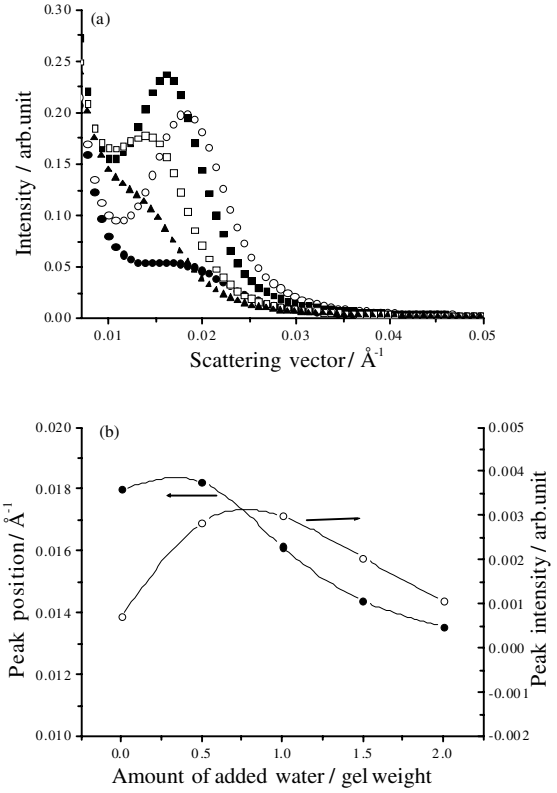

Fig.1. (a) SAXS profiles of the re-moistened dehydrated NIPA gel. Closed circle, open circle, closed square, open square and closed triangle indicate the profiles of the gel added water of 0.0w, 0.5w, 1.0w, 1.5w and 2.0w, respectively. (b) Peak position and intensity distributions of the re-moistened NIPA/SA gel for the amount of added water.

References

[1] M.Sugiyama et al., Jpn. J. Appl. Phys. 38, L1360 (1999).

* sugi8scp@mbox.nc.kyushu-u.ac.jp

12C/2000G246

Structural analysis of C14-type Laves $TiMn_2$ alloy by XAFS

Naoya MASAHASHI, Satoshi SEMBOSHI, Masaki SAKURAI, Shuji HANADA
Institute for Materials Research, Tohoku University, Sendai 980-8577, Japan

Introduction

The hydrogen absorption property of $TiMn_2$ alloy depends on alloy composition severely in the same crystal structure. Repeat process of hydrogen absorption and desorption causes δ-TiH formation and several tens nanometer clustering in atom scale [1]. Hydrogen absorption capacity determined by PCT curves deteriorates with increasing the number of hydrogenation cycle, which is significant for Ti-60 at. % Mn. In this work, the change of interaction between constituent atoms in $TiMn_2$ alloy focusing on hydrogenation was investigated by EXAFS measurement.

Experimental

Four type samples of as-anneal, one cycle-hydrogenation, thirty cycles-hydrogenation and dehydrogenation at 673K after thirty cycles-hydrogenation were prepared for two alloys of Ti - 59 at. % Mn with superior hydrogenation property and Ti - 60 at. % Mn with inferior property. The samples other than as-anneal were supplied by pulverization in PCT experiments and the as-annealed samples were prepared by milling. The X-ray absorption measurement at 20K was carried out with synchrotron radiation using XAFS beam line BL-12C of KEK-PF.

Results

According to Fourier transforms |F(R)| of the EXAFS oscillation functions at the Mn K-edge, the intensity at 2.49Å monotonously decreases with the number of hydrogenation for Ti – 60 at. % Mn, while a drop of the intensity followed by a recovery of the same spectra intensity with increasing of hydrogenation cycles for Ti - 59 at. % Mn. Both samples show a full recovery of the intensity after dehydrogenation. The quantitative analysis of the spectra revealed that the Debye-Waller factors for the first nearest Mn-Mn and Mn-Ti correlation in Ti – 59 at. % Mn are almost constant independent of the process, while they increase with increasing of hydrogenation cycles in Ti – 60 at. % Mn as shown in Fig. 1. The result suggests that the distribution of the inter-atomic distance of Ti – 60 at. % Mn is relatively influenced by the hydrogenation compared with Ti – 59 at. % Mn. It is concluded that the hydrogen absorption capacity of $TiMn_2$ is closely related to the crystallinity of Laves phase.

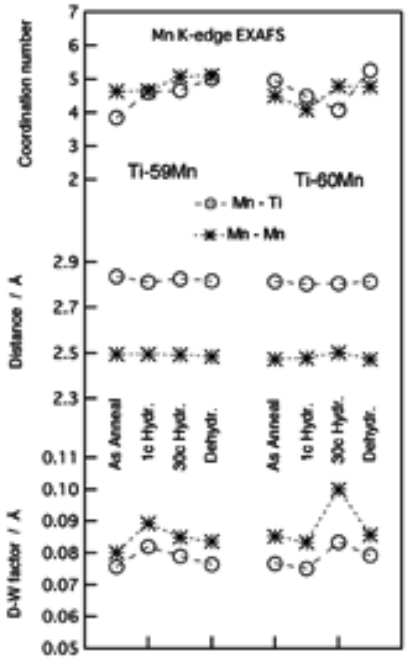

Fig. 1 The coordination number, distance and Debye-Waller factors of Mn-Mn and Mn-Ti in Ti –59 at. % Mn and Ti - 60 at. % Mn of as-anneal, one-cycle hydrogenation, thirty cycles-hydrogenation and dehydrogenation.

References

[1] S. Semboshi, N. Masahashi, S. Hanada: Acta Mater 49, 14 (2001) 927-935.

masahasi@imr.tohoku.ac.jp

10B/2000G253

EXAFS study of liquid Se-Te mixture

Takafumi MIYANAGA*[1], Hideoki HOSHINO[2], Hiroyuki IKEMOTO[3], Hirohisa ENDO[4]
[1] Faculty of Science and Technology, Hirosaki University, Hirosaki, Aomori 036-8561, Japan
[2] Faculty of Education, Hirosaki University, Hirosaki, Aomori 036-8560, Japan
[3] Faculty of Science, Toyama University, Toyama 930-8555, Japan
[4] Faculty of Engineering, Fukui Institute of Technology, Fukui 910-8505, Japan

Introduction

Liquid (l-) Se-Te mixtures have attracted considerable interest because they have covalently bonded chain structure and undergo the semiconductor to metal (S-M) transition at high temperature. Previous EXAFS studies on l-Se-Te mixtures have been carried out by Tamura *et al*[1]. However, their study at 2.5 GeV operation in PF was not sufficient enough in S/N ratio. In the present study we have measured EXAFS spectra at 3.0 GeV operation in which the S/N ratio is much better than those at 2.5 GeV operation. In this paper the changes of the local structure for around Te atoms l-Se-Te mixtures near the S-M transition are reported.

Experimental

The mixtures were prepared by weighing 99.999% pure Se and Te in silica glass ampoules sealed under vacuum. More detailed procedure of sample preparation is described elsewhere[2]. X-ray absorption spectra of Te *K*-edge (31.8 keV) were obtained at BL-10B. An electron beam energy was 3.0 GeV and a stored ring current was 200 mA. Si(311) channel-cut crystal monochromator was used. X-ray absorption spectra were recorded in transmission mode. The samples were put in a quartz cell with appropriate length. The EXAFS interference function was extracted from the absorption spectra and was Fourier transformed by the program of XANADU code described elsewhere[3]. In order to obtain the structural parameters, the EXAFS function was fitted by non-linear least-squares method to the theoretical function, in which theoretical parameters were calculated by FEFF 6 code[4].

Results and Discussion

The previous EXAFS analysis indicates that the short chains in l-Te with metalic nature are composed of the same number of short (~2.80A) and long (~2.95A) covalent bonds and that the long bonds vanish in the semiconducting state at low temperature [5]. In this report we performed 2-shell (Te-Se and Te-Te) fitting. Figure 1 shows temperature variation of the coordination numbers around Te atoms for l-$Se_{40}Te_{60}$. Open circles indicate the coordination number of Se around Te atoms ~2.56A ($N_{Te\text{-}Se}$), open squares Te around Te at ~2.77A ($N_{Te\text{-}Te}$) and closed circles total coordination number (N_{tot}). The values of N_{tot} are about 2.0 at temperature range from 375 to 500C, suggesting that the l-$Se_{40}Te_{60}$ mixture is composed of the chain structure with covalent bonding in this temperature region. With increasing temperature from 500 to 600 C, the value of N_{Total} decreases from 2.0 to 1.5. It is suggested that the S-M transition is accompanied by the appearance of the short chain. More detail analyses are in progress.

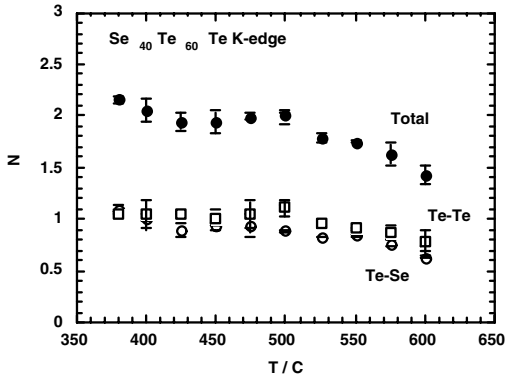

Fig. 1. Temperature variation of the coordination number around Te atoms for l-$Se_{40}Te_{60}$.

References

[1]K.Tamura, M.Inui, M.Yao, H.Endo, S.Hosokawa, H.Hoshino, Y.Katayama and K.Maruyama, J. Phys.: Condens. Matter **3**, (1991) 7495.
[2] H.Endo, H.Hoshino, H.Ikemoto and T.Miyanaga, J. Phys.: Condensed Matter **12** (2000) 6077.
[3] H.Sakane, T.Miyanaga, I.Watanabe, N.Matsubayashi, S.Ikeda and Y.Yokoyama: Jpn. J. Appl. Phys. **32** (1993) 4641.
[4] J.J.Rehr, J.Mustre de Leon, S.I.Zabinsky and R.C.Albers: Phys. Rev. B **44** (1991) 5135.
[5]Y.Kawakita, M.Yao and H.Endo, J. Non-Cryst. Solids, **250-252** (1999) 447.

* takaf@cc.hirosaki-u.ac.jp

12C/2000G255

Mn and Fe K-edges XAFS study of Sn added Mn-Zn ferrite

Masahiro OISHI[1], Keiichi FUKUDA[1], Yasuko TERADA[2], Izumi NAKAI[3]
[1]TDK Corp. R&D Center, Ichikawa, Chiba 272-8558, Japan
[2]SPring-8, JASRI, Hyogo 679-5198, Japan
[3]Science University of Tokyo, Tokyo 162-8601, Japan

Introduction

Mn-Zn ferrite ($(Mn,Zn)Fe_2O_4$) is used for the transformer materials such as AC adapter of the personal computer, power supply for the backlight of liquid crystal monitor. Recently, there have been strong demands to control composition and impurity of Mn-Zn ferrite strictly, because difference in composition and impurity directly changes their magnetic loss (core loss) characters.

It is known that core loss value is related to the amount of Fe^{2+} in Mn-Zn ferrite. On the other hand, we found that a slight amount of Sn in Mn-Zn ferrite caused a drastic change in core loss value. However, how Sn influences the core loss value and which site Sn exists in Mn-Zn ferrite were not yet clarified.

In the present study, we measured Mn K-edge and Fe K-edge XAFS spectra of Mn-Zn ferrite (SnO_2=0 ,0.1 ,0.5 ,1.0 wt%) and discussed the relation between the amount of Sn and Fe^{2+}, and also relation among valence states of Mn and Fe and amount of Sn.

Experimental

Mn-Zn ferrites (SnO_2=0,0.1,0.5,1.0wt%) were prepared for XAFS analysis. Major compositions of Mn-Zn ferrites are Fe_2O_3 (54mol%), MnO (38mol%), ZnO (8mol%). Mn K-edge and Fe K-edge XAFS spectra of these samples were measured in a transmission mode at BL12C, KEK-PF. Powdered samples were diluted with BN and were pressed into disks.

Results and Discussion

Fig. 1 shows Fe K-edge XANES spectra of Fe-foil, Fe_2O_3, Fe_3O_4 and Mn-Zn ferrites with different amount of Sn. Among four Mn-Zn ferrite sample, no difference was found on Fe K-edge XANES spectra. Compared with the reference compounds, the shoulder of Fe K-edge spectra of Mn-Zn ferrite closely resemble Fe_2O_3.

Fig. 2 shows the Fourier transforms of the k^3- weighted Fe K-edge EXAFS spectra. Among four Mn-Zn ferrite samples, no difference was found in the EXAFS spectra. This result is consistent with that of XANES. These spectra also indicate that Mn-Zn ferrites contain Fe^{2+} and Fe^{3+} by the peak of 0.19nm related to the Fe-O bonding.

We also measured Mn K-edge XAFS spectra of these Mn-Zn ferrite samples, but both XANES spectra and Fourier transforms of EXAFS spectra showed no difference among these four Mn-Zn ferrite samples. Compared with the reference compounds, it is found that Mn in Mn-Zn ferrite exist in the Mn^{2+} state.

From these results, we have found that Sn in Mn-Zn ferrite does not have relation between the Fe and Mn state. It is suggested that the core loss's change in Sn added Mn-Zn ferrite is not caused by change of the amount of Fe^{2+} and there may be another factor to effect core loss value.

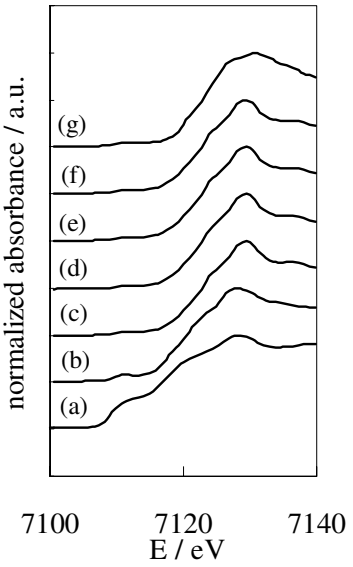

Figure 1. Fe K-edge XANES spectra of (a)Fe-foil, (b)Fe_3O_4, (g)Fe_2O_3, and (c)-(f)SnO_2 added Mn-Zn ferrites: (c)SnO_2 0wt%, (d)SnO_2 0.1wt%, (e)SnO_2 0.5wt%, (f)SnO_2 1.0wt%.

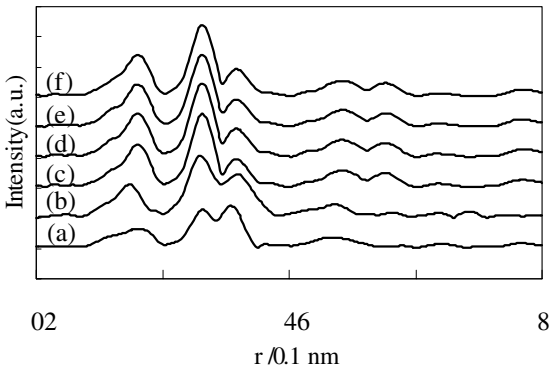

Figure 2. Fourier transforms of the k^3-weighted EXAFS oscillation of (a)Fe_3O_4, (b)Fe_2O_3 and (c)-(f)SnO_2 added Mn-Zn ferrites: (c)SnO_2 0wt%, (d)SnO_2 0.1wt%, (e)SnO_2 0.5wt%, (f)SnO_2 1.0wt%

9A/2000G269

Population of 5-fold coordinated Ti in mesoporous titania

Hideaki YOSHITAKE*[1], Tae SUGIHARA[2], Yasuhide GOA[3], Takashi TATSUMI[2]
[1]Graduate School of Environment and Information Sciences, Yokohama National University, Yokohama 240-8501, Japan
[2]Graduate School of Engineering, Yokohama National University, Yokohama 240-8501, Japan
[3]Graduate School of Engineering, University of Tokyo, Tokyo 113-8654, Japan

Introduction

The mesoporous oxides synthesized by a templating method has been studied intensively for high surface areas, narrowly distributed pore sizes and well ordered mesopore channels. The wall structure is, in most cases, amorphous and the local structures of central atoms, such as Si, Al, and transition metals, of these oxides have not studied well.

Since mesoporous titania synthesized with a primary amine template has an extremely large surface area (> 1200 $m^2 \cdot g^{-1}$) and an amorphous nature, the atomic structure can differ in many points from that in all the other known titanium oxides. We applied XAFS spectroscopies to investigating the local structure of Ti.

Method

The mesoporous titania whose structure was directed by dodecylamine template was prepared according to the literature [1]. XANES spectra of the Ti K edge were recorded on a BL-9A. A conventional transmission mode with detection using gas ion chambers was employed.

Since a pre-edge peak due to *p-d* orbital mixing is observed in most titanium oxides, the pre-edge region in XANES has been analyzed for determining the Ti coordinations. The background of XANES was subtracted by a polynomial function followed by a peak deconvolution with Lorentzian functions and arctangents for transitions to a bound state and the continuous state, respectively.

Results and Discussion

Figure 1 shows the result of a deconvolution of the preedge peak of template-extracted mesoporous silica. The absorption at 4968.8 eV is attributed to 6-fold coordination since the peak top of anatase appears at the same position. The another deconvolution component, peak at 4967.6 eV, is assigned to 5-fold coordination. Figure 1 demonstrates that the deconvolution quantifies the population of $^{[5]}$Ti and $^{[6]}$Ti. The result is summarized in Table 1. Since normalized absorption of anatase and all $^{[5]}$Ti in the oxides measured are 0.3 and 0.8, respectively, and $^{[5]}$Ti turned into $^{[6]}$Ti of anatase by calcinations, the absorption of $^{[6]}$Ti and the population of $^{[5]}$Ti and $^{[6]}$Ti of mesoporous titania can be calculated. The ratio of $^{[5]}$Ti/$^{[6]}$Ti is thus determined to be 0.5.

The most stable low index face of titania single crystals is rutile (110), where $^{[5]}$Ti and $^{[6]}$Ti are equally populated. $^{[5]}$Ti/$^{[6]}$Ti = 0.5 suggests the three Ti layers. The surface area of this face is 1440 $m^2 \cdot g^{-1}$ while the measured BET specific surface area of mesoporous titania is 1256 $m^2 \cdot g^{-1}$, ca. 87 % of 1440 $m^2 \cdot g^{-1}$. The disagreement of $^{[5]}$Ti/$^{[6]}$Ti with the surface area is attributed to the contribution of micropores.

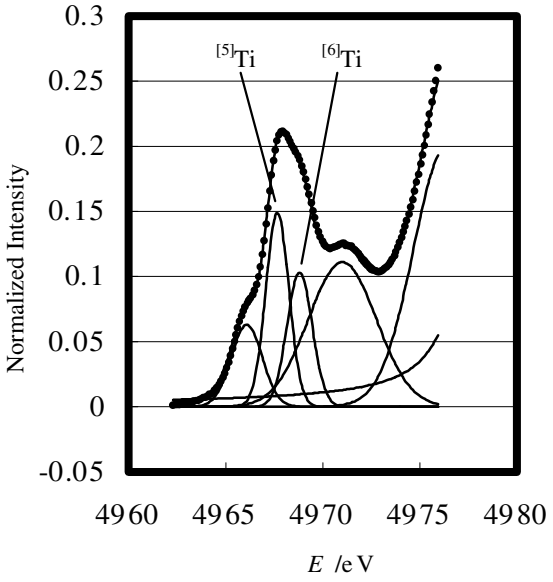

Figure 1. Peak deconvolution of pre-edge peaks of Ti K edge XANES of template-extracted mesoporous silica.

Table 1. Area of Deconvoluted Peaks of XANES Spectra

Sample No.	*I* (4967.6 eV) arb. unit	*I* (4968.8 eV) arb. unit	*I* (4967.6 eV) / *I* (4968.8 eV)
1	1.28	0.77	1.7
2	1.20	0.70	1.7
3	0	1.10	0

Intensity in arbitrary unit. Samples are mesoporous titania before template extraction (1), after template extraction (2), and anatase (3).

The wall structure is, consequently, “porous, ” which is supported by the FT of FEFF generated EXAFS spectrum for rutile(110), demonstrating that this face is more densely packed than mesoporous titania.

Reference

[1] H. Yoshitake, et. al., *Chem. Mater.* **14**, 1023 (2002).

*yos@ynu.ac.jp

4A/2000G279

Dynamic layer response of electroclinic effect in ferroelectric liquid crystals by time resolved X-ray micro-diffraction

Yumiko TAKAHASHI*[1a], Atsuo IIDA[2], Yoichi TAKANISHI[3], Michi NAKATA[3], Megumi TOSHIMITSU[3], Ken ISHIKAWA[3] and Hideo TAKEZOE[3]
[1] The Grad. Univ. for Advanced Studies, Tsukuba, Ibaraki 305-0801, Japan
[2] KEK-PF, Tsukuba, Ibaraki 305-0801, Japan
[3] Tokyo Institute of Technology, O-okayama, Meguro-ku, Tokyo 152-8552, Japan

Introduction

In smectic liquid crystals, the dynamic response of the layer structure upon applying an electric field is of great interest both from device application and fundamental physics. Recently, the irreversible and reversible layer transformation in (anti)ferroelectric liquid crystals has been analyzed with the time resolved micro-diffraction measurement[1]. In a SmA phase, the electric field induces a tilt of the director (electroclinic effect). The electroclinic effect is the fastest electro-optical effects in liquid crystals. This effect has been studied as electro-optical phenomena of molecules, though the local layer response has not been clarified yet.

In this report, the local layer responses to an electric field in SmA phase of FLC cells is measured using time resolved microbeam X-ray diffraction.

Experimental

The experiment was carried out on BL-4A. The x-ray energy was 8 keV. Experiments were performed with a beam size of about 4×4 μm^2. The diffracted intensity was measured by a PSPC as functions of ω and χ angles; ω angle corresponded to a layer rotation angle from the rubbing direction around an average layer direction, and χ angle was a layer deflection angle around surface normal. Time resolved measurements were carried out with a MCS mode and a gated MCA mode for ω and χ-profiles, respectively. X-ray diffraction data were collected synchronized with an applied electric field, which was a triangular form wave of 5 Hz, ±20V.

The sample was TK-C101 (Chisso), sandwiched between ITO-coated glass plates rubbed one-side after coating a polyimide film. The cell gap was 6.8 m. The sample was kept at T_C+1°C during experiments, where T_C was SmA*→SmC* transition temperature (56°C).

Results

The time resolved microbeam x-ray diffraction profiles are shown in Fig.1. The MCS-mode ω-profile measured with 0.2 ms time resolution (b) shows that a peak near ω =1° at low voltage changes to a broad one at high voltage, and peaks appear at both the high and low angle side and change their angular position continuously with applied voltage. Corresponding MCA-mode χ-profiles at ω=1° (c) shows that a single peak shifts depending on the voltage. The absolute angle and the direction of the peak shift depended on the analyzing position. From these results, it is shown that the initial bookshelf structure transforms to the combination of the deformed horizontal chevron and the vertical chevron to compensate the reduction of layer spacing due to the molecular tilt.

With the time-resolved X-ray micro-diffraction, the local layer deformation in the electroclinic effect was revealed for the first time.

References

[1] Y.Takahashi et al. Jpn. J. Appl. Phys. **40**(01)3294, Mol. Cryst. And Liq. Cryst. **365**(01)853

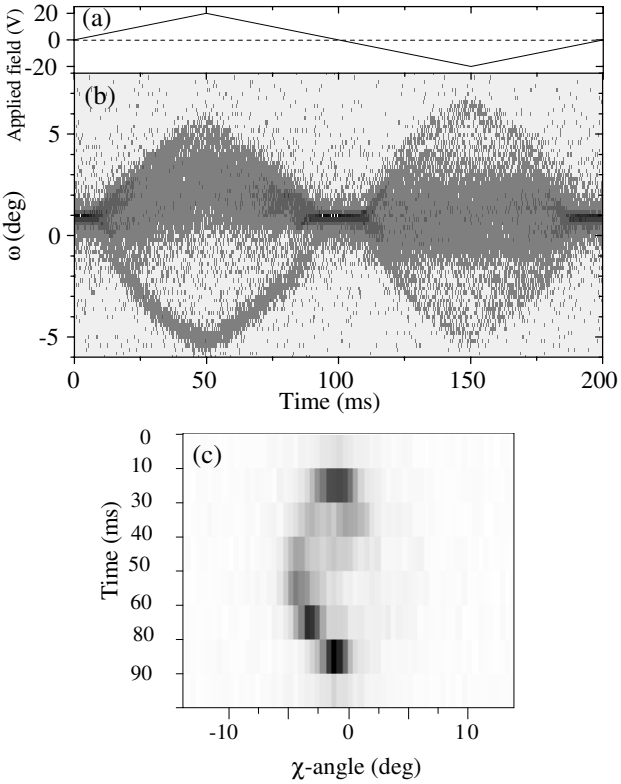

Fig.1 Time resolved micro x-ray diffraction profiles. (a) Applied field, (b) MCS-mode ω-profile, and (c)MCA-mode χ-profiles. 0.2ms and 10ms time resolution for (b) and (c), respectively.

*yumikot@shotgun.phys.cst.nihon-u.ac.jp
a. Present address: Nihon university, Kanda, Chiyoda-ku, Tokyo 101-8308, Japan

12C/2000G287

EXAFS study on local structure of Fe in nano-structured Al alloy

Masaki SAKURAI, Eiichiro MATSUBARA, Makoto MATSUURA*
Kazuhiko KITA#, Hiroyuki SASAKI# and Junichi NAGAHORA#
Institute for Materials Research, Tohoku University, Katahira 2-1-1, Aoba-ku, Sendai 980-8577, Japan
**Miyagi National College of Technology, Nodayama, Natori 981-1239, Japan*
#*Sendai Institute of Material Science and Technology, YKK corporation, Kurokawa 981-3341 Japan*

Introduction

Nano-structured Al-based alloys prepared by electron beam evaporation with small amount of additives can achieve excellent mechanical properties [1]. For the case of Fe additive, grain size decreases and hardness increase with increasing of the amount of Fe up to 5at%. These alloys show x-ray diffraction patterns of super-saturated sold solution of Al. Mechanical properties of these alloys strongly depends on the preparation process of the alloys even the x-ray diffraction patterns do not show clear difference. Hence, it is expected that there is a difference of the local structure around the additive depending on the amount of additives and the sample preparation process. In present work, we study the local structure around Fe atoms in Al-Fe alloy (1.0at% and 2.5at% Fe).

Experimental

Al-Fe alloys were prepared by electron beam deposition with Al and Fe target in a high vacuum chamber. Two types of alloys, Al-1.0at%Fe and Al-2.5at%Fe, were prepared on the substrate of two different temperatures of 100°C and 250°C.

The Fe K-edge XAFS spectra were measured using fluorescence mode at the BL12C station with a double Si(111) monochromator at 20K.

Results and discussion

Fig. 1 shows Fourier transform (F(r)) of the Fe K-edge EXAFS, $k^3 \cdot \chi(k)$, of Al-2.5at%Fe and Al-1.0at%Fe alloys prepared with different substrate temperatures together with those of the simulated results for Fe in fcc Al, Al_2Fe and Al_3Fe intermetallic compounds using FEFF program. Both samples of Al-1.0 and 2.5%Fe samples deposited on the 250°C substrate exhibit similar F(r); one nearest neighbour correlation observed at 2.0Å. On the other hand, the 1.0-at%Fe(100°C) sample exhibit nearest neighbour peak at 2.4Å. While for the 2.5at%Fe(100°C), the F(r) shows two peaks at 2.0 and 2.5Å .

As seen in Fig.1(e), Fe-Al correlation in fcc Al calculated using FEFF locates at 2.5Å. Therefore, it can be concluded that the peak at 2.5Å for the 1.0-at%Fe(100°C) can be attributed to the Fe atoms substituted to fcc Al. On the other hand, the peaks at 2.0Å of the sample for 250°C substrate are very close to nearest Fe-Al correlation in Al_2Fe or Al_3Fe intermetallic compounds. However, long-range correlations are vanished, as seen in Fig.1 (b)-(d). These features indicate that very small (nano-meter size) or distorted intermetallic compound is formed in 250°C substrate alloys.

Mechanical properties of the 1.0-at%Fe(100°C) sample is relatively inferior to other samples. Consequently, these results suggest that the formation of the nano-sized and/or distorted intermetallic compounds in this Al-Fe alloy improves mechanical properties.

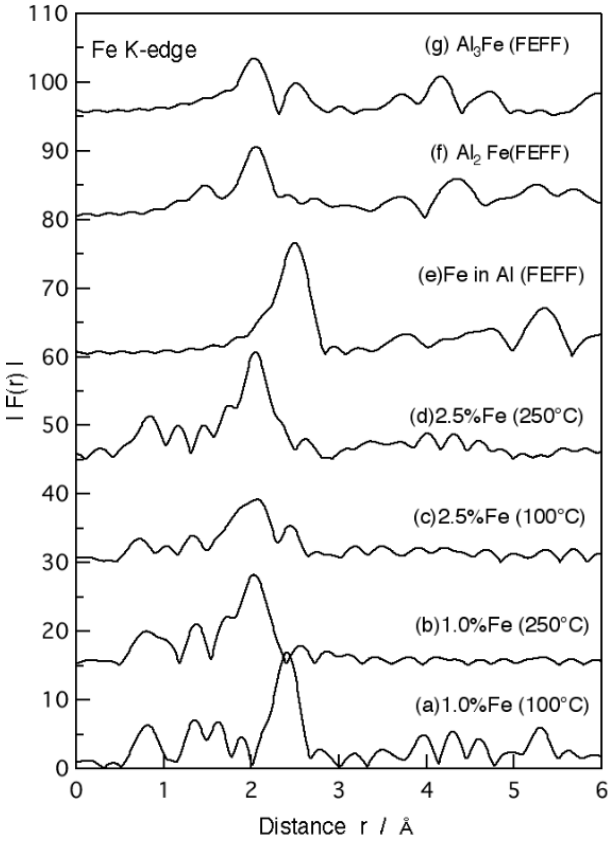

Fig.1 Fourier transform of k^3 weighted Fe K-edge EXAFS of Al-Fe alloys and Fe in fcc-Al, Al_2Fe and Al_3Fe intermetallic compounds calculated from FEFF program.

References

[1] N. Kumagai et al., J. Japan Inst. Metals, 65 366(2001).
[2] J. Nagahora et al., Proc. 2nd Sympo. on SUPER METAL, Japan (1999) pp.39.

* msakurai@imr.edu

12C/2000G288

Dynamic and static disorder of alkali halide solid solutions studied by temperature-dependent extended X-ray-absorption fine structure

Manabu KIGUCHI*[1], Koichiro SAIKI[1], Atsushi KOMA[2]
[1] Graduate School of Frontier Sciences, The University of Tokyo, Bunkyo, Tokyo 113-0033, Japan
[2]Graduate School of Science, The University of Tokyo, Bunkyo-ku, Tokyo 113-0033, Japan

Introduction

A solid solution is a material which is composed of a mixture of atoms or molecules over a range of compositions, and still remains in a single phase. Solid solutions have attracted wide attention not only for fundamental science but also for technological applications, because their properties can be controlled by changing the composition. Although the structures of solid solutions have been well studied and understood, the interatomic potential of solid solutions has not been well understood so far. In the present study, we have studied the interatomic potential of alkali halide solid solutions using temperature dependent EXAFS measurements.

Experiment

$KCl_{0.8}Br_{0.2}$ and $KBr_{0.2}I_{0.8}$ were prepared by mixing appropriate amounts of KBr and KCl or KI, followed by repeated treatments of grinding and melting. Br *K*-edge EXAFS spectra of the solid solutions and KBr were taken by means of the conventional transmission mode at BL-10B in the Photon Factory of the Institute of Materials Structure Science.

Results and discussion

Fig. 1 shows the fourier transform of Br K-edge EXAFS functions of $k^2\chi(k)$ at 32 K, 100 K and 200 K for KBr, $KCl_{0.8}Br_{0.2}$ and $KBr_{0.2}I_{0.8}$. The K-Br bond length and the Einstein temperatures of the K-Br bond for solid solutions were determined by means of the curve-fitting method. The numerical results are shown in Table I. The K-Br bond was contracted by 0.06 Å for $KCl_{0.8}Br_{0.2}$, while it was elongated by 0.09 Å for $KBr_{0.2}I_{0.8}$, as compared to that in KBr. The Einstein temperature decreased with the K-Br bond length, that is, the longer K-Br bond was softer than the shorter K-Br bond. Since the K-Br interatomic potential is anharmonic, the second derivative of the interatomic potential decreases with an increase in the bond length. Therefore, the force constant, that is, Einstein temperature, decreased with the bond length. The static disorder and dynamic disorder could be analysed separately within the Einstein approximation. If the concentration of KBr is low, the static disorder of the K-Br bond in solid solutions was not always larger than that for bulk KBr. The static disorder also increased with the bond length.

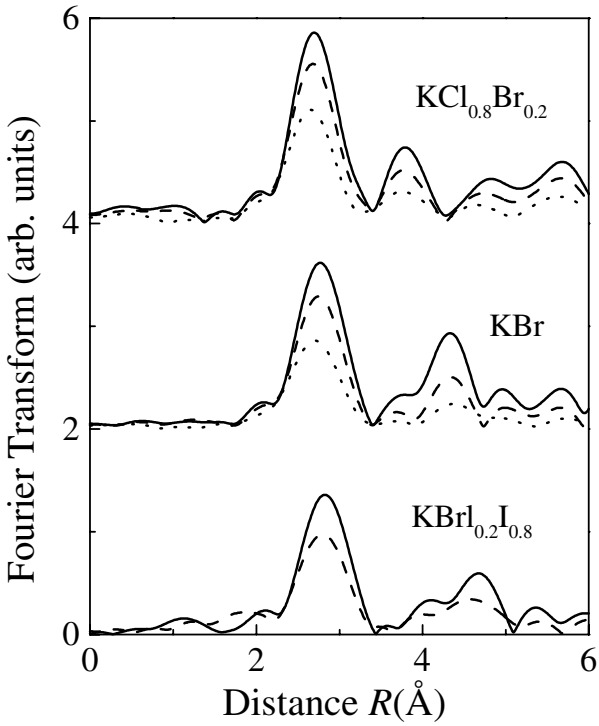

Fig. 1 Fourier transform of Br K-edge EXAFS function of $k^2\chi(k)$ at 32 K (full line), 100 K (dashed line) and 200 K (dot line) for $KCl_{0.8}Br_{0.2}$, KBr and $KBr_{0.2}I_{0.8}$.

Table I: The K-Br bond length and Einstein temperature (ϑ_E) of the K-Br bond for KBr, $KCl_{0.8}Br_{0.2}$ and $KBr_{0.2}I_{0.8}$.

System	*R* (Å)	ϑ_E (K)
KBr	3.26(2)	155(5)
$KCl_{0.8}Br_{0.2}$	3.20(2)	170(5)
$KBr_{0.2}I_{0.8}$	3.35(2)	130(5)

References

[1] M. Kiguchi, K. Saiki and A. Koma, J. Phys. Soc. Jpn. **71**, 1076 (2002).

* kiguchi@k.u-tokyo.ac.jp

19B/2001G011

Co 2p x-ray absorption spectrum of $LaCoO_3$

Yukihiro TAGUCHI*, Kojiro MIMURA, Yoshinao OKABAYASHI, Katsuyuki KITAMOTO, Yoko WATANABE, Kouichi ICHIKAWA, Shuichi KAWAMATA, Osamu AITA
Graduate School of Engineering, Osaka Pref. Univ., Gakuen-cho, Sakai, Osaka 599-8531, Japan

Introduction

$LaCoO_3$ exhibits a gradual nonmagnetic to paramagnetic transition around 100 K. The ground state of Co is the low-spin (LS) state with S=0. It is now considered that the intermediate-spin (IS) state with S=1 is the first excited state and populated thermally through the transition [1]. By assuming these spin states, the magnetic susceptibility is explained qualitatively but not quantitatively [2]. The nature of the transition has yet to be understood fully.

We have studied the Co 3d state of $LaCoO_3$ associated with the magnetic transition around 100 K by using Co 2p x-ray absorption spectroscopy (XAS) with the aid of a CoO_6-cluster model analyses.

Results and Discussion

The sample used was a $LaCoO_3$ single crystal, whose surface was cleaned *in situ* by scraping. Photon energies were calibrated by measuring Au 4f photoemission spectra.

Figure 1 shows the Co 2p XAS (total electron yield) spectra taken at 20 and 250 K. The overall features of the two spectra are like each other and in agreement with previous result [3]. Upon heating, the Co $2p_{3/2}$ and $2p_{1/2}$ peaks are shifted to higher energies, a shoulder around 779 eV decreases and that around 783 eV increases in intensity in comparison with the Co $2p_{3/2}$ peak. According to the magnetic susceptibility analyses [1], over half of Co is excited thermally at 250 K, whereas almost all Co remains in the LS state at 20 K.

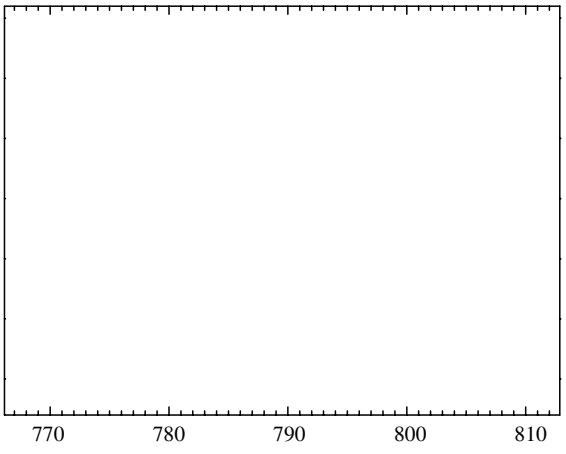

Fig. 1. Co 2p x-ray absorption spectra of $LaCoO_3$ taken at 20 K (solid line) and 250 K (open circles).

We have used a CoO_6-cluster model to analyze the obtained XAS spectra, and assumed that the population of each spin state of Co follows that predicted by the model described in Ref. 1. and that only the first excited state is excited thermally. The calculated results are shown in Figure 2. The parameters used are listed in Table 1.The calculation does not reproduce well the temperature dependence of the observed spectra. The refinement of the parameters used and more detailed simulation by taking into account higher excited states should be necessary.

Fig. 2. Simulated results of temperature dependence of Co 2p XAS spectrum of $LaCoO_3$. Curve LS represents the 20 K-spectrum, and curves IS (300 K) and HS (300 K) the 300 K spectrum by assuming the IS and the high-spin state as the first excited state, respectively.

Table 1: Parameters used in calculation. Values are given in eV, except for Rc and Rv

Δ	U_{dd}	$V(t_{2g})$	U_{dc}	$10Dq$	Rc	Rv
2.0	5.0	3.0	6.0	0.75	0.8	0.9

References

[1] T. Saitoh *et al*., Phys. Rev. B 55, 4257 (1997).
[2] S. Noguchi *et al*., to be published in Phys. Rev. B.
[3] M. Abbate *et al*., Phys. Rev. B 47, 16124 (1993).

* taguchi@ms.osakafu-u.ac.jp

14B ,15C / 2001G031

Rocking curves of iron borate single crystal in rf magnetic field

Takaya Mitsui[1], Yasuhiko Imai[2]
[1]Japan Atomic Energy Research Institute, Kamigori, Ako-gun, Hyogo 678-12, Japan
[2]Japan Synchrotron Radiation Research Institute, 1-1-1 Mikazuki-cho, Sayo-gun, Hyogo 679-5198, Japan

Introduction

Recently, from the viewpoints of fundamental physics research, many scientists have paid attention to the acoustic vibration phenomenon of $FeBO_3$ crystal, which is exposed to rf magnetic field or ultrasonic wave. Because, in such non-equilibrium systems, this crystal can display nonlinear effects [1,2,3], and even magneto acoustic solitons [4]. The influence of acoustic vibration on the crystal deformation of $FeBO_3$ single crystal is a very interesting research subject. Therefore, we carried out the stroboscopic measurements of double crystal X-ray diffraction by using single bunch mode of SR. Then, the acoustic vibration of $FeBO_3$ crystal was excited by rf magnetic field synchronized with SR X-ray pulse.

Experimental Set-up

The synchrotron beam was tuned to λ=1.24Å by Si(111) double crystal monochromator, and was collimated by Si(400) asymmetric reflection (1/b=4.39, ω_h=1.35arcs). The delivered X-ray beam then becomes parallel in comparison with the diffraction width of $FeBO_3$(444) Bragg reflection (ω_h =35 6 arcs), and these crystals fulfill a condition of (+-) parallel setting. An external rf magnetic field was applied parallel to $FeBO_3$(111) plane and perpendicular to scattering plane with various peak amplitudes (0 ~ 16.8Oe) and frequency of 9.61728MHz. The frequency was six times as large as the frequency of SR X-ray pulse (1.60288MHz) exactly. In phase locking, the timing of SR X-ray incidence was fixed in the phase of zero amplitude of rf magnetic field for all measurements.

Rocking curve of $FeBO_3$ (444) in H_{rf}

The rocking curves of $FeBO_3$ (444) reflection were measured with various strengths of rf magnetic field. They are shown in Fig.1. At the strength of rf magnetic field below 4.2Oe (See Figs.1(a) and 1(b)), the measured rocking curves show both sub-peaks and broad tails in a very large angular range (~ 100arcs). These results indicate that this $FeBO_3$ crystal has some defects (misorientations between growth boundaries and crystal bent) in the range of 100 arcs. But, in contrast, at the strength of rf magnetic field over 8.4Oe, the rocking curves change into a sharp form of single peak abruptly. At the same time, strong narrowing of FWHM and enhancement of peak intensity are caused (See Figs.1(c)). Finally, the value of FWHM reaches to 8.0arcs (See Figs.1 (d) and 1(e)). This value is the same order of theoretical the value (the intrinsic FWHM of $FeBO_3$ (444) reflection is about 4.0arcs at λ=1.24Å).

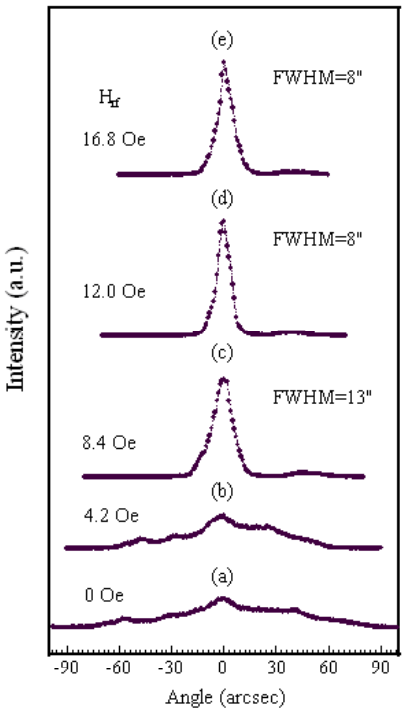

Fig.1. Rocking curves of $FeBO_3$ (444) reflection placed in external fields

These results indicate that rf magnetic field excites the acoustic wave resonantly and it makes a dramatic deformation for $FeBO_3$ crystal surface through magnetostrictive interaction. Surprisingly, the excited magneto acoustic standing wave makes improve $FeBO_3$ crystal perfection extremely. It may be a very important phenomenon for the future's application researches. In recent stroboscopic topography experiment, we could record the visual images of excited magneto acoustic standing wave of $FeBO_3$ crystal too [5].

References

[1] M.V.Chetkin,V.V.Lykov, JETP Lett.52(1990)235.
[2] L.E.Svistov,V.L.Safonov,L.Low,H.Benner, J.Phys:Condens.Matter.6(1994)8051.
[3]Q.Z.Zhang,M.Mino,V.L.Safonov,H.Yamazaki, J.Phys.Soc.Jpn.69(2000)41.
[4]Ozhogin,V.L.Preobrazhenskii, USP.Fiz.Nauk.155(1988)539.
[5] T.Mitsui, Y.Imai, S.Kikuta, Nuclear Instruments and Methods B.(To be published)

*taka@spring8.or.jp

4C/2001G036

An order-disorder phase transition in Al-Ni-Co decagonal quasicrystals by anomalous-X-Ray scattering

Hiroshi ABE*[1], Hiroyuki SAITOH[2], Ken-ichi OHSHIMA[2], Yoshie MATSUO[3], Hironori NAKAO[4]
[1]National Defense Academy, Yokosuka 239-8686, Japan
[2]Univ. of Tsukuba, Tsukuba 305-8573, Japan
[3]Nara women's Univ., Nara 630-8263
[4]Tohoku Univ., Sendai 980-8578, Japan

Introduction

Al-Ni-Co (ANC) system is well known to be decagonal quasicrystals, which have two-dimensional quasiperiodic planes. The structures of ANC depend both on the Ni and Co concentrations and temperature extensively.

In complicated ANC system, it was found that atomic short-range order (SRO) exists by the analysis of the anomalous-X-ray diffuse scattering in $Al_{70}Ni_{15}Co_{15}$ [1]. The diffuse scattering was derived from the random phason strain, which can be coupled with SRO. Further quantitative analysis shows that $Al_{70}Ni_{15}Co_{15}$ has only one kind of a pair correlation function, Ni-Co.

The structure of $Al_{72}Ni_{20}Co_8$ is interpreted as an atomic decoration of the ideal Penrose tiling. Therefore, we can obtain the pure SRO diffuse scattering without the effect of the random phason strain.

Experimental

The diffuse scattering measurements were performed on the BL-4C of the Photon Factory at the High Energy Accelerator Research Organization in Japan. A cylindrical focusing mirror is placed in front of a double monochromator of Si (111). The specimen was mounted on a four-circle diffractometer (Huber 5010). Air scattering was minimized by He filled beam paths. Fluorescence of the scattered beam from the specimen was reduced using a curved highly orientated pyrolytic graphite (002) (Panasonic Co.). The incident X-ray energy was calibrated to within 1 eV using Co foil. The incident X-ray energies were chosen at 7.686 keV near Co K-edge, 8.304 keV near Ni K-edge and 8.098 between them. A high temperature furnace (Mac Science Co.) has two hemispherical Be windows, whose thickness is 1 mm each. In order to analyze the diffuse scattering quantitatively (electron units per atom), we measured the several integrated intensities of a standard powder sample of Ni.

Results and discussion

Figure 1 shows the distribution of the SRO diffuse scattering, where broad peaks are distributed around the superstructure positions only on quasi-periodic planes [2]. The correlation length was estimated to be 2.6 nm approximately. By quantitative analysis, SRO consists of three kinds of pair correlation functions, between Al-Ni, Ni-Co and Co-Al. Each distribution of the SRO diffuse scattering was isotropic. $Al_{72}Ni_{20}Co_8$ has no phason strain. It is also supported by the fact that $Al_{72}Ni_{20}Co_8$ has no $|G^{\perp}|$ dependence of full width at half maximum (FWHM) of Bragg reflections.

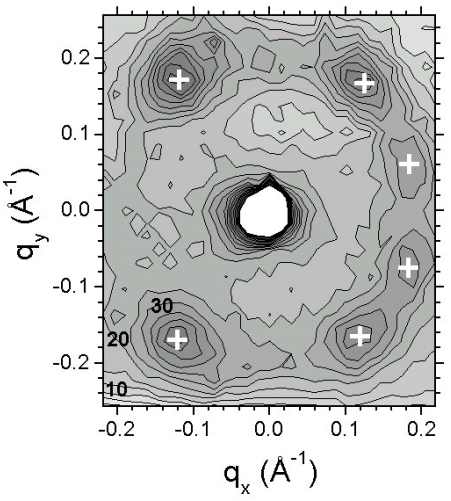

Fig. 1 Diffuse scattering on quasiperiodic plane.

At 965 K ($<T_c$), w eak $|G^{\perp}|$ dependence of FWHM of Bragg reflections appeared [3]. This suggests that weak phason strain appears even in an order-disorder transformation of a perfect quasicrystal. Also, $|G^{\parallel}|$ dependence of those was observed on ordering process. We interpret the ununiform deformation is introduced by the creation and growth of S1-domains below T_c.

References

[1] H. Abe et al., Mater. Sci. and Eng. **294-296**, 299 (2000).
[2] H. Abe et al., Jpn. J. Appl. Phys. **39**, L1111 (2000).
[3] H. Abe et al., J. Alloys and Comp. **342**, (2002) in press.

* ab@nda.ac.jp

14A/2001G045

K emission spectra of lanthanide compounds

Masaaki HARADA[1], and Kenji SAKURAI*[2]
[1]Fukuoka University of Education, Munakata, Fukuoka, 811-4192, Japan
[2]National Institute for Materials Science, Tsukuba, Ibaraki 305-0047, Japan

Introduction

Generally, detailed analysis of x-ray emission spectra can reveal the chemical environments of the specific elements in the materials [1]. The present research aims to investigate K emission lines for lanthanide series elements, mainly in terms of changes in the line intensity ratio [2]. In view of the rather high energy (30~60 keV), however, there are still several experimental difficulties. This report describes some preliminary research for several Gd compounds.

Experimental

X-ray fluorescence (XRF) spectra were collected by an energy-dispersive spectrometer at BL14A with the storage ring operated at 2.9 GeV. The excitation energy was set at 78 keV using a Si(553) monochromator (Gd K-edge is 50.239 keV). The whole detection system is shown in Fig. 1. The fluorescent X-rays were observed by a Ge detector (Canberra GL0055PS) in the perpendicular direction, and energy resolution was estimated as 370 eV at 50 keV (Gd $K\beta_2$). Several kinds of Gd compound powder were prepared as pellets, with a diameter of 8mm and a thickness of 1mm, supported by an aluminum ring.

Results and Discussion

The XRF spectrum of Gd metal is shown in Fig 2. The accumulation time was 10^4 seconds and the dead time was kept at less than 20% under the 12 μs shaping time of the amplifier (Canberra 2021). All the emission lines were assigned as indicated in Fig. 2. The Compton peak of the 78 keV excitation line is observed around 68keV, which is in agreement with the theoretically calculated value in the direction of 90 deg. Gd $K\alpha_1$, $K\alpha_2$, and $K\beta_1$, $K\beta_2$, as well as $L\alpha_{1,2}$, and $L\beta_1$, $L\beta_2$, are observed, although the separation is not always perfect, because of the rather poor energy resolution. In addition, Ge Kα and Kβ escape peaks for some of those lines are visible. One can also see other parasitic lines originating from elements other than Gd; Ta K, Cu K, and Pb L-lines.

Although our interest is mainly in the fine structures of Kβ spectra, both $K\beta_5$ (slightly higher energy side of $K\beta_1$) and $K\beta$-$O_{2,3}$ (slightly higher energy side of $K\beta_2$) were not detected in the present study. Meanwhile, the relative intensity ratio Kβ/Kα was examined precisely for Gd compounds (metal, oxide, fluoride, nitrate, carbonate, and acetylacetonate). However, besides the chemical effects, several factors were found to be affecting the intensity ratio. Detailed analysis is under way. The authors would like to thank Prof. S. Kishimoto for his kind assistance during the experiment.

Reference

[1] L.V. Azaroff, "X-Ray Spectroscopy", McGraw-Hill, (1974).
[2] K.Sakurai and H.Eba, Nucl. Instrum. & Methods B (in press)

*sakurai@yuhgiri.nims.go.jp

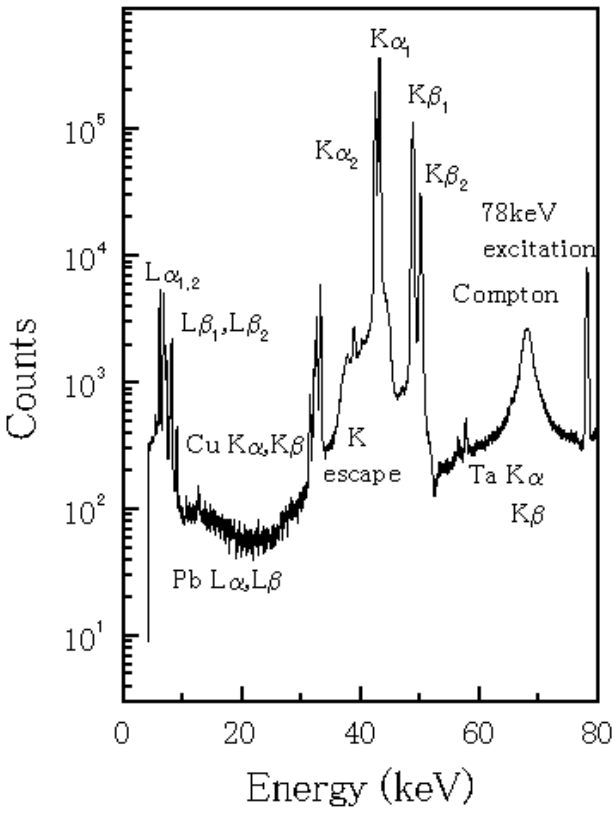

Figure 1 (up) A schematic of the high-energy XRF system.
Figure 2 (right) High-energy X-ray fluorescence spectrum of Gd metal.

15B1/2001G062

Recipe for SR Laue topography of protein crystals

Haruhiko Koizumi, Takashi Uchida, Mitsunori Ishimoto, Miki Shimizu,
Takashi Anezaki, Natsuko Aota, Satoshi Kurita, Ken-ichi Kobayashi
Masaru Tachibana*, Kenichi Kojima
Graduate School of Integrated Science, Yokohama City University, Yokohama 236-0027

The characterization of crystal defects in protein crystals is very important for their technical applications. Laue topography using synchrotron radiation (SR) is one of the most powerful methods to characterize crystal defects because a large number of topographs with different reflections can be obtained by one short exposure. However, protein crystals that include a large amount of water are very fragile. In addition, they suffer radiation damages even in the short exposure. These mean that it is difficult to take SR Laue topographs of protein crystals in the same way as other inorganic crystals. In this paper, we report the recipe for SR Laue topography of protein crystals such as hen egg-white (HEW) lysozyme crystals.

HEW lysozyme crystals were grown at 23°C by the solubility-gradient method [1]. Tetragonal HEW lysozyme crystals (a=b=7.91 nm, c=3.79 nm) of millimeter-size were obtained in the test tube after about two weeks.

The HEW protein crystals with the test tube of 1.0 mm thickness can provide SR Laue topographs with the intense X-ray background due to the test tube. Consequently, the image contrast of crystal defects on the topographs is much poor. Therefore, for the SR Laue topography, the crystal grown in the test tube must be transferred to the thin container that is transparent for white beam. The crystal was carefully skimmed from the solution with fine tip of a soft wood. As shown in Fig.1, the crystal was set inside a short straw of about 0.2 mm thickness, and both sides were sealed with parafilms. The use of the straw was effective for the reduction of X-ray background on the topographs. As the other way, the skimmed crystal was mounted on spider cobwebs crossing a metal ring and sealed with a piece of wetted filter paper. This way for holding the sample is also effective for fragile crystals [2,3].

The high power of the SR white beam gives rise to the radiation damage even in one short exposure. Most of radiation damages are due to the heating of the crystals by irradiating long wavelengths. To avoid the heating, metal plates are usually used as a filter. However, the metal filters were not effective for protein crystals. We considered that the radiation damages for protein crystals are due to the long wavelengths absorbed by the water in the crystals. To avoid the irradiation of the long wavelengths, the water was used as a filter. As a result, the radiation damage was drastically reduced [2,3]. The water filter is very effective for the SR Laue topography of protein crystals. Such recipes should accelerate the study on crystal defects in protein crystals.

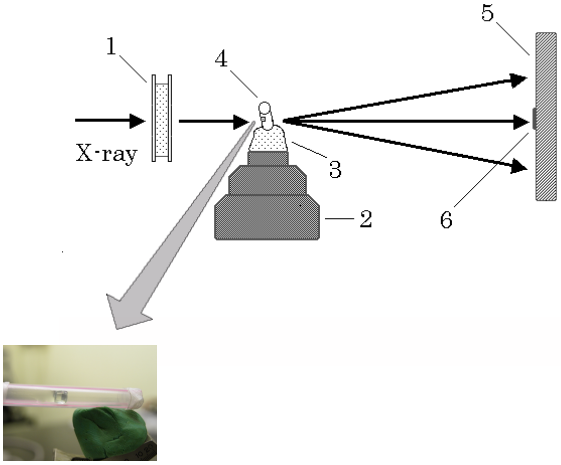

Fig.1 A schematic figure of setting sample for Laue topography using synchrotron radiation.
1.Watre filter 2.Goniometer head 3.Clay 4.Sample 5.File 6.Beam stopper

References

[1] M. Tachibana *et al*., *J. Crystal Growth* **198**-**199**, 661 (1999).
[2] K. Izumi *et al*., *J. Crystal Growth*, **206**, 155 (1999).
[3] M. Tachibana and K. Kojima, *Current Topics in Crystal Growth Research* (in press).

*tachiban@yokohama-cu.ac.jp

1B/2001G064

Pressure effect on the magnetism and structure of a spin-Peierls substance:MEM-[TCNQ]$_2$

K. Ejima[1], T. Tajiri[1], H. Deguchi[1*], M. Mito[1], S. Takagi[1], K. Ohwada[2], H. Nakao[3], Y.Murakami[3]
[1]Faculty of Engineering, Kyushu Institute of Technology, Kitakyushu 804-8550, Japan
[2]SPring-8, Koto Mikazuki-cho Sayo-gun Hyogo 679-5148, Japan
[3]Faculty of Science, Tohoku University, Sendai 980-8578 Japan

Introduction

An organic ion-radical salt, N-Methyl-N-ethyl-morphorinium- [7,7',8,8'-tetracyanoquinodimethane]$_2$ (MEM-[TCNQ]$_2$), is a one-dimensional(1D) spin system and shows a spin-Peierls(SP) transition at the SP transition temperature(T_{SP}) of 18K.

We report the significant pressure effects on the magnetic properties of MEM-[TCNQ]$_2$ [1], though they are rather different from the results reported by Bloch *et al* [2]. In order to clarify such anomalous pressure effects on the magnetism, we have carried out the crystal structure analysis of the substance under pressure by using synchrotron radiation(SR) X-rays.

Experiment

The salt, MEM-[TCNQ]$_2$, was synthesized by the standard method and crystallized by slow cooling of an acetonitrile solution. The susceptibility was measured by using a SQUID susceptometer (Quantum Design MPMS-5) with a hand-made pressure cell in the temperature range of 2-300K and at the pressure up to 8kbar.

The SR X-ray diffraction measurements of the single or powder crystals of the salt under ambient and high pressures have been carried out at the beamline 1B.

Results and Discussion

The paramagnetic susceptibility of the salt at various pressures is shown in Fig. 1 as a function of temperature. The susceptibility at ambient pressure (1bar) clearly shows the spin-Peierls transition at 18K below which the susceptibility suddenly decreases with decreasing temperature. The slight increase of the susceptibility below 7K is attributable to the small amount of paramagnetic impurities. Above 18K, the susceptibility is quantitatively explained by the Bonner-Fisher curve(dashed-line in the Fig. 1) with J/k = -52K.

As the pressure is increased up to 8kbar, the susceptibility at low temperatures becomes large. The susceptibility at above 0.84kbar monotonically increases with decreasing temperature and does no longer show a minimum. The susceptibility at low temperatures and higher pressures obeys the Curie-Weiss law with a very small Weiss temperature. Therefore, the increase of the susceptibility at low temperatures and higher pressures may result from the free spins, which must be produced by separating spin-pairs.

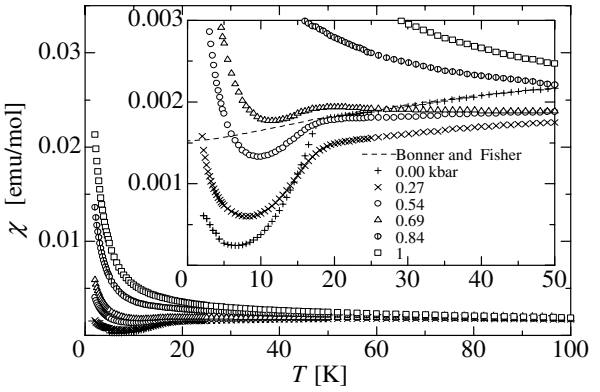

Fig.1. Temperature dependence of the magnetic susceptibility at various pressures.

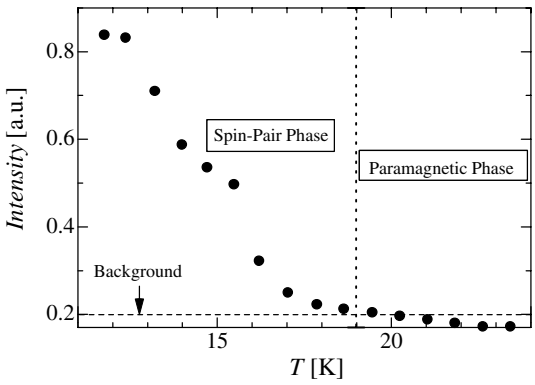

Fig.2. Temperature dependence of the reflection intensity of superlattice in the SP state.

The X-ray reflection resulting from the superlattice in the spin-Peierls state below 18K was clearly observed for a single crystal at ambient pressure. The temperature dependence of the intensity of the reflection is shown in Fig.2. However, the reflection was no longer observed under high pressures. It suggests that the spin-Peierls state is destroyed under pressure, which is consistent with the results of the magnetic measurements. The crystal structure of the salt is rather affected by the pressure even at room temperature.

References

[1] S.Takagi *et al*., Mole.Crys. Liq. Cryst. **376** (2002) 377.
[2] D.Bloch *et al*., Physica **119B** (1983) 43.

* deguchi@tobata.isc.kyutech.ac.jp

4B2/2001G070

Charge-density distribution in calcium titanate perovskite $CaTiO_3$

Masatomo YASHIMA*

Department of Materials Science and Engineering, Interdisciplinary Graduate School of Science and Engineering, Tokyo Institute of Technology, 4259 Nagatsuta-cho, Midori-ku, Yokohama, 226-8502, Japan

Introduction

Calcium titanate perovskite $CaTiO_3$ is one of the most important compounds in materials science and engineering and in earth science. Here I report the charge distribution in the $CaTiO_3$ obtained by the MEM (maximum entropy method)/Rietveld analysis using synchrotron radiation powder data.

Experiments and data processing

To obtain higher angular resolution as possible with good counting statistics, we performed synchrotron X-ray powder diffraction experiments at 25°C for $CaTiO_3$ at the beamline BL-4B2 at the Photon Factory, High Energy Accelerator Research Organization (KEK), Japan (Toraya *et al.*, *J. Synch. Rad.* **3** (1996) 75). A monochromatized 1.2 Å X-ray was used for the measurement. The electron-density distributions were determined by the MEM/Rietveld technique. Computer programs *RIETAN*-2000 (Izumi and Ikeda, *Mater. Sci. Forum* **321-324** (2000) 198) and *ENIGMA* (Tanaka *et al., J. Appl. Cryst.* **35** (2002) 282) were utilized for the calculation.

Results and discussion

Figure 1 shows the fitting result of a preliminary Rietveld analyses in the MEM/Rietveld method of *Pbnm* $CaTiO_3$. Sample spinner during the synchrotron radiation diffraction measurement was very effective to obtain accurate Bragg intensity data. The reliability factors were R_{wp} = 16.10%, R_I = 8.26% and R_F = 4.44%. Goodness of fit was 1.46. Refined unit-cell parameters were a = 5.44322(3) Å, b = 7.64185(5) Å and c = 5.38113(3) Å. Refined structural parameters were x(Ca)=0.03579(7), z(Ca)=-0.00675(12), B(Ca)= 0.323(6)Å^2, B(Ti)=0.059(6) Å^2, x(O1)=0.4838(3), z(O2)=0.0721(3), B(O1)=0.47(3) Å^2, x(O2)=0.2902(2), y(O2)=0.0380(2), z(O2)=0.7101(2), B(O2)=0.40(2) Å^2.

Figure 2 shows the MEM charge-density distributions in $CaTiO_3$. Almost no overlapping electron distribution was observed between Ca-O bonding, indicating an ionic bonding nature. On the contrary, the Ti and O had overlapping electron distributions between them, indicating the covalent feature for the Ti-O bonding.

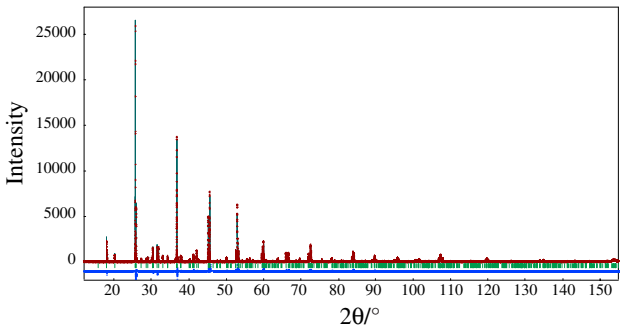

Fig.1. Rietveld pattern of $CaTiO_3$ measured at 25°C.

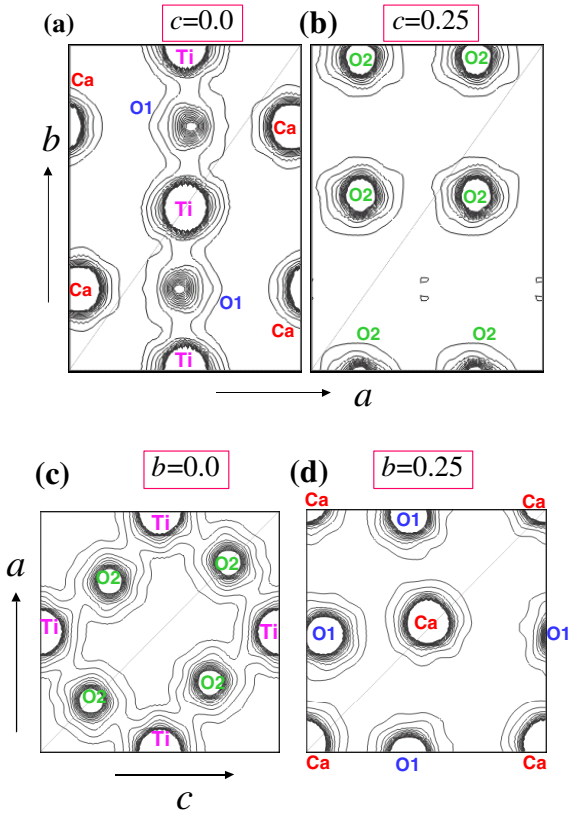

Fig.2. MEM charge-density distributions of $CaTiO_3$; on (a) (001), (b) (004), (c) (010) and (d) (040) planes. The contour lines are drawn from 0.4 to 4.0 e Å^{-3} with 0.2e Å^{-3} intervals.

* yashima@materia.titech.ac.jp

15C/2001G071

Recovery of x-ray energy responses of neutron irradiated semiconductors

Junko KOHAGURA*[1], Teruji CHO[1], Mafumi HIRATA[1], Tomoharu NUMAKURA[1], Ryutaro MINAMI[1], Hiroyuki WATANABE[1], Maiko YOSHIDA[1], Hirokazu ITO[1], Kiyoshi YATSU[1], Syoichi MIYOSHI[1], Junichi HORI[2], Takashi KONDOH[2], Takeo NISHITANI[2], Keiichi HIRANO[3], Hideki MAEZAWA[3]
[1]Plasma Research Centre, University of Tsukuba, Ibaraki 305-8577, Japan
[2]Japan Atomic Energy Research Institute, Ibaraki 319-1195, Japan
[3]KEK-PF, Tsukuba, Ibaraki 305-0801, Japan

Introduction

One of the most critical issues in the use of semiconductor detectors under the circumstances with nuclear fusion produced neutrons is to find a method for recovering the degraded semiconductor response without vacuum break (in situ recovering), or to find out a relation between the degradation effects and neutron fluence into semiconductors. From this viewpoint, we investigate a rather simple and externally controllable method of supplying detector bias to a damaged detector.

Experimental Apparatus

X rays monochromatized with a double-crystal [Si(111)] monochromator (BL-15C) in the energy range of 6 to 20 keV are incident on a semiconductor detector array irradiated with the neutron fluence of 1×10^{13} neutrons cm^{-2} in the Joint European Torus (JET) tokamak. Here, neutrons are produced by deuterium-deuterium (D-D) plasma fusion experiments in JET (2.5 MeV neutrons). The detector array consists of 35 channels with anodes 4.5 mm by 0.96 mm at 0.99 mm spacing with common cathodes. The detector is fabricated using a 300-μm-thick n-type-silicon wafer.

Experimental Results

Figure 1 shows data on the x-ray energy responses of the neutron damaged JET detector array at the applied bias of 1.5 (the filled circles), 3.0 (the open circles), 6.0 (the triangles), and 10.0 V (the squares). Here, we extend to apply our proposed theoretical formula [1-3] under neutron circumstances: The essential terms in the formula are the parameters of d_{dep}, L, and d_{waf}, where d_{dep}, L, and d_{waf} denote the depletion layer thickness, the minority-carrier diffusion length, and the wafer thickness, respectively. The value of d_{waf} is unchanged. Therefore, we need information on the remaining two terms of d_{dep} and L to fit the data in Fig. 1 using the formula. The term of d_{dep} may be effected due to neutron irradiation. In the present report, we directly measure the values of d_{dep} after neutron irradiation by means of an impedance (C-V) analyser. On the other hand, the term of L is tried to be estimated from the data fitting to the x-ray energy response in Fig. 1 under the assumption of the validity of the formula [1-3] even for such a damaged detector. The solid, dashed, dotted, and dot-dashed curves in Fig. 1

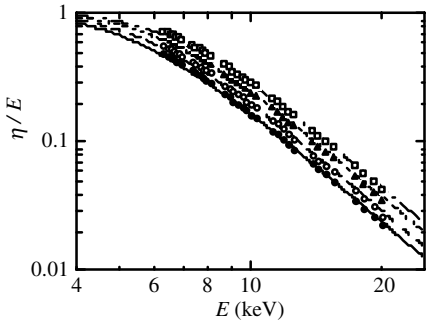

Fig. 1 The x-ray response data obtained from the D-D neutron damaged detector at the applied bias of 1.5, 3.0, 6.0 and 10.0 V are plotted by the filled circles, open circles, triangles, and squares, respectively. The data are well fitted by the theoretical curves (see Refs. [1,2]) using the values of observed d_{dep} at each applied bias along with the same value of L=20±5 μm.

stand for fitting curves to the above four biasing data sets using the values of observed d_{dep} along with the same value of L=20±5 μm for all traces.

The evidence of (i) the availability of the use of the same value L for tracing all data, and (ii) the existence of the degradation as compared with the case of L=50 μm obtained before neutron irradiation implies the availability of the formula even for such damaged detectors. The decrease in L is expected to be interpreted by the formation of trapping centres due to lattice damages for intercepting x-ray created diffusion charges in the field-free substrate region. According to the above mentioned physics interpretations, these damaged energy responses including the applied bias dependence will be calculated when we obtain more detailed dependence formulae for d_{dep} and L as a function of neutron fluence.

References

[1] T. Cho et al., Nucl. Instr. and Meth. A348, 475 (1994).
[2] J. Kohagura et al., Phys. Rev. E 56, 5884 (1997).
[3] J. Kohagura et al., Rev. Sci. Instr. 72, 805 (2001).

* kohagura@prc.tsukuba.ac.jp

10C/2001G076

Crystallization process of poly(ε-caprolactone)-*b*-polybutadiene in a spherical microdomain structure

Satoshi TANIMOTO[1*], Shintaro SASAKI[1], Shuichi NOJIMA[2]
[1]Japan Advanced Institute of Science and Technology, Tatsunokuchi, Ishikawa 923-1292, Japan
[2]Tokyo Institute of Technology, Ookayama, Meguro-ku, Tokyo 152-8552, Japan

Introduction

From recent studies, it was clear that the crystallization in the spherical microdomain structures occurs when the microdomain structure was stables enough [1, 2]. In these cases, the crystal mechanism, the crystallinity, and the crystal morphology should be different from those for the case of crystalline homopolymer because the spherical microdomain structures have disadvantages for the crystallization especially in the vicinity of the interface between the crystalline spherical domain and the amorphous matrix.

In this study, we observed the geometrical changes of the crystallized spherical microdomain structure as a function of the crystallization temperature.

Experimental

The crystalline-amorphous diblock copolymer used in this study was poly(ε-caprolactone)-*block*-polybutadiene diblock copolymer (PCL-*b*-PB) and was synthesized by a successive living anionic polymerization with n-BuLi as an initiator in vacuum (Table 1). The commercially available PB homopolymer (Mw: c.a. 3000) was blended with the PCL-*b*-PB to control the fraction of the crystalline PCL chain in the samples. The percent of PCL-*b*-PB/PB blend was fixed on 20/80 in weight.

Table 1 Characterization of samples.

Notation	Mw[1)]	PCL : PB (vol.%)[2)]
PCL-*b*-PB	8300	40 : 60
PB	c.a. 3000	—

1) Determined by VPO. 2) Calculated from ^{1}H-NMR.

The morphology of the sample was observed by SAXS with synchrotron radiation (SR-SAXS) and conventional SAXS at various temperatures. The SR-SAXS measurement was performed at BL-10C.

Results

Figure 1 shows the typical SAXS intensity profiles for the PCL-*b*-PB/PB blend sample at several temperatures. Each profile shows the scattering peak from the microdomain structure and the broad maxima originated from the form factor. The repeating period in the blend sample was determined from the peak position. And the radius of the spherical structure was evaluated from the curve fitting to the form factor of the isolated sphere.

It was confirmed that after crystallization the intensity maxima assigned to the form factor of the isolated sphere changed in the shape and position as a function of the crystallization temperature. It suggests that the shape of the spherical domain was deformed by the crystallization.

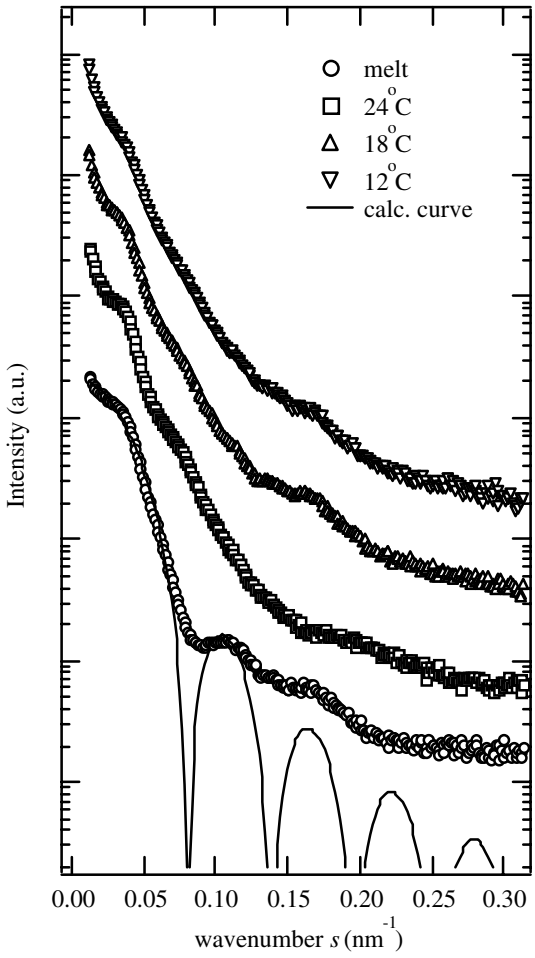

Figure 1. SAXS profiles for PCL-*b*-PB/PB blend at several temperatures. The solid curve is a calculated profile from the form factor of the isolated sphere.

References

[1] A. Rohadi, R. Endo, S. Tanimoto, S. Sasaki, S. Nojima, *Polymer Journal*, **32**, 602 (2000)
[2] S. Nojima, M. Toei, S. Hara, S. Tanimoto, S. Sasaki, *Polymer*, **43**, 4087 (2002)

* tanimoto@jaist.ac.jp

9A/2001G087

Ti K-edge EXAFS on the local structural change of $PbTiO_3$

Takafumi MIYANAGA[1]*, Kei SATO[1], Shigenobu MATSUDA[1], Djibril DIOP[2]
[1] Faculty of Science and Technology, Hirosaki University, Hirosaki, Aomori 036-8561, Japan
[2] Department of Physics, Faculty of Science and Technology, Anta Cheikh Diop University of Dakar, Dakar, Senegal

Introduction

Structural change in perovskite materials have been long studied using by X-ray diffraction and neutron diffraction [1]. On the other hand, X-ray absorption fine structure (XAFS) is a technique to study the local structure of the materials and considered as a complementary technique to the former two methods. During the last two decade, much evidence accumulated indicating that local distortion in perovskite compounds also exist above the phase transition temperature. Sicron *et al*. extensively studied for $PbTiO_3$ EXAFS at wide temperature range [2].

In this report we study the local structural change around Ti atom. We found the discontinuous change of the longest Ti-O(3) distance through the transition temperature as shown in Pb-O(3)[3].

Experimental

Powder sample of $PbTiO_3$ was purchased and sample verification was performed by X-ray powder diffraction method. X-ray absorption spectra of Ti *K*-edges (4.9 keV) were measured at BL9A of Photon Factory (KEK) with transmission mode. Si(111) double crystal monochrometer was used. EXAFS data analyses were performed by XANADU code [4]. In the least-square curve-fitting procedure, the theoretical EXAFS parameters calculated from FEFF6 code [5] were used.

Results and Discussion

Figure 1 shows the EXAFS $k^2\chi(k)$ spectra for Ti *K*-edge at various temperatures. Up to 10 Å^{-1}, satisfactory quality data were obtained.

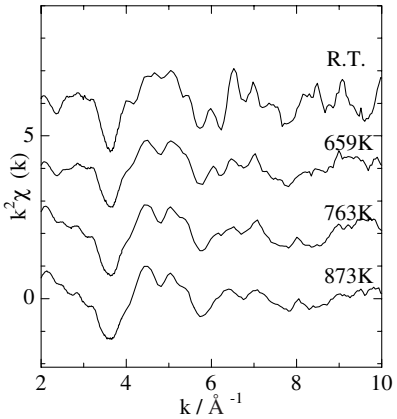

Fig. 1 EXAFS $k^2\chi(k)$ spectra of Ti-*K* edge EXAFS for $PbTiO_3$ at various temperatures.

Using the non-linear least-square-fitting method, we can determine the structural parameters. Figure 2 shows the variations of three kinds of Ti-O interatomic distances with temperature. The interatomic distance of Ti-O(2) is almost constant in whole temperature range. That of Ti-O(3) decreases gradually as temperature increases up to T_c and does not change with temperature over T_c. As for Ti-O(1), we find complex behavior between Ti-O(2) and Ti-O(3). These phenomenon is quite similar to the result of Pb-O(1,2,3) obtained from Pb L_{III}-edge EXAFS study [3]. That is: the longest Ti-O(3) shows the typical "displacive" behavior as well as Pb-O(3) and Ti distortion remains at temperature over T_c.

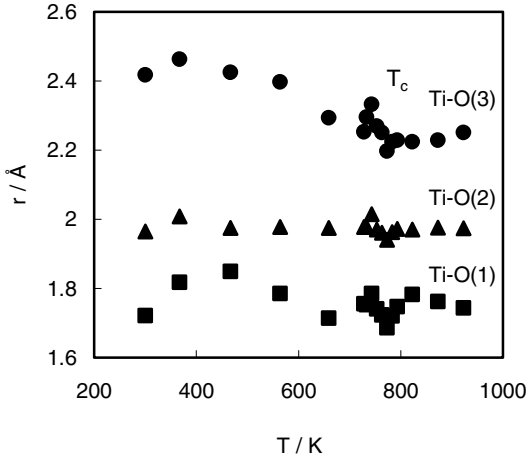

Fig. 2 Temperature dependence of the Ti-O(1,2,3) interatomic distances obtained from EXAFS.

References

[1] F.Jona and G.Shirane, *Ferroelectric Crystals*, Pergamon Press, (1962).
[2] N.Sicron, B.Ravel, Y.Yacoby, E.A.Stern, F.Dogan, J.J.Rehr, Phys. Rev. B, **50**, 13168 (1994)
[3] T.Miyanaga, D.Diop, S.Ikeda and H.Kon, Ferroelectrics, in press.
[4] H.Sakane, T.Miyanaga, N.Matsubayashi, I.Watanabe, Y.Yokoyama, Jpn. J. Appl. Phys., **32**, 4641(1993)
[5] J.J.Rehr, J.Mustre de Leon, S.I.Zabinski and R.C.Albers, Phys. Rev., B **44**, 5135 (1991).

* takaf@cc.hirosaki-u.ac.jp

9A, 10B/2001G090

Local structure around non-crystallized transition metals incorporated in hydroxyapatites

Shigeru SUGIYAMA, * Takuya ICHII, Tomotaka SHONO, Masayoshi FUJISAWA, Daisaku MAKINO, Toshihiro MORIGA, Hiromu HAYASHI
Department of Chemical Science and Technology, Faculty of Engineering, The University of Tokushima, Minamijosanjima, Tokushima 770-8506, Japan

Introduction

It is generally known that, in XRD of hydroxyapatite ($M_{10}(PO_4)_6(OH)_2$; M = divalent cation) incorporated with transition metals, there are no information on the nature of the incorporated species. For examlpe, XRD pattern of strontium hydroxyapatite (SrHAp, M=Sr) is essentially identical to that of SrHAp incorporated with Co^{2+} (Co-SrHAp) [1]. Based on the preparation procedure of Co-SrHAp, the following three situations for Co^{2+} may be suggested: (1) ion-exchanged type as $Sr_{10}(PO_4)_6(OH)_2$ + $Co_{10}(PO_4)_6(OH)_2$ (CoHAp); (2) solid-solution type as $Sr_{10-x}Co_x(PO_4)_6(OH)_2$; (3) Co-supported type as Co/ $Sr_{10}(PO_4)_6(OH)_2$. In this report, XAFS has been employed for the analysis of Co-SrHAp and possible structure of the Co-incorporated material is suggested.

Experimentals

Strontium hydroxyapatite (SrHAp) was prepared from $Sr(NO_3)_2$ and $(NH_4)_2HPO_4$. Into SrHAp, cobalt action was incorporated by stirring the solid and $Co(NO_3)_2{\cdot}6H_2O$ in aqueous solution at 293 K [1]. Undoped SrHAp was treated in the same manner but without the addition of cobalt nitrate. After washing with distilled H_2O and drying 373 K overnight, the sample was calcined at 773 K for 3 h. The incorporated solids are denoted as CoxxSrHAp, with xx equal to 1000Co/Sr (atomic ratio), which is measured with ICP. In order to characterize those samples, XRD (Rigaku RINT-2500X), solid state ^{31}P MAS NMR (Bruker Avance DSX300) and XPS (Shimadzu ESCA-1000AX) were employed together with XAFS. X-ray absorption spectroscopy (XAFS) were measured (2.5 GeV) with a storage ring current of 67 mA at the High Energy Research Organization. The X-rays were monochromatized with channel-cut Si(311) crystals at the BL-10B station for the measurement of XAFS near the Sr-K edge while those were monochromatized with Si(111) double monochromator and the higher order harmonics were eliminated by a focusing double mirror system at the BL-9A station for the measurement of XAFS near the Co-K edge. The absorption spectra were observed using ionization chamber in a transmittance mode. The photon energy was scanned in the range 7.4-8.8 and 15.8-17.1 keV for Co-K and Sr-K edges, respectively. Details of the calculation procedures on XAFS were described in our previous paper [2].

Results and Discussion

XRD patterns of Co-SrHAp were essentially identical to that of SrHAp and information from Co^{2+} in Co-SrHAp were not obtained at all, although ICP and XPS analyses showed that Co is certainly present in bulk and on surface of those samples, respectively. In the XPS spectra of those fresh hydroxyapatites, peaks attributed to Sr $3p_{1/2}$, O 1s, P 2s and Co $2p_{3/2}$ (when present) were found at approximately 280, 531, 190 and 782 eV, regardless of the contents of incorporated cobalt. In order to characterize cobalt species in the cobalt-incorporated catalysts, XAFS and ^{31}P MAS NMR have been employed. The X-ray absorption near-edge structure (XANES) spectra near the Co-K edge of Co55SrHAp and CoO showed that edge position of those samples near the Co-K edge was similar, indicating that the electronic configuration of cobalt-species in Co55SrHAp are not significantly different from that of Co^{2+} in CoO. However the shape of the spectra from those two samples was evidently different. Therefore the site symmetry of cobalt in those two samples was evidently different and Co species in Co55SrHAp was not CoO. Cobalt-oxygen distances obtained by EXAFS analyses of Co-SrHAp and CoO shows that the distances of Co-O in Co36SrHAp (0.204 nm) and Co55SrHAp (0.201 nm) are dissimilar to that in CoO (0.245 nm). Therefore Co species in Co-SrHAp is not Co-supported type as $CoO/Sr_{10}(PO_4)_6(OH)_2$. It should be noted that the nearest distances of Sr-O in SrHAp (0.254 nm) and Co-SrHAp (0.252-0.255 nm) are longer than those of Co-O while XRD patterns of those catalysts were essentially identical. Based on these results and the structure of SrHAp, it may be suggested that Sr^{2+} in SrHAp is replaced by Co^{2+} to afford Co-SrHAp as solid-solution type of $Sr_{10-x}Co_x(PO_4)_6(OH)_2$ while site-center of those cations may be rather different, resulting in the deviation from site symmetry of SrHAp, which can not be detected by XRD but detected by EXAFS. ^{31}P MAS NMR spectra of SrHAp and Co-SrHAp revealed that the intensity of the side band was greater with increasing the content of Co^{2+} in Co-SrHAp, indicating that site symmetry around P species may fall into disorder due to site-positioning of Co^{2+}. Only one ^{31}P MAS NMR peak from SrHAp and Co-SrHAp demonstrates that PO_4^{3-} ions in both unit cells have similar structural environment, suggesting the formation of solid-solution like $Sr_{10-x}Co_x(PO_4)_6(OH)_2$.

References

[1] S.Sugiyama et al., Appl. Catal. A., 211, 123 (2001).
[2] S.Sugiyama et al., Bull. Chem. Soc. Jpn., 74, 187 (2001).

*Sugiyama@chem.tokushima-u.ac.jp

7C, 10B, 12C/2001G099

Structural analysis of Noble metal nanoparticles under supercritical conditions by means of EXAFS

Masafumi HARADA*[1], Yoshifumi KIMURA[2], and Tsutomu OHMORI[3]
[1]Department of Textile and Apparel Science, Faculty of Human Life and Environment, Nara Women's University, Nara 630-8506, Japan
[2]International Innovation Center, Kyoto University, Kyoto 606-8501, Japan
[3]Department of Chemistry, Graduate School of Science, Kyoto University, Kyoto 606-8502, Japan

Introduction

Small metal particles of nanoscale are interesting materials academically and industrially, and the synthesis methods have widely been researched in order to make size-controlled particles. Among various methods, chemical reduction of metal ions using a polymer as a protective reagent is one of the promising ways to prepare small metal particles [1]. Previous application of the high-pressure and high-temperature system to synthesize small metal particles have been mainly limited the cases of metal oxide such as solvothermal reactions in supercritical water [2]. By using the high-temperature conditions of dense fluids which is not possible under ambient pressure, it may be possible to change the rate limiting process to create the nano-particles, which offers another possibility to control the particle size. In this study, we present the results of the synthesis in three different solvent fluids (water, ethanol, and mixture of water and ethanol) at high temperatures and high pressures, and the resulted colloidal dispersions in three different solvents show characteristic features.

Experimental

Concentrated platinum colloidal dispersions ([Pt]=30mM) were prepared from heating of the mixture of $H_2PtCl_6 \cdot 6H_2O$ and poly(N-vinyl-2-pyrrolidone)(PVP) solutions. The preparation conditions of temperature and pressure were 373-573 K and 25 MPa, respectively. Dilute platinum colloidal dispersions ([Pt]=3mM) were also prepared by the same method. The reduced samples were then poured into cells for EXAFS measurements.

Pt-L_3 EXAFS spectra were collected at the BL-10B and/or BL-12C. The EXAFS measurements of the concentrated colloids were carried out at room temperature in a transmission mode at BL-10B, while the measurements of the dilute colloids were performed in a fluorescence mode using a Lytle type detector at BL-12C.

Results and Discussion

Figure 1 shows the Pt-L_3 edge EXAFS Fourier transforms for the obtained solutions of 1:1 mixture of 30 mM Pt/H_2O and 30 g/dm^3 PVP/C_2H_5OH at various temperatures and at 25 MPa. The solution prepared at 373 K shows the same peak position and intensity as the reactant solution, whose peak is assigned to the bond of Pt^+-Cl^-. With increasing the temperature to 423 K, the peak due to the bond of Pt^+-Cl^- vanishes and another peak increases due to the Pt-Pt bond. It is assured that no platinum dioxides are resident after the reduction at high-pressure and high-temperature(>423K). The coordination numbers of Pt atom around the Pt atom is 9.2 0.3, which is almost constant above 473 K, as shown in Table 1.

On the other hand, it is notable that there is a large effect of the solvent on the productivity and dispersity of Pt nano-particles under high temperature in Table 1.

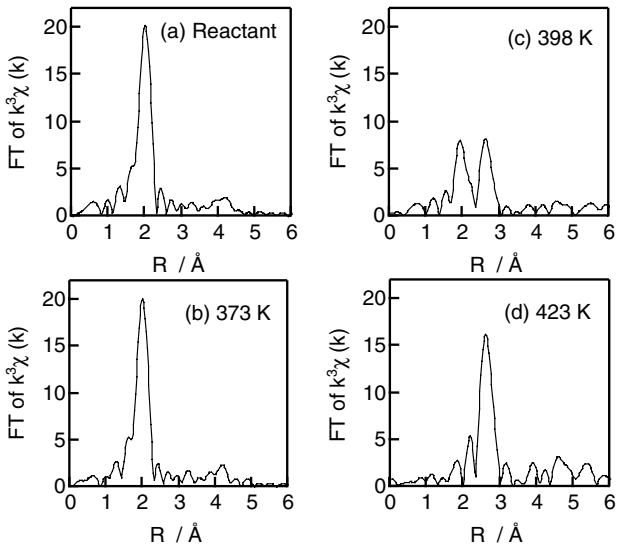

Fig.1 Fourier transforms of Pt-L_3 edge for Pt solutions created at different temperature and at 25 MPa.

Table 1. Curve-fitting results for Pt colloids

T (K)	Pt (mM)	PVP(g/dm^3)	Solvent	C. N.
423	30	30	1: 1	8.4
473				9.2
473	30	30	H_2O	8.0
473	7	3	EtOH	10.1

References

[1] M. Harada et al., J. Phys. Chem. **98**, 2653 (1994).
[2] J. A. Darr et al., Chem. Rev. **99**, 495 (1999).
*harada@cc.nara-wu.ac

9A,7C/2001G119

XAFS characterisation of PtIn catalysts supported on activated carbon

Diego CAZORLA[1*], M.Carmen ROMÁN[1], Juan A. MACIÁ[1],
HiromiYAMASHITA[2], Yuichi ICHIHASHI[2], Masakazu ANPO[2]
[1]Dto. Química Inorgánica, Universidad de Alicante, Apdo. 99, 03080 Alicante, Spain
[2]Dept. Appl. Chem., Osaka Prefecture University, Gakuen-cho, Sakai, 599-8531, Japan

Introduction

Supported PtSn and PtIn are effective catalysts for dehydrogenation or cyclization reactions[1]. However, although the literature about PtSn is well documented, this is not the case for PtIn catalysts. The purpose of the present study is to elucidate the effect of the preparation method and the support surface chemistry in the state of Pt in dried PtIn/carbon samples, and the structure of the metallic particles in reduced catalysts.

Experimental

The catalysts were prepared using solutions of H_2PtCl_6 and $In(NO_3)_2$ following two procedures: i) successive impregnation (first In and then Pt), denoted by SI, and ii) coimpregnation, denoted by C. The Pt loading is about 1wt.% and the atomic ratio Pt/In is 1. Two activated carbons with different surface oxidation (C and C-HP (treated with H_2O_2) were used as support. Drying and reduction were carried out at 383K (overnight) and at 623 K (in H_2 flow, 12 h), respectively. The Pt_{III}-edge absorption spectra were recorded in the transmission mode at RT (E=11300-12700 eV). A FT was performed on k^3-weighted oscillations over the range of 3-12 $Å^{-1}$.

Results and discussion

Dried catalysts

Fig. 1a shows the FT-EXAFS spectra obtained for the samples Pt/C, PtIn/C (SI) and PtIn/C (C) and H_2PtCl_6.

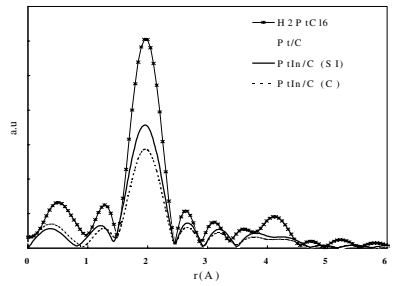

Fig 1. FT-EXAFS of dried catalysts (support C)

These results show an important decrease and/or change in the coordination of Pt upon impregnation. Differences between the three catalysts should be related to the different interaction of the platinum precursor with the carbon support. Such an interaction can take place via coordination with surface oxygen groups and/or via a reduction process in which carbon acts as a reducing agent and as a coordinating ligand [2,3]. For the two bimetallic catalysts, an effect of the preparation method is observed. It can be interpreted as follows: in the SI procedure, surface oxygen groups are occupied by In when the impregnation with the H_2PtCl_6 solution takes place; in the C procedure, however, there is a competence between In and Pt, and more platinum can be coordinated to oxygen. The interaction with oxygen groups can be, as well, conditioned by the chemical state of such groups, that depends on the pH. The analysis of the white line shows that in the supported catalysts, platinum is less electrodeficient than in H_2PtCl_6, what proves the partial reduction of Pt. The presence of indium conduces to a less electrodeficient state of platinum, that can be related either to a different interaction with carbon or to some interaction with In.

In comparison, with the oxidised C-HP support, almost no differences have been found in the structure of Pt in Pt/C-HP and PtIn/C-HP(C) catalysts, but the effect of the surface chemistry is noticeable in sample PtIn/C-HP(SI)). As interpreted above, in an extensively oxidised support, competence for the oxygen surface groups is less relevant. The white line intensity for the three samples is close.

Reduced catalysts

Fig. 2 shows the FT-EXAFS profiles obtained for the reduced samples Pt/C, PtIn/C (SI) and PtIn/C (C) and for a platinum foil (reference). The profiles in Fig. 2 reveal that in the monometallic catalyst, Pt has a structure similar to that of platinum foil (calculated CN is 9).

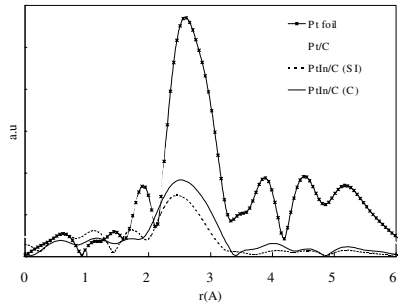

Fig. 2. FT-EXAFS of reduced catalysts (support C).

However, in the bimetallic catalysts, the structure is quite different (the fitting was not possible with Pt foil as a reference). This suggests that some alloying between Pt and In has occurred. The results obtained show some effect of both, the preparation method and, the support surface oxidation in the metallic or bimetallic particles. A deeper investigation of these effects requires the availability of suitable reference, subject of the next work. The XANES region shows that all the reduced bimetallic catalysts give a similar intensity of the white line and of the edge position, that is, after reduction the electronic state of platinum can be considered to be quite similar.

References

[1] F.Pasos et al. J.Catal. 160, 106 and 118 (1996).
[2] H.E. van Dam et al. J. Catal. 131, 335 (1991).
[3] M.C. Román et al. Langmuir, 16, 1123 (2000).
*cazorla@ua.es

12C, 10B/2001G133

Arsenate-iron complex in the pore of functionalized MCM-41

Hideaki YOSHITAKE*[1], Toshiyuki YOKOI[1], Takashi TATSUMI[2]
[1]Graduate School of Environment and Information Sciences, Yokohama National University, Yokohama 240-8501, Japan
[2]Graduate School of Engineering, Yokohama National University, Yokohama 240-8501, Japan

Introduction

Grafting technique of silanes introduces functional groups into the pores of MCM-41, which anchor ions strongly in a proper pH condition. The high surface area, large pores and strong adsorbing properties imply the environmental applicability of functionalized MCM-41. Amino groups in the pores works as adsorbent of oxyanions such as AsO_4^{3-}, CrO_4^{2-}, SeO_4^{2-} and MoO_4^{2-} in pH < 8 [1]. And, in addition, these organic groups anchor certain transition metal cations such as Fe^{3+}, Co^{2+} and Cu^{2+}, which bind the toxic oxyanions selectively. These adsorption centres have a molecular nature and this mode of interaction cannot realize in the adsorption on the minerals. However, the humic materials likely binds both cations and anions though amino group. The clarification of the interactions between cations, anions and organic groups in functionalized MCM-41 will be helpful for understanding the behaviour of these toxic anions in nature and developing effective adsorbents for the area suffering from the pollutions. In this study we analysed the structure of oxyanion–Fe^{3+} complexes anchored by amino groups in the pores of MCM-41 by EXAFS.

Method

MCM-41 prepared by the method in ref. [2] was stirred in toluene containing [1-(2-aminoethyl)-3-aminopropyl]trimethoxysilane and heated to 383 K in dry nitrogen for 6 h. The powder was washed and dried. We denote this diamino-functionalized silica as en-MCM-41. The en-MCM-41 was stirred in 0.1 M 2-propanol solution of $FeCl_3$ for 2 h, washed and dried. The Fe^{3+}-anchored en-MCM-41 is denoted as Fe/en-MCM-41.

50 mg of Fe/en-MCM-41 was stirred for 10 h in 100 ml of aqueous solution of KH_2AsO_4. The concentrations of the oxyanion in the solution were determined by ICP-AES. The detection limit was 1 x 10^{-6} g/L (= 1 ppb). Typical pH value of the solution at the beginning was 2 where the dominant species is $H_2AsO_4^-$.

X-ray absorption experiments were carried out in a transmission mode at BL-9A and BL-10B. The data were processed by EXAFS analysis program REX 2000 (Rigaku). After normalised with using the McMaster tables, k^3–weighted EXAFS oscillation, $k^3\chi(k)$, in 30 – 135 nm^{-1} region was Fourier transformed into a radial distribution function. The amplitude and phase-shift functions were calculated by using the parameter set by Mckale et. al.

Results and Discussion

Figures 1 and 2 shows the Fourier transforms of Fe K-edge and As K-edge in Fe/en-MCM-41 and arsenate adsorbed Fe/en-MCM-41. The unresolved peak at 0.1-0.22 nm in Fe/en-MCM-41 is well fitted with two shells, Fe-N (N = 3.3, r = 0.192 nm) and Fe-Cl (N = 2.1, r = 0.224 nm). No other characteristics are observed in this FT. After adsorption of arsenate, two peaks appear in 0.1- 0.24 and 0.24 – 0.36 nm. These are fitted with four shells; Fe-N (N = 2.9, r = 0.194 nm), Fe-Cl (N = 0.5, r = 0.228 nm) and two Fe-As (N = 1.5, r = 0.327 nm and N = 1.4, r = 0.359 nm). Two kinds of arsenates bound to Fe are distinguished. This is confirmed by the structural parameters obtained in the peaks in Figure 2, where three shells are necessary for a good fitting; As-O (N = 3.9, r = 0.168 nm) and two As-Fe (N = 0.93, r = 0.327 nm and N = 0.40, r = 0.351 nm). At the adsorption saturation, Fe/en-MCM-41 releases a part of Cl^- but retaining the chelate coordination by en.

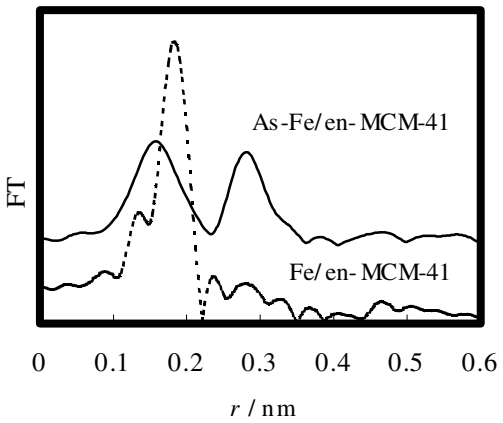

Figure 1. Fourier Transform of Fe K-edge in Fe/en-MCM-41 and arsenate adsorbed Fe/en-MCM-41.

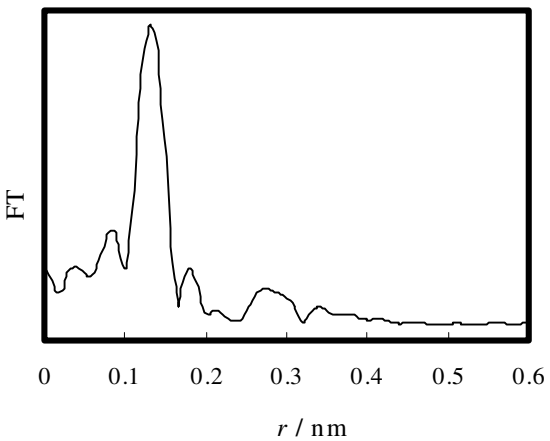

Figure 2. Fourier Transform of As K-edge in arsenate adsorbed Fe/en-MCM-41.

References

[1] H. Yoshitake et al., *Chem. Lett.* **2002**, 586.
[2] H. Yoshitake, et. al. *Stud. Surf. Sci. Catal. in press.*
* yos@ynu.ac.jp

4A/2001G144

Morphology and compositional distribution of Cu-Zn growing electrodeposits

Hiromi EBA and Kenji SAKURAI*
National Institute for Materials Science (NIMS), Tsukuba, Ibaraki 305-0047, Japan

Introduction

Electrochemical deposition of metals from an aqueous solution is an operative way to study a variety of pattern formations observed in growth phenomena [1]. In this study, electrodeposits of a binary system composed of copper and zinc were observed and the relationship between composition and pattern was examined. A non-scanning X-ray fluorescence (XRF) imaging technique [2,3] effective for the 2-dimensional analysis of chemical composition was employed for the dynamical observation of the growing electrodeposits.

Experimental

Electrolysis was performed using a compact cell with a copper wire cathode (0.7mm dia.) and a copper ring anode (i.d. 16mm). An electrolyte of an aqueous solution of copper sulfate and/or zinc sulfate, of which the initial concentrations were 6 ~ 250 mM $CuSO_4$ and 180 ~ 350 mM $ZnSO_4$, respectively, was covered by thin Mylar film and forms a 100~200 m thin layer inside the ring. The DC voltage applied was fixed at 2.5 V in all growing runs.

Results

When the Cu/Zn ratio in the electrolyte is rather large (1/6~3/2), a ramified deposit of short branches similar to pure copper deposits was observed (1). As the Zn concentration increases, the pattern changes gradually: bent branches (2), fine straight branches grown parallel and densely (3), and finally zinc dendrite (4). It was observed from XRF images that both copper and zinc were distributed in branches. Figure 1 shows a typical XRF image of deposits. Pattern (2) can be seen to the left of the cathode (located almost center), and pattern (3) in a limited area to the right. Pattern (1) is also observed in the outer edges. Such differences are due to the inhomogeneous Cu/Zn ratio. Copper ions from the ring anode contributed to such a complex distribution.

The relationship between the chemical composition of the electrolyte (corresponding to 4 types of patterns) and that of the deposits is summarized in Fig.2. When pure copper deposit-like pattern (1) is observed, the compositions are in the region of the α (copper and solvent solution by adding zinc), β' or γ phases. A typical powder XRD pattern (inserted in Fig. 2) indicates the existence of each phase of α, ε and η. On the other hand, for the bent deposits (2), both the XRD pattern and the chemical composition agree well with the hexagonal ε phase (represented as $CuZn_4$ or $CuZn_5$). The authors would like to thank Prof. A. Iida for his valuable discussions and kind assistance during the experiment.

References

[1] T. Vicsek, *Fractal Growth Phenomena*, 2nd edition (World Scientific, Singapore, 1992).
[2] K. Sakurai and H. Eba, Japanese Patent No.3049313 (2000).
[3] K. Sakurai and H. Eba, PF Activity Report #17, 321 (1999).
*sakurai@yuhgiri.nims.go.jp

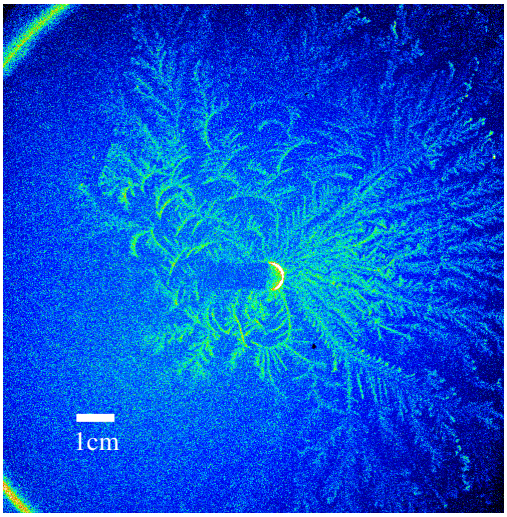

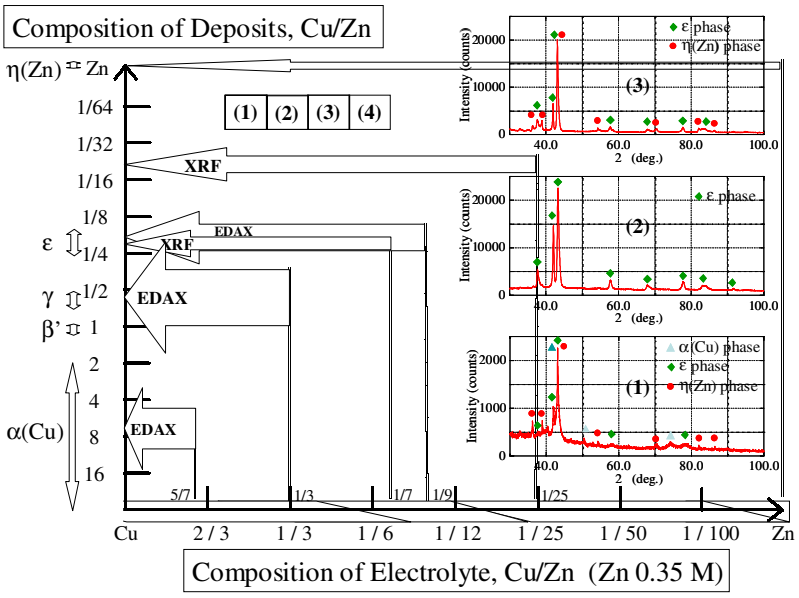

Fig.1 (left) XRF image of electrodeposits from 300 mM $CuSO_4$ and 350 mM $ZnSO_4$ aqueous solution. The pattern started from the cathode (located almost center). Incident energy : 8 keV. Exposure time, 2 min.

Fig.2 (right) Summary of crystal phases of Cu-Zn binary deposits. Four types of phases were obtained for different chemical compositions.

28B/2001G232

Magnetic EXAFS for Ni-Mn alloys

Takafumi MIYANAGA[1]*, Teiko OKAZAKI[1], Ryota MARUKO[1], Shin-ichi NAGAMATSU[2], Takashi FUJIKAWA[2]

[1]Department of Materials Science and Technology, Faculty of Science and Technology, Hirosaki University, Hirosaki, Aomori 036-8561, Japan

[2]Graduate School of Science, Chiba University, Yayoi-cho 1-33, Inage, Chiba 263-8522, Japan

Introduction

The Ni_3Mn alloy forms an ordered phase of Cu_3Au type with suitable heat treatment [1]. The magnetization depends on the number of nearest-neighbor Mn atoms around a Mn atom for Ni_3Mn [2]. According to heat treatment Mn atoms are substituted into the Ni atoms in the lattice as each Mn atom is located at the corner positions of f.c.c. lattice. These Mn pairs show ferromagnetic interaction. The magnetic EXAFS is powerful and direct method to study the local magnetic structures for such an alloy.

In this report we study the magnetic EXAFS of Mn *K*-edge for $Ni_{0.76}Mn_{0.24}$ alloy. We compare the experimental spectra with semi-relativistic theoretical calculation.

Experimental

The appropriate quantities of 99.99 % pure Ni and Mn were melted in Ar gas by the rf induction furnace, and then the ingot was homogenized by holding in a vacuum for 15 h at 1273 K. The foil samples of $Ni_{0.76}Mn_{0.24}$ prepared by polishing and annealed at 693 K for 100 hours in a quartz tube sealed under Ar atmosphere in order to obtain certain degrees of atomic order. The magnetic EXAFS spectra were measured at BL28B in transmission mode using the left-circularly polarized X-ray.

Theory

The semi-relativistic calculation for magnetic EXAFS was applied to NiMn alloys. The formalism of the calculations are presented elsewhere [3].

Results and Discussion

Figure 1 shows the Fourier transforms of the EXAFS. The *k*-range of the Fourier transform is 2.0~10.8 $Å^{-1}$. Solid lines presents magnetic and dashed line does non-magnetic EXAFS. Vertical arrows in Fig. 1 denote the crystallographic positions of nearest neighbour atoms in Ni-Mn f.c.c lattice from central Mn atom. The non-magnetic EXAFS shows these contributions quite normally. On

1B/2001G245

High-pressure x-ray diffraction study on $Pr_{0.65}Ca_{0.35}MnO_3$

Susumu Shimomura*, Kengo Nishimoto, Tetsuji Ogata, Yasushi Yamanaka, Yoshiaki Naito, Keisuke Tajima, Nobuyoshi Wakabayashi, Ryoko Tazaki[1], Hiroshi Sawa[2], Hironori Nakao[2], Yasuhide Tomioka[3,4], and Yoshinori Tokura[3,4,5]
Dept. of Phys., Keio Univ., 3-14-1 Hiyoshi, Kohoku-ku, Yokohama 223-8522, Japan
[1]Grad. School of Sci. and Tech., Chiba Univ., Chiba 263-8522, Japan
[2]KEK-PF, Tsukuba, Ibaraki 305-0801, Japan
[3]JRCAT, Tsukuba 305-0046, Japan
[4]CERC, AIST, Tsukuba 305-8562, Japan
[5]Dept. of Appl. Phys., Univ. of Tokyo, Tokyo 113-8656, Japan

Introduction

The mixed valence system of manganese oxides with distorted perovskite structures, $A_{1-x}B_xMnO_3$, shows the colossal magnetoresistance and other novel phenomena. These phenomena have been interpreted by the strong coupling among the charge, orbital, spin and lattice. In $Pr_{1-x}Ca_xMnO_3$ ($0.3 \leq x \leq 0.5$), the charge ordering transition takes place at T_{CO}~230K[1]. The cooperative Jahn-Teller ordering associated with the orbital ordering simultaneously occurs, and this results in the doubling of the crystallographic unit cell. The charge and orbital ordered insulating phase is transformed into the disordered metallic phase by applying magnetic fields. Recently we have measured the temperature and pressure dependences of the superlattice reflections attributed to the charge and orbital ordering in $Pr_{0.65}Ca_{0.35}MnO_3$. We found an indication of an additional phase transition in a limited region of pressure and temperature where the superlattice reflection intensity shows an anomalous increase. We have conducted x-ray diffraction experiments at low temperatures and high pressures in the compound with x=0.35 in order to reveal the characteristics of the pressure-induced phase.

Experimental

The x-ray diffraction measurements were performed at the BL-1B of the Photon Factory. The x-ray energy was 18.0 keV. A single crystal of $Pr_{0.65}Ca_{0.35}MnO_3$ was placed in a diamond anvil cell. Ruby fluorescence scale was used for pressure determination. The diamond anvil cell was mounted on a cold head of a closed-cycle refrigerator. The diffracted intensities were recorded on an image plate.

Results and Discussion

Figure 1 shows a typical oscillation photograph taken at 180K and 1.85GPa, where the charge and orbital ordered state is stable. The superlattice reflections were observed below T_{CO}. These reflections can be indexed as (h, k+1/2, l) on the basis of the fact that the sample consists of the domains due to the pseudo-cubic structure. For further increasing pressure and lowering temperature, the superlattice reflections abruptly disappear. This indicates that the charge and orbital ordered phase is transformed into the ferromagnetic metallic phase. The anomalous changes in the superlattice reflection intensities were also observed in the limited pressure and temperature region. These changes suggest that rearrangement of charge and orbital ordering takes place. No additional reflections were observed, but there is a possibility that new reflections at specific positions are not distinguishable due to the existence of the pseudo-cubic domains.

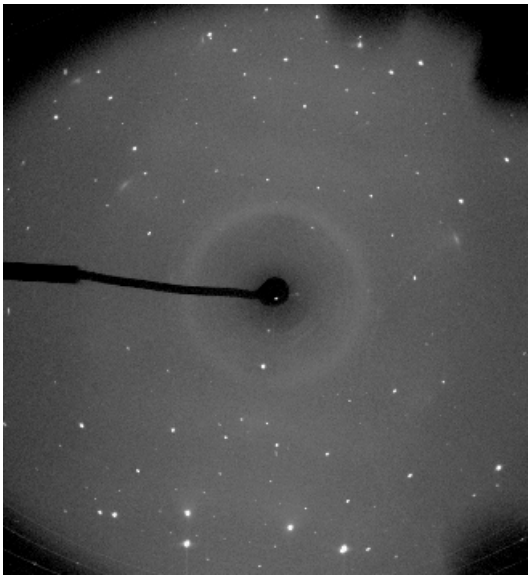

Fig.1 An x-ray oscillation photograph of $Pr_{0.65}Ca_{0.35}MnO_3$ taken at 180K and 1.85GPa.

References

[1] Y. Tomioka et al., Phys. Rev. B 53, R1689 (1996).

* simomura@phys.keio.ac.jp

3A/2001G246

X-ray fluorescence holography of Nd_2CuO_4

Kouichi HAYASHI[1*], Yukio TAKAHASHI[1], Ei-ichiro MATSUBARA[1], Takeharu MORI[2], Masahiko TANAKA[2], Hirotaka YAMAGUCHI[3]
[1]Tohoku Univ., 2-1-1 Katahira, Aoba-ku, Sendai 980-8577, Japan
[2]KEK-PF, Tsukuba, Ibaraki 305-0801, Japan
[3]AIST, Tsukuba, Ibaraki 305-8568, Japan

Introduction

X-ray fluorescence holography (XFH) is a promising method for determination of a local environment around a particular element. One of most important applications of XFH is an observation of local lattice distortion of superconductor or colossal magnetic resistance materials induced by phase transition. In the present study, Nd_2CuO_4 was used as sample of XFH, and visualized local atomic images around Cu.

Experimental

A dimension of Nd_2CuO_4 single crystal (001) was $5 \times 5 \times 2.0$ mm^3, was used as the measured sample. The incident energies were 17.0 - 19.5 keV with 0.5 keV steps. Cu Kα radiations emitted from the sample were analyzed and focused by the toroidally bent graphite analyzer. The focused fluorescence photons were detected by the APD. The intensities of Ge fluorescence was measured as a function of the azimuthal angle ϕ and polar angle θ within the range of $0° \leq \phi \leq 360°$ and $20° \leq \theta \leq 70°$.

Results and Discussion

The collected data was processed by normalization with respect to incident intensities, removal of the large background, symmetrization using standing wave lines and low-pass filtering. Figure 1 shows a typical hologram pattern of Nd_2CuO_4 recorded at 18.0 keV. Atomic images were reconstructed from six holograms. Figures 2 (a), (b) and (c) show the planes parallel to the {001} lattice planes taken at distance of z = 0, 1.6 and 4.5 Å, respectively. Cu and Nd atoms were clearly visible. However, O atoms were not visible.

*khayashi@imr.tohoku.ac.jp

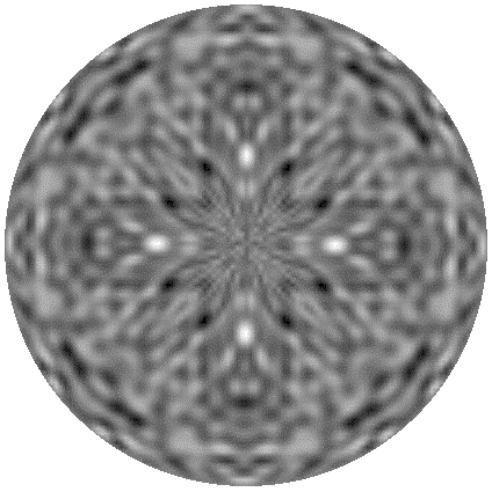

Fig. 1 X-ray hologram of Nd_2CuO_4. The incident energy was 18.0 keV.

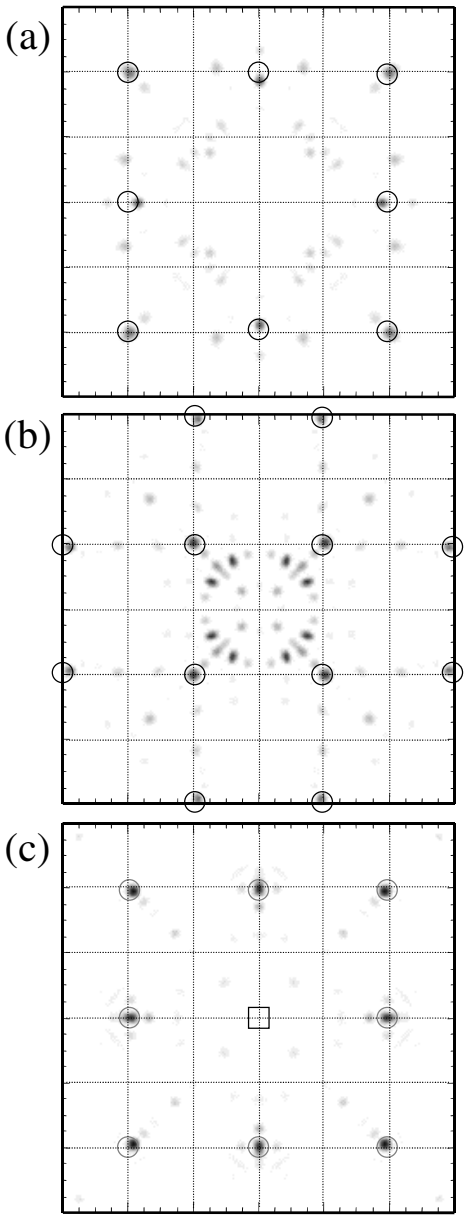

Fig. 2 Atomic images reconstructed from six holograms. Planes parallel to the {001} lattice planes taken at distance of z = (a) 0, (b) 1.6 and (c) 4.5.

9 C, 15A/2001G269

Study on crystallization and spherulite growth of poly(ethylene) in phase-separated polymer blends

Shinichi SAKURAI[1], Kyoko HAYASHI[1], Shigeo HARA[2], Katsuhiro YAMAMOTO[2] and Shigeru OKAMOTO[2]

[1]Department of Polymer Science and Engineering, Kyoto Institute of Technology, Matsugasaki, Sakyo-ku, Kyoto 606-8585, JAPAN

[2]Department of Material Science and Engineering, Nagoya Institute of Technology, Gokiso-cho, Showa-ku, Nagoya 466-8555, JAPAN

Introduction

Crystalline polymer has structural hierarchy, which affects its mechanical property. Especially, it is significant to study and control spherulite growth because spherulite stays at the top of the structural hierarchy. It has been reported in our previous study that spherulite can grow bigger than phase-separated domains in rapid cooling process. For blends of LLDPE (linear low density polyethylene) with rubbery polymers, effects of phase-separated domains on spherulite growth and crystallization of LLDPE were studied by focusing the radius of spherulite and the long period of crystalline lamellae in isothermal crystallization process. The former was evaluated from small-angle light scattering (Hv-SALS) measurements and the latter was examined by the small-angle X-ray scattering technique (SAXS). The crystallinity was evaluated as well by the wide-angle X-ray scattering technique (WAXD).

Experimental

Simultaneous SAXS/WAXS/Hv-SALS measurements were conducted at the BL-9C beamline. Figure 1 shows the schematic diagram for the simultaneous SAXS/WAXS/Hv-SALS equipment at the BL-9C beamline Simultaneous SAXS/WAXS measurements were also conducted at the BL-15A beamline. The wavelength of X-ray was tuned at 0.154 nm. A set of position-sensitive proportional counters were used.

Results and Discussion

Fig. 2 shows an example of two dimensional Hv SALS pattern. (LLDPE/SEBC=80/20). Here, the half of the four-leaf pattern, which is attributed to a spherulite, was detected. From the peak position appeared in the direction with the azimuthal angle μ = 45°, the radius of spherulite can be evaluated.

It was found, in some particular cases, that the spherulites were 10 times lager than the phase-separated domains, which was analyzed by the transmission electron microscopy. It was also found that the rate of spherulite growth in a neat LLDPE is faster than in the phase-separated blend of LLDPE with a rubber polymer.

shin@ipc.kit.ac.jp

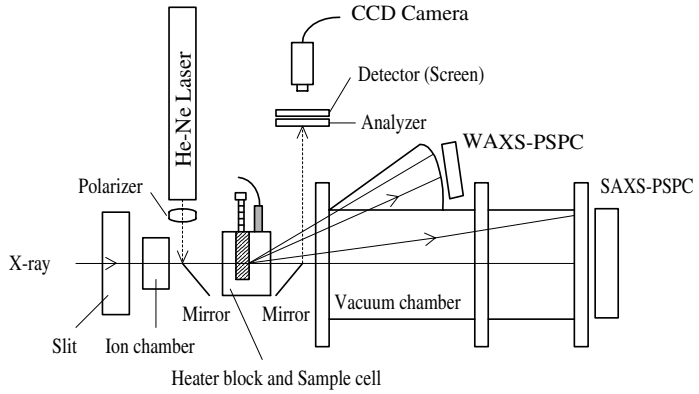

Fig. 1 Simultaneous synchrotron SAXS/WAXS/ Hv-SALS equipment (PF BL-9C).

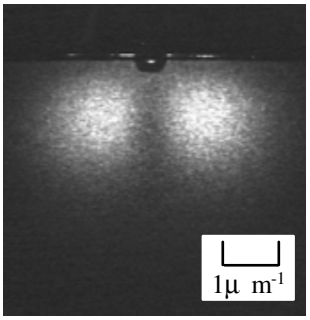

Fig. 2 Example of two dimensional Hv SALS pattern. (LLDPE/SEBC=80/20)

9 C, 10C/2001G270

Structural analysis of a thin film of an SEBS triblock copolymer forming spherical microdomains

Shinichi SAKURAI*[1], Akiko SAKAMOTO[1], and Shigeru OKAMOTO[2]
[1]Department of Polymer Science and Engineering, Kyoto Institute of Technology, Matsugasaki, Sakyo-ku, Kyoto 606-8585, JAPAN
[2]Department of Material Science and Engineering, Nagoya Institute of Technology, Gokiso-cho, Showa-ku, Nagoya 466-8555, JAPAN

Introduction

Various different kinds of supermolecular structures have been found in microphase-separated structures of block copolymers. We report here an experimental result of the transformation of packing order of spherical microdomains in block copolymer thin film.

Experimental

The sample used is polystyrene-*block*-poly(ethylene-co-but-1-ene)-*block*-polystyrene triblock copolymer (SEBS) having Mn = 6.7×10^4, ϕ_{PS}=0.084 , M_w / Mn=1.04. Thick films were prepared by solution casting from a 5wt% w/v solution of the SEBS in toluene on silicon wafers. Thin films were prepared by spincoating from a 0.5wt% w/v solution of the SEBS in toluene on silicon wafers. All samples were annealed under vacuum at 140°C for 12h. Annealing is essential to obtain well-ordered spherical microdomain structures.

Results and Discussion

Atomic force microscopy (AFM) revealed that spherical microdomains ordered hexagonally on the free surface of the thin film from the 0.5wt% solution (Fig. 1) and the thick film from the 5wt% solution.

Fig. 2 shows the results of small-angle X-ray scattering (SAXS) experiments for thin films spin-cast on the cover glass. The SAXS profile for the thin film from 5 wt% solution exhibits the diffraction peaks at relative positions $1:\sqrt{2}:\sqrt{3}$, suggesting BCC (body-centered cubic) packed spheres in bulk. Thus, the free surface of the thick film from the 5wt% solution might be covered with a (111) plane of the BCC lattice. However, thus deduced lattice constant was just the half of the bulk one. It is rather reasonable to consider that the spherical microdomains at the free surface of the film are ordered in FCC lattice, giving rise to the hexagonal surface cleavage with a (111) plane of the FCC (face-centered cubic) lattice.

*shin@ipc.kit.ac.jp

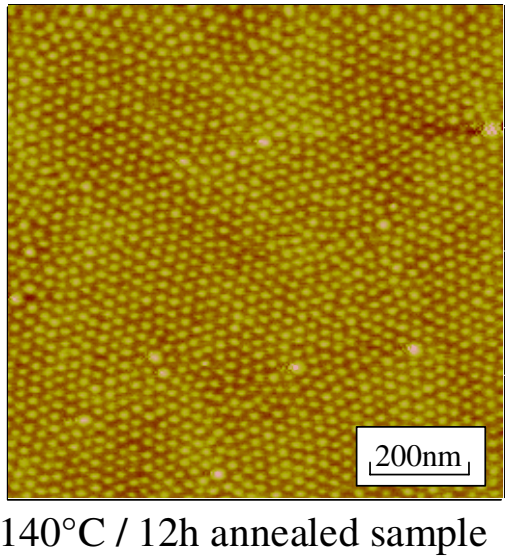

140°C / 12h annealed sample

Fig. 1 AFM tapping mode phase image.

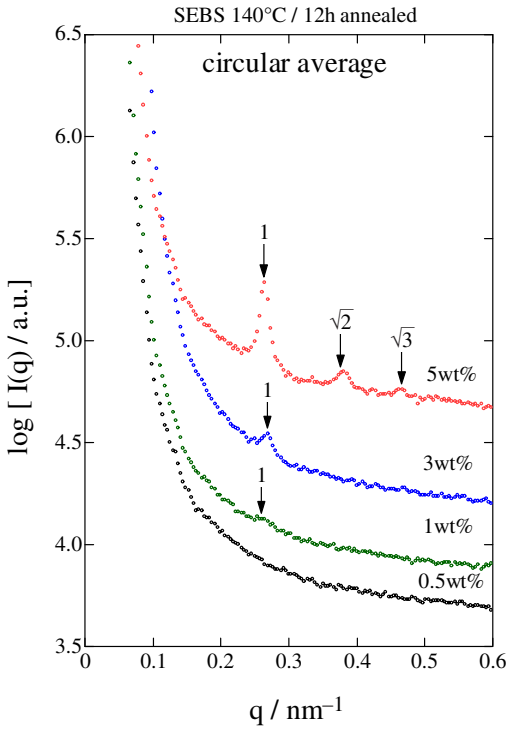

Fig. 2 SAXS profiles for thin films spin-cast on the cover glass.

7C/2001G273

Effective pair potentials of molten CuI estimated from the experimental partial structure factors

Pavlin D. MITEV[1], Masatoshi SAITO*[2], Kazumasa SUGIYAMA[3] and Yoshio WASEDA[1]
[1]IMRAM, Tohoku University, Sendai 980-8577, Japan
[2]Sch. of Health Sciences, Fac. of Medicine, Niigata Univ., Niigata 951-8518, Japan
[3]Dep. of Earth and Planetary Science, The University of Tokyo, Tokyo 113-0033, Japan

Introduction

A clear understanding of the physical properties of molten salts is known to depend upon their structure and pair potential at a microscopic level. It is also well recognized that the effective pair potentials estimated from the experimental structural data are quite useful, because they are considered to include, more or less, the particular features of liquid of interest. The main purpose of this work is to estimate the effective pair potentials of molten salt of CuI from the experimental partial structure factors[1] estimated from anomalous X-ray scattering (AXS) measurements by applying the modified hypernetted-chain equation.

Experimental

The AXS measurements for molten CuI were carried out with synchrotron radiation at BL-7C with incident energies of 8.6803, and 8.9553keV, which are 300eV and 25eV below Cu K absorption edges. Scattered intensities were collected using symmetrical transmission geometry with a devised silica glass cell.

Results and Discussion

The resultant effective pair potentials of molten CuI are shown in **Fig. 1** together with the model potentials. Calculated pair distribution functions from MC simulations using the potential presently obtained or model potential[2] are shown in **Fig. 2** together with experimental one. The following remarks could be given from these results. (a) The experimental pair distribution functions of Cu-Cu pair are well reproduced by MC simulation using the pair potentials presently obtained. The distribution functions indicate the characteristic like-ion penetration into the first unlike-ion coordination shell when compared with the model potential case. The present results of the Cu-Cu pair potential of molten CuI suggest more freely movement of Cu ions. (b) The present results of the Cu-I pair potentials show that there are negative deviations from the model potentials (Coulombic form) in the range from 0.4 to 0.9 nm. The deviation of the Cu-I pair potential from the Coulombic form is considered to be essential for the understanding of the density fluctuation of Cu ions by keeping the charge neutrality in Coulomb liquids. (c) The present results of the I-I pair potential are, in the authors' view, relatively close to the model potentials, this contrasts to the Cu-Cu and Cu-I cases. As a result, fairly good agreement is observed for the partial structure factors simulated using these two potentials.

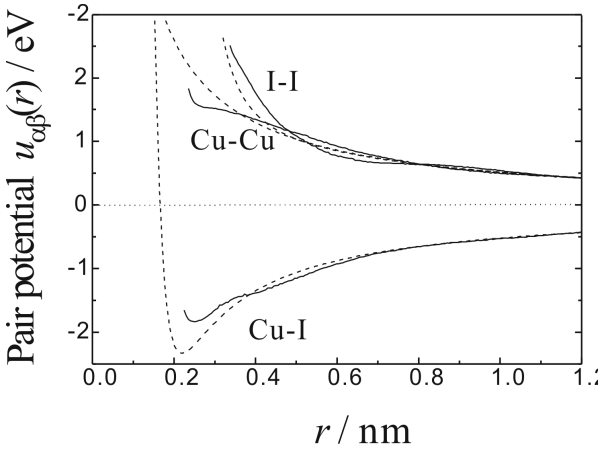

Fig. 1Effective pair potentials of molten CuI (solid line) estimated from the experimental partial structure factors in comparison with model potential (dotted line).

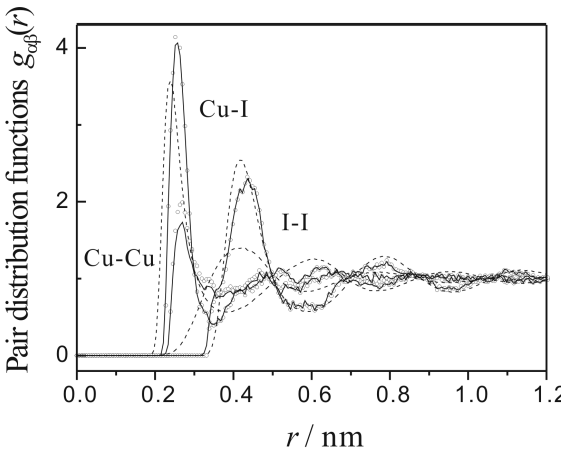

Fig. 2 Experimental PDF of molten CuI (open circles), in comparison with those of MC simulation with the effective pair potentials (solid line) and model potentials (dotted line).

References

[1] Y.Waseda et al, J.Phys.: Condens. Matter. **12**, A195 (2000).
[2] A.J. Stafford et al, J. Phys.:Condens. Matter **2**, 6631 (1990).

* masaito@clg.niigata-u.ac.jp

11B/2001G274

Local structure around Si atoms in GeSi alloy semiconductors

Ichiro YONENAGA*, Masaki SAKURAI
Institute for Materials Research, Tohoku University, Sendai 980-8577, Japan

Introduction

Germanium-silicon is a complete solid solution system, having the diamond cubic structure. The 4% difference in the lattice constants of constituent Ge and Si atoms leads various unique alloying phenomena on electronic, optical and mechanical properties. Knowing the accurate local structure is important and crucial in order to clarify the physical origin of such alloying phenomena, relevant to the local strain relaxation. We performed an XFAS study of the local structure of $Ge_{1-x}Si_x$ alloys grown by the Czochralski method in the whole composition range $0 < x < 1$ [1]. From Ge-K-edge spectra measured at 20K, the followings are reveled: GeSi alloy possess random substitutional site occupancy of Si and Ge atoms but no preferential ordering across the whole composition range. Ge-Ge and Ge-Si bond lengths maintain distinctly different lengths and vary linearly with alloy composition and to be close, but not completely, to the Pauling limit [2] rather than Vegard limit [3], similar to other semiconductor alloys as GaInAs [4]. The estimated topological rigidity parameter 0.6 suggests that the bond lengths and bond angles are distorted with alloy composition [5]. Thus, it is a task to clarify the local atomic structure and the compositional dependence of Si-Si bond length in GeSi alloys. Here we report preliminary results of XAFS investigations on the local structure around Si atoms in bulk crystalline GeSi alloys in the whole composition.

Experimental

High quality $Ge_{1-x}Si_x$ samples ($0<x<1$) were prepared from bulk alloy crystals grown by the Czochralski technique [6]. Si K-edge XAFS spectra of $Ge_{1-x}Si_x$ samples were measured using the total electron yield (TEY) detection at the soft X-ray XAFS station (BL-11B) of KEK-PF at room temperature. Channel cut InSb (111) was used for monochromator.

Results and Discussion

Figure 1 shows absolute values of Fourier transform $|F(r)|$ of Si K-edge $\kappa^3\chi(\kappa)$ of GeSi of various Si content x at room temperature. The intensity of the main peak around r = 2 – 2.2 Å, which is due to the nearest-neighbour atoms around Si atoms, decreases and the distance is shortened with an increase in Si content. Though detailed analysis of the above-shown results is now being conducted by FEFF6 program, the obtained XAFS signals at room temperature seem to be too poor to obtain quantitative information. Thus, we are conducting XAFS measurements at low temperature 20K.

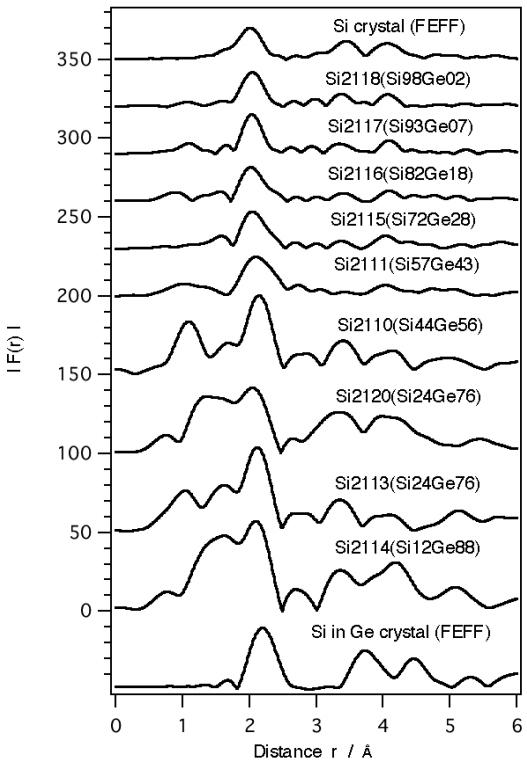

Fig. 1. The Absolute values of Fourier transform $|F(r)|$ of Si K-edge $\kappa^3\chi(\kappa)$ of GeSi of various composition x at room temperature.

In addition, it should be mentioned for future works that some absorption edges originating into unexpected impurities as S, P, Cl, etc. from the used beam-line were recorded on the XAFS spectrum.

References

[1] I. Yonenaga and M. Sakurai, Phys. Rev. B **64**, 113206 (2001).
[2] L. Pauling, *The Nature of the Chemical Bond* (Cornell University Press, NY, 1967).
[3] L. Vegard, Z. Phys. **5**, 17 (1921).
[4] J. C. Mikkelsen, Jr. and J. B. Boyce, Phys. Rev. Lett. **49**, 1412 (1982).
[5] N. Mousseau and M. F. Thorpe, Phys. Rev. B **46**, 16872 (1992).
[6] I. Yonenaga, J. Cryst. Growth **198/199**, 404 (1999).

* yonenaga@imr.edu

9C, 15A/2001G275

Time-resolved small- and wide-angle X-ray scattering studies on structure formation in crystalline graft copolymers

Katsuhiro YAMAMOTO*[1], Shigeru OKAMOTO[1], Kenji NAGATA[1], Shin-ichi SAKURAI[2], Shigeo HARA[1], Yusuke SUGINO[1] and Masashi MOURI[1]
[1]Nagoya Institute of Technology, Gokiso-cho, Showa-ku, Nagoya 466-8555, Japan
[2]Kyoto Institute of Technology, Matsugasaki, Sakyo-ku, Kyoto 606-8585, Japan

Introduction

Structure formation in block copolymers continues to be of considerable experimental and theoretical interest. In block copolymer containing a crystallizable component, structural changes resulting from crystallization will compete with those occurring due to microphase separation.

This report is concerned with the structure of polyethylene-poly(ethylene propylene) (PE-PEP) diblock copolymer quenched from lamellar microphase-separated phase below the polyethylene crystallization temperature. We present that time-resolved synchrotron SAXS and WAXS data for and DSC measurement was carried out simultaneously.

Experiment

The block copolymer used was synthesized by catalytic hydrogenation of polydiene precursor, which was anionically polymerized from butadiene and isoprene monomers. The number average molecular weight, M_n is 4.42×10^4, the M_w/M_n is 1.05, and weight fraction of polybutadiene (PB) is 0.52, where M_w denotes weight-average molecular weight. The simultaneous SAXS, WAXD and DSC (Mettler FP90) measurements were performed at BL9C and BL15A. The wavelength of X-rays was tuned at 0.1499 nm. The PE-PEP sample was heated up to 180°C at a rate of 2-20K/min and then cooled rapidly to crystallization temperature (T_c), where was slightly below melting temperature (T_m=108°C DSC peak top) of the hydrogenated PB block.

Results

Figure 1a shows time-resolved SAXS data detailing the crystallization of PE-PEP at 100°C. During this experiment, the sample was cooled at 100 at 20°C/min from 180°C down to 100°C. The intensities increase of the SAXS peaks beginning near 3 min is due to crystallization of PE block. The simultaneous growth of 4 peaks (q ratio of 1:2:3:4) indicates that crystallization results in the development of a lamellar morphology. Figure 1b also demonstrates the results of the simultaneous WAXS/SAXS/DSC measurements, which is corresponding to data in Figure 1a. DSC exothermic peak was observed during the crystallization. In the WAXS data, the increase intensities of (11) and (200) reflections of the orthorhombic PE crystal were observed. These crystalline reflections appear to develop on the almost same time scale as the increase in SAXS primary peak intensity during 100°C crystallization.

To analyze crystallization process, it is useful to replot the data in the Avrami form: $\ln(1-X_C)=-kt^n$, where, X_C is the fraction of crystallization that has occurred at elapsed time t, n is the Avrami exponent, and k is a constant. We obtain X_C from $X_C = (I(t)- I_0)/(I_m-I_0)$, where I_0 is the melt scattering intensity at T_C, I_m is the intensity at the end of the experiment, and $I(t)$ represents the intensity at time t.

Avrami plots for PE-PEP crystallized at 100 and 103°C are shown in Figure 2, based on the intensities of the primary SAXS peak. The Avrami exponents for PE-PEP were 1.7 and 3.0 at 100 and 103°C crystallization, respectively. These values were commonly observed for polymers that crystallize in spherulites.

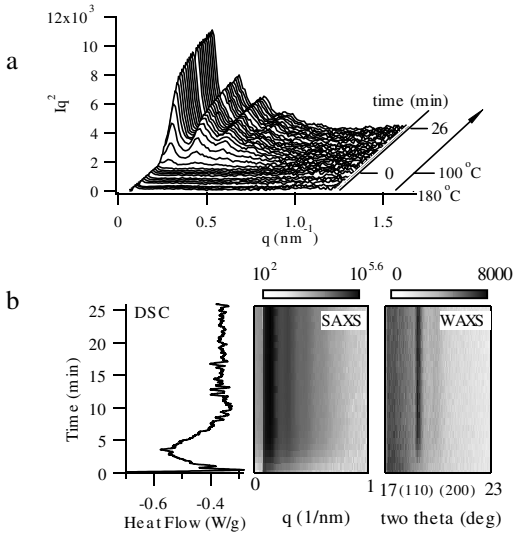

Figure 1. Time-resolved simultaneous WAXS/SAXS/DSC measurements during the crystallization at 100°C. Intensity graduations of SAXS and WAXS are in logarithmic and in linear scales, respectively.

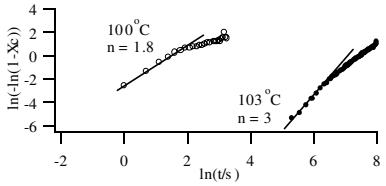

Figure 2. Avrami plots of the crystallization processes.

* katuhiro@mse.nitech.ac.jp

10C/2001G279

Structural development of sodium-form gellan gum gels on cooling

Yuji Jinbo*, Yusaku Sugiura, Hisanori Watanabe, Hideto Niwa, Katsumi Watanabe, and Yoshinobu Izumi
Graduate School of Science and Engineering, Yamagata University, Yonezawa, Yamagata 992-8510, Japan

Introduction

In the previous report, PF Activity Report, 18B, 139 (2000), we presented local lamellar structures of gellan gum gels in high concentration regions. In this study, we have investigated the structural change accompanied by the gelation process of gellan gum on cooling. A time-resolved SAXS measurement using the synchrotron radiation X-ray is the best tool for the observation of structural change with the time scale of second order.

Experimental

Two fractionated sodium-form gellan gum samples (NaGG), F-8-2 with M_v = 32000 and F-9 with M_v = 18000, were chosen for this study. Here, M_v represents the viscosity average molecular weight. The weight fraction of NaGG in the gel was adjusted to 0.06 for both gels in where the lamellar structure was formed at 25 ℃. A solution in the sol state was quenched manually by turning a valve connecting two water circular baths controlled at 90 °C and 23 °C in parallel. Time resolved SAXS measurements with a time slice of 5 sec and a frame number of 30 were performed on the SAXES apparatus in BL-10C station. Measurements were started at t = 15, 90, and 180 sec. Here, time t was counted when the temperature decreased after the quenching operation.

Results and Discussion

Figure 1 demonstrates the result of excess scattering intensity $I(q)$ for NaGG sample F-8-2 on cooling. Here q denotes the magnitude of scattering vector. In the sol state, $T > 33$ ℃, SAXS profiles almost overlap as drawn by two solid lines. It suggests that gellan gum chains are molecularly dispersing in the solvent, although the presence of a tiny amount of aggregate is observed as an enhanced low angle scattering intensity. When the temperature decreases below T_g = 32 ℃, $I(q)$ monotonically increases by time and further lamellar peaks begin to appear. We regarded T_g as the gel formation temperature and it was small *c.a.* 15 ℃ from the melting point of the gel. The thermal hysteresis of gellan gum gel can be explained by the structural difference between the transient gel with weakly ordered and enough matured gel with highly ordered. The peak position q_m for all $I(q)$ takes the same value of 0.081 Å^{-1} obtained for the gel ripen for 1 week which is shown by the bold solid line. It means that the lamellar structure with the same repeating distance is already formed even at the early stage of the gellan gum gelation process. The same behavior was also observed for the sample F-9.

To clarify the structural development of lamellar gels, the ratio of $I(q)$ for gels to that for sol at q_m, $A(t)$, was calculated. Intensities for gels were corrected taking the melting of gel due to the exposure of strong X-ray into account. In Figure 2, $A(t)$ for both gels are plotted against t. It is clearly seen that there are two stages in the gelation process of gellan gum. Values of $A(t)$ for both samples drastically increase in the early stage and then gradually approaches to some value in the next stage. It suggests that gellan gum chains in solution condense as aggregates or microgels that pile up further until it forms a macrogel. Consequently, the concentration fluctuation of gellan gum drastically enlarges in the early stage. In the second stage, the increment of concentration fluctuation stagnates and ordering to the lamellar structure progresses slowly. The results are fairly compared with the double exponential type equation with four adjustable parameters of A_i and k_i:

$$A(t) = 1 + A_1\exp[k_1(t-t_g)] + A_2\exp[k_2(t-t_g)] \qquad (1)$$

The second and the third terms correspond to the early and the second stage, respectively.

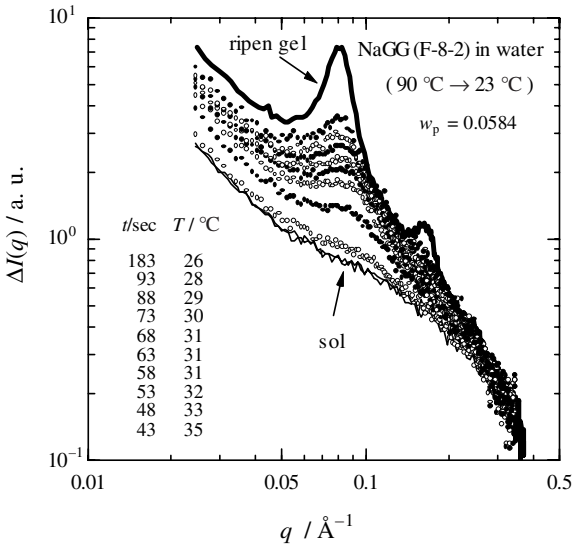

Figure 1. SAXS profiles for NaGG (F-8-2) on cooling.

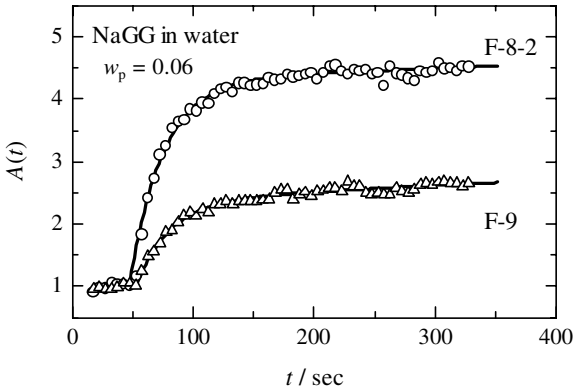

Figure 2. Lamellar peak intensity increment by the gelatin. Solid lines are calculated by Eq. (1).

* yjinbo@yz.yamagata-u.ac.jp

12C/2001G281

Local structure of Lu doped in high creep resistant Al_2O_3

Masaki SAKURAI*[1], Eiichiro MATSUBARA[1]
Hideo YOSHIDA[2], Yuichi IKUHARA[3] and Taketo SAKUMA[2]
[1]Institute for Materials Research, Tohoku University, Katahira, Sendai 980-8577, Japan
[3]Engineering Research Institute School of Engineering, The University of Tokyo, Hongo, Tokyo 113-8586, Japan
[2]Department of Advanced Material Science Graduate School of Frontier Sciences, The University of Tokyo, Hongo, Tokyo 113-8586, Japan.

Introduction

Addition of small amount of a third element into Al_2O_3 ceramic have been extensively studied to improve mechanical properties especially at high temperature. Recent years, Yoshida et al. have found that Lu doping is particularly effective in improving the high-temperature creep resistance of poly crystalline Al_2O_3[1]. TEM observation shows that doped Lu atoms condensed in the grain boundary of Al_2O_3[1]. Local environment around Lu atoms at grain boundary is directly connected to the mechanical properties of Lu-doped Al_2O_3. However, the role of the Lu has not been well understood. In this present work, we study the local structure around Lu atoms obtained by EXAFS.

Experimental

Mixture of high-purity Al_2O_3 and Lu acetate pressed into bars with cemented carbide under a pressure of 33MPa, and isostatically-pressed under a pressure of 100MPa. The pressed mixture was sintered at 1400°C for 2 hour in air. The amount of doped Lu was 0.05at%. Lu L_{III}-edge XAFS spectra were measured using fluorescence mode at the BL12C station with double Si(111) monochromator at 20K. In the curve fitting analysis, parameters of the phase shift, the back scattering amplitude and the electron mean free path were obtained using FEFF program.

Results and discussion

Fig. 1 shows (a) k^3Lu L_{III}-edge EXAFS, $k^3 \cdot \chi(k)$, of 0.05at%Lu-Al_2O_3 and Lu_2O_3 as reference sample and (b) Fourier transform of them. F(r) of Lu in Al_2O_3 exhibit only one peak at 1.9Å, which corresponds to the first nearest Lu-O pair, while Lu_2O_3 shows long distance correlations. Such vanishing of the long distance correlation of F(r) of Lu in Al_2O_3 suggests strong distortion of the local structure around Lu atoms. The results of the curve fitting analysis of the Lu-O correlation of Lu in Al_2O_3 are listed in a table 1. Since, one Gaussian fitting did not converge well in this curve fitting procedure, we use double Gaussian fitting for the Lu-O peak of Lu in Al_2O_3. Mean cation-oxygen distance in the octahedral site (coordination number is six) of the Lu_2O_3 is 2.24Å and that of the Al_2O_3 is 1.91Å. Consequently, it can be concluded that doped Lu in Al_2O_3 mainly occupy the octahedral site which similar to that in the Lu_2O_3. Larger mean coordination number of 6.5, however, suggests that Lu atoms also occupy the site with large volume. This heterogeneity of the local structure around Lu atoms causes large Debye-Waller factor. The local structure around Lu obtained from EXAFS reflects the condensation of Lu in the grain boundary of Al_2O_3.

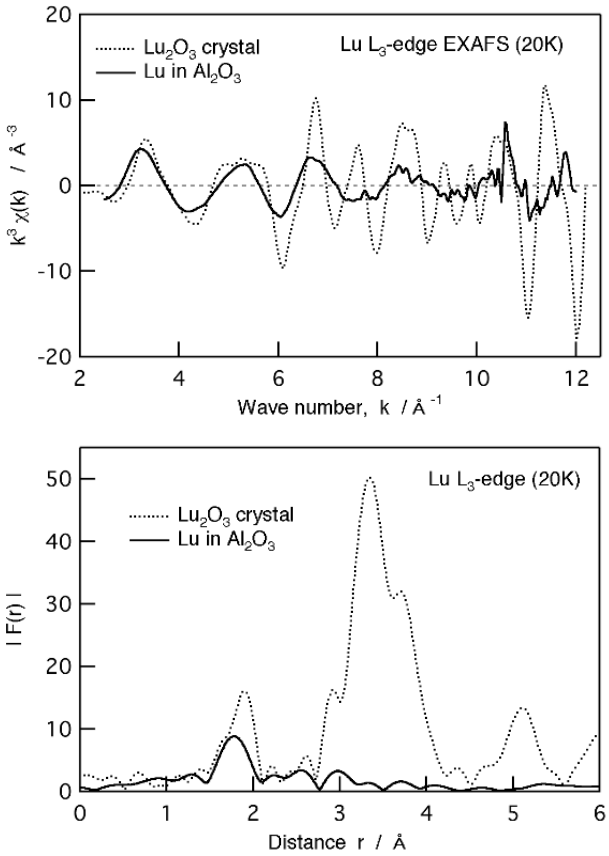

Fig.1 (a) k^3 Lu L_{III}-edge EXAFS, $k^3 \cdot \chi(k)$, of 0.05at%Lu-Al_2O_3 and Lu_2O_3 and (b) Fourier transform of them.

Table 1: Curve fitting results for Lu-O correlation of Lu L_{III}-edge EXAFS for Lu in Al_2O_3. N, R and σ correspond to coordination number, atomic distance and Dwbye-waller factor, respectively.

	N	R(Å)	σ(Å)
Lu_1-O	1.3	2.02	0.06
Lu_2-O	5.2	2.34	0.11

References

[1] H. Yoshida et al., Int. J. Inorg Mater. **1**, 229 (1999)

*msakurai@imr.edu

15A/2001G285

A grazing-incidence SAS measurement of Ge islands capped with Si

Hiroshi OKUDA*[1], Shojiro OCHIAI[1], Yoshiyuki AMEMIYA[2]
[1]IIC, Kyoto Univ., Yoshida Honmachi, Kyoto 606-8501, Japan
[2]Dept. of Advanced Mater. Sci., Tokyo Univ. Univ., Bunkyo-ku, Tokyo , Japan

Introduction

The structure of self-organized Ge islands capped with a Si layer has been examined by small-angle scattering measurements with grazing-incidence (GI-SAS).

Although the structure of semiconducting islands grown on substrates has been examined by direct methods such as scanning probe microscopy, GI-SAS has a merit that the structure of islands buried in a cap layer for protection or for confinement can be examined, in particular, as the macroscopic average. We conducted small-angle scattering experiments with grazing incidence with rather simple set-up. It was shown that the use of two-dimensional detector is quite useful and simple kinematical analysis applies when the islands are small enough and the scattering profile appears well above the critical angle.

Experimental

GI-SAXS experiment was performed at BL-15A with a sample rotation/height stage and the 9-inch II-CCD. A typical experimental setup is described in [1]. In order to set the angle of incidence slightly larger than the critical angle, trace of the specular reflection was used to calibrate the angle of sample stage. In the present measurements, a sample with one layer of Ge islands grown on Si substrate and capped with Si was examined.

Results and Discussion

Figure 1 shows a set of two-dimensional GI-SAXS patterns with the angle of incidence varying from just above the critical angle for Si to above that of Ge. It is seen that with the angle of incidence between the critical angle of Si and Ge (a), the SAS intensity is weak and no apparent SAS pattern originating from the island was observed. When the angle of incidence increased as shown in (b), well-defined SAS profile reflecting the shape of the island, and also the interference effect between islands was observed. The average size of the island was estimated to be about 9nm in radius from a Guinier approximation of the in-plane intensity. The Guinier radii was found to be the same when the direction of the incident beam with respect to the sample was rotated in the in-plane direction. This leads to a conclusion that the Ge islands examined in the present experiment is not facetted. From the peak distance in the in-plane component of the intensity, the average separation of the islands was found to be 44.2 nm. Since the distance between the neighboring islands are the same regardless of the crystallographic direction, the spatial distribution of the Ge island was isotropic in the present sample. Assuming a nearly close-packed distribution, the number density of the island was estimated to be 6.0×10^{-10} cm^2. It should be emphasized that the size and also the number density of the Ge island are evaluated without removing or destroying the capped layer in the present experiment. Present results suggest that GI-SAXS is quite useful in evaluating the structure of self-organized nanodots. Detailed analysis on the shape and distribution of the islands based on kinematical calculation is now under progress.

References

[1] H.Okuda PF Proceedings 2001-25,52(2002).

*okuda@mtl.kyoto-u.ac.jp

(a)

(b)

Fig.1 Two-dimensional GISAS profiles for α=0.3degree (a) and β=0.48 degree (b).

15A/2001G302

Conformation of humic acids from soils of different age studied by synchrotron X-ray scattering

Alexander Timchenko[1], Igor Serdyuk[1], Kazumoto Kimura[2], Hiroshi Kihara*[3], Rudolf Oberthur[4]
[1] Institute of Protein Research, Pushchino, Russia, 142292;
[2]Department of Biochemistry Dokkyo University School of Medicine, Mibu, Tochigi 321-02, Japan
[3] Dept of Physics,Kansai Medical University Uyamahigashi, Hirakata Osaka 573-1136, Japan
[4] Laboratory of Dr.Oberthur GmbH, Bruchweg 10, 49844 Bawinkel, Germany

Introduction

The Photon Factory Activity Report 2001 has adopted a new format for electronic publication of Users' Report. This document describes the requirements for submission of papers.

Humic acids (HA) are an important component of natural ecological systems and represent a polydisperse complex of natural biopolymers with molecular masses from several to hundreds kilodaltons. In our previous reports[1] we have shown the variability of conformations of HA of different origin. Thus, molecules in HA fractions of chernozem have preferentially a branched coiled conformation while those of compost have an elongated rod-like conformation. HA fractions from red soil had globular-like, blob-like and elongated conformations. Here we were interested in study of dependence of conformation and molecular mass distribution (MMD) on soil age. For this purpose we prepared humic substances from brown coal (10-60 million years), peat (10000 years), soil ESHA (500 years) with the new procedure including the treatment of organic material by 0.2 M ammonium hydroxide with the consequent air drying

Experimental

Synchrotron X-ray measurements were done on a small-angle camera B15-A (Photon Factory, Tsukuba) . HA samples were dissolved in 0.1M NaOH.

Results

To analyse scattering data we used Guinier and Kratky plots, distance distribution function P(R) and evaluated the fractal dimension from the logI-logh plot at higher scattering angles. Kratky plot, fractal dimension and P(R) indicate, at least, two phase distributions as seen from Fig.1. Conformation of such particles can be interpreted as blob-like structure more or less expanded. The values of Rg were from 8 nm to 11 nm. Strong dependence of Rg on the maximal distance of particle indicates the possible polydispersity of system. P(R) and extrapolated to zero scattering angle intensity I(0) show that for rather young sources of humic substances (soil ESHA, compost) the further extractions cause the enrichment of fraction with high molecular mass molecules. At the same time the extraction of HA from peat and brown coal does not change noticeably the MMD

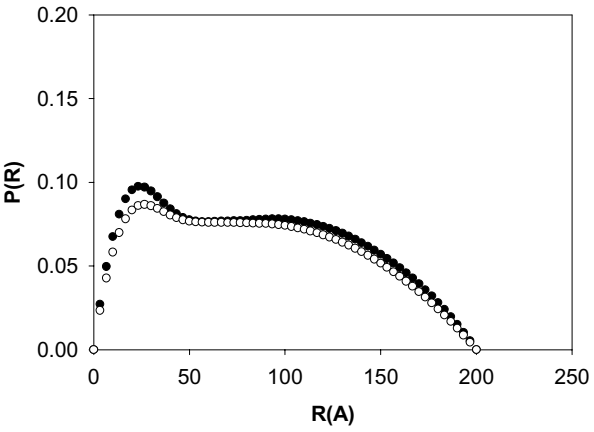

Fig.1 P(R) for two extractions of peat.

References

[1] A.A.Timchenko *et al*. **PPAR**(1998), 176;.(1999), 182. Proposal 97-G152, 99-G275.

*kihara@makino.kmu.ac.jp

10B/2001G321

EXAFS studies on the sprayed Pt catalyst prepared from PVP-stabilized colloid

Nobuyuki ICHIKUNI*, Yasuko TAKAGI, Shogo SHIMAZU and Takayoshi UEMATSU
Chiba University, Inage-ku, Chiba 263-8522, Japan

Introduction

Sprayed catalysts show the strong interaction between supported particles and the support. However, the aggregation of the particles easily occurred, and hence, the particle size was usually larger than 10 nm.

Particle sizes of platinum colloidal clusters are easily controlled between 0.8 to 4 nm by choosing reduction time, kind of stabilizer, the method of reduction and so on. Although colloidal clusters are very small, the stabilizer, such as polymers, covered the metal surfaces and lead to low metal surface area. Thus, the effective removal of the stabilizer from the colloidal clusters on the catalysts is one of the crucial problems.

In this study, we prepared Pt/Al_2O_3 catalyst from Pt-PVP (polyvinylpyrrolidone) colloidal clusters by spray reaction technique. Pt cluster size was characterized by EXAFS analysis.

Experimental

Pt-PVP colloidal cluster was prepared from $H_2PtCl_6 \cdot 6H_2O$ and PVP aqueous solution with molar ratio of 1:40. Ethanol (equivalent amount to H_2O) was added, followed by refluxed for 1 h at 356 K, resulting dark brown solution included Pt colloid [PVP-colloid]. Sprayed Pt/Al_2O_3 catalyst was prepared from the above Pt-colloidal solution and $Al(NO_3)_3 \cdot 9H_2O$ with the molar ratio of Pt:Al = 0.5:99.5. The ultrasonicated solution was aspirated through a quartz tube situated in the electric furnace at 1073 K under an ambient condition. The reacting droplets were dried, decomposed into oxides and subsequently calcined in the furnace within a second [PVP-spr1073]. Sprayed catalysts were calcined in the air at 673 K for 1 h to remove the residual stabilizer [PVP-spr1073c].

Pt L_3-edge EXAFS spectra were collected at BL-10B of the Photon Factory with Si(311) channel cut monochromator. Colloidal solution was concentrated and dried on the felt sheet. The powder samples were transferred into Al cells with Kapton windows. Curve-fitting analyses of k^3-weighted EXAFS oscillations in the k-space were performed by the EXAFS analysis program REX2000 (Rigaku Co.). Model parameters for curve-fitting analysis (back scattering amplitude and phase shift) were extracted from an EXAFS oscillation observed for bulk Pt (N =12, r =0.2774 nm).

Results and discussions

FT of the catalysts was shown in Fig. 1. The main peak of the colloidal solution and sprayed Pt/Al_2O_3 catalysts can be attributed Pt-Pt coordination in the Pt metal. Coordination number (CN) of Pt-Pt in PVP-colloid is 7.8 as shown in Table 1. So the particle size was estimated <2 nm. Although concentration process of colloidal solution might lead the some aggregation, severe aggregation had not occurred. CN of PVP-spr1073 and PVP-spr1073c are 8.1 and 8.6, respectively. They are almost same as that of PVP-colloid, suggesting the small Pt clusters can be prepared on the Al_2O_3 support by spray reaction technique. Moreover, additional calcination at 673 K did not lead the serious aggregation. It can be said that the strong interaction between Pt and Al_2O_3 support in the sprayed catalysts can prevent the aggregation during the treatment. The effectiveness of the spray reaction technique and colloidal solution to the catalyst preparation can be presented.

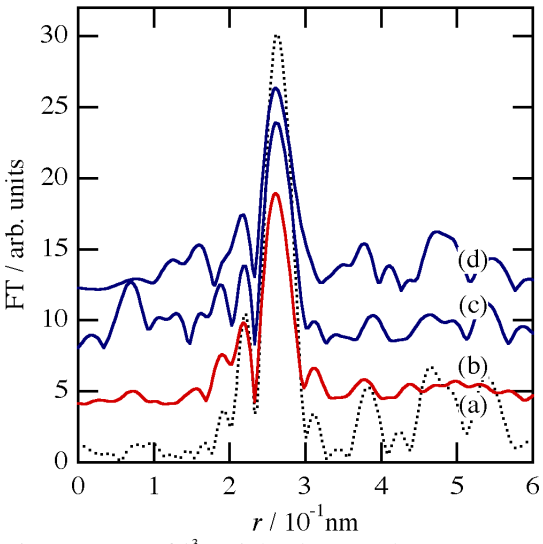

Figure 1. FT of k^3-weighted Pt L_3-edge EXAFS oscillation; (a) Pt foil, (b) PVP-colloid, (c) PVP-spr1073, (d) PVP-spr1073c.

Table 1: Curve fitting* results for Pt-Pt coordination

sample	N	r / nm	dE / eV	DW / nm
PVP-colloid	7.8	0.276	–0.885	0.0068
PVP-spr1073	8.1	0.276	–0.172	0.0066
PVP-spr1073c	8.6	0.276	–0.808	0.0071
bulk Pt	12	0.2774	0.0	0.006

*Fourier filtering range: 0.23-0.30 nm.

* ichikuni@tc.chiba-u.ac.jp

9A/2001G322

Effective pair potentials in $BaTiO_3$, $PbTiO_3$ and related perovskite-type compounds

Akira YOSHIASA*[1], Maki OKUBE[1], Hiroki OKUDERA[1], Masatomo YASHIMA[2], Roushown ALI[2], Kazumasa NAKAMURA[2], Atsushi SAKAI[2] and Mizuki MORI[2]

[1]Department of Earth and Space Science, Graduate School of Science, Osaka University, Toyanaka, Osaka 560-0043, Japan

[2] Department of Material Science and Engineering, Interdisciplinary Graduate School of Science and Engineering, Tokyo Institute of Technology, Nagatsuda, Midori-ku, Yokohama 226-8502, Japan

Introduction

The ideal perovskite-type structure is cubic symmetry such as $SrTiO_3$. Many perovskite type compounds have distorted variants with lower symmetry. Detailed knowledge of local structure and thermal properties for each atom in perovskite-type compounds is of great importance for understanding the mechanisms of favorable physical properties.

The analysis of temperature-dependent EXAFS Debye-Waller factor allows us to evaluate the anharmonicity of effective pair potentials and interatomic force constants for neighboring atoms [1,2]. We succeeded in the precise local structure analysis around Ca, Ti and Ge in $CaTiO_3$, $SrTiO_3$ and $CaGeO_3$ perovskite-type compounds [3]. Significant anharmonicity in thermal vibration for each bond was revealed in these compounds. On the other hand, Sicron et al. [4] reported that no anharmonicity for Ti-O bonds in perovskite-type $PbTiO_3$ ferroelectrics was detected in their EXAFS analysis.

In order to study if the anharmonic thermal vibration for each atom in $BaTiO_3$, $PbTiO_3$ and related perovskite-type compounds is dominant, we have determined the temperature variation of the local structure parameters up to 1200 K.

Experimental and analysis

The crystals of $BaTiO_3$, $PbTiO_3$, $SrTiO_3$ and $CaTiO_3$ perovskite were identified by X-ray diffraction. The measurements of Ca, Ti and Sr K-edge and Ba and Pb L3-edge EXAFS spectra were carried out in the transmission mode at beam line BL-9A of the Photon Factory. X-ray absorption measurements were made in the temperature range from 80 to 1200 K. Mirrors was used to eliminate higher harmonics. Details of the measurement and analysis were given in reference [1,3].

The EXAFS interference function was extracted from the measured absorption spectra and was normalized MacMaster coefficients according to the EXAFS workshop report. In quantitative analyses, we carried out the Fourier-filtering technique and a nonlinear least squares fitting method by comparing the observed and calculated EXAFS interference function. We used the EXAFS formula in the single scattering theory with the cumulant expansion up to the fourth order term.

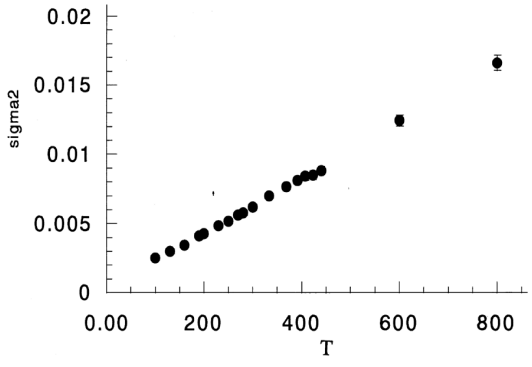

Fig. 1. Temperature (K) dependence of σ2 for the Ba-O bond in $BaTiO_3$

Results and Discussion

Figure 1 shows the temperature dependence of σ2 for Ba-O bond in $BaTiO_3$. The Debye-Waller type factor σ2 includes the effects of static and dynamic disorders. The static disorder is the configuration disorder, while the dynamic disorder arises from the thermal vibration of atoms. The contribution of the thermal vibration, $\sigma_{thermal}$, can be estimated under the assumption of classical statistical dynamics by the temperature dependence of σ 2 [1]. The gradient for the experimental σ 2 is equal to k_B/α, if we evaluate the anharmonic effective pair potential $V(u)=\alpha u^2/2+\beta u^3/3!$ from the contribution to the thermal vibration, where k_B is the Boltzmann constant, α and β are the potential coefficients and u is the deviation of the bond distance from the location of the potential minimum. β is calculated from the values of σ2 and σ3. The potential coefficient α for the Ca-O bonds in $CaTiO_3$ is 4.3 eV/Å^2. The potential coefficient α for the Ba-O bond in $BaTiO_3$ is 4.1 eV/Å^2. The magnitude of σ 2 of Ti-O bonds at higher temperature is greater than 0.01 Å^2. It was revealed that the Ti-O bonds in $PbTiO_3$ at higher temperature have significant anharmonic contributions.

References

[1] A.Yoshiasa et al., J. Synchrotron Rad. **6** 43(1999)
[2] A.Yoshiasa et al., (1997) Jpn. J. Appl. Phys **36** 781-784 (1997)
[3] A.Yoshiasa et al., J. Synchrotron Rad. **6** 1051 (1999)
[4] N.Sicron et al., Phys. Rev. **B50** 13168 (1994)

* yoshiasa@ess.sci.osaka-u.ac.jp

7C, 9A/2001G326

Ion beam irradiation effects of oxide thin films formed by oxygen cluster ion beam assisted deposition

Yutaka SHIMIZUGAWA[1,4,*], Jiro MATSUO[2,4], Toshio SEKI[2,4], Tatsuya ASANUMA[3], Kohei KADONO[3], Tomonari TAKEUCHI[3] and Hiroyuki Kageyama[3,4]
[1]Laboratory of Advanced Science and Technology for Industry, Himeji Institute of Technology, 3-1-2 Koto, Kamigori-gun, Ako, Hyogo 672-1025, Japan,
[2]Ion Beam Engineering Experimental Laboratory, Faculty of Engineering, Kyoto University, Sakyo, Kyoto 606-8501, JAPAN
[3]National Institute of Advanced Industrial Science and Technology (AIST), Kansai-Center, 1-8-31 Midorigaoka, Ikeda, Osaka 563-8577, Japan
[4]Collaborative Research Center for Cluster Ion Beam Process Technology

Introduction

The thin films metal oxides, for example TiO_2 will be used for multi-layer thin film for optical devices combined with SiO_2 thin films. It is necessary for the improvement of the optical properties to control accurately the refractive index and the optical transparency of the TiO_2 layer, i.e. high stoichiometry and so-called 'amorphous' structure.

The fluorescence XAFS analysis is one of powerful tools to analyses the valence state and the structure of the 'amorphous' thin films at the atomic level instead of the conventional X-ray diffraction technique. In this study we made the fluorescence XAFS measurement of Ti oxide thin films, which were obtained by the oxygen gas cluster ion beam assisted deposition techniques.

Experimental

The Ti K-XAFS of Ti oxide thin films with 200nm thickness, which were formed by both the oxygen gas cluster ion beam assisted deposition and an electron beam deposition, were measured in fluorescence XAFS mode by a Lytle type ionization chamber using incident X-ray beam monochromatized by double Si(111) crystals at beam line 7C and 9A. Also the Ti K-XAFS of Ti metal, two polymorphs of TiO_2, rutile and anatase, were measured as reference spectra.

Results and Discussion

Fig. 1 shows the comparison of the Ti K-XANES of the samples. The significant difference of the spectral features is observed between the films under electron beam and 3keV accelerated cluster ion beam deposition conditions, and two polymorphs of TiO_2.

Fig. 2 shows the comparison of the Ti K-EXAFS of the samples. Also the significant loss of long-range-order in high k region is found for both the films deposited with assistance of 3keV accelerated cluster ion beam and electron beam deposition. This suggests that these Ti oxide thin films have the amorphous-like structure.

New Energy and Industrial Technology Development Organization (NEDO) support this work.

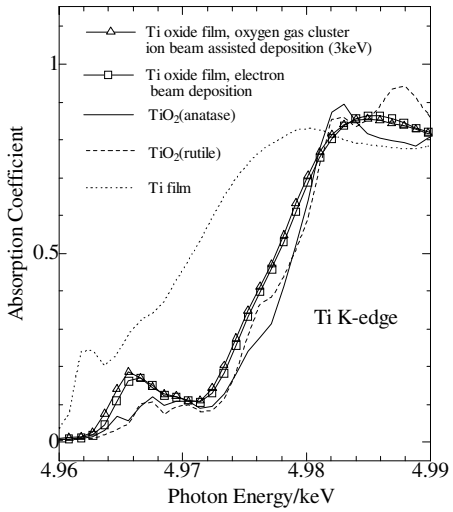

Fig. 1. Ti K-XANES of Ti oxide thin films, which were formed by the oxygen gas cluster ion beam assisted deposition (3keV) and electron beam deposition together with those of Ti metal, TiO_2 (rutile) and TiO_2 (anatase).

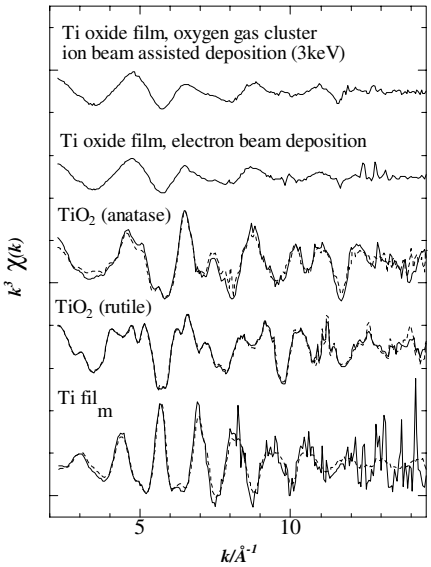

Fig. 2. Ti K-EXAFS of Ti oxide thin films, which were formed by the oxygen gas cluster ion beam assisted deposition (3keV) and electron beam deposition together with those of Ti metal, TiO_2 (rutile) and TiO_2 (anatase).

*shimizug@lasti.himeji-tech.ac.jp

7C,10B/2001G327

In situ XAFS study on molybdenum oxide catalysts supported on zirconia by molten salt preparation

Nobuyuki MATSUBAYASHI*[1], Motoyasu IMAMURA[1], Koichi SATO[1], Tomoaki TANAKA[1], Kyoko K. BANDO[1], Hiromichi SHIMADA[1] Pavel AFANASIEV[2] and Christophe GEANTET[2]
[1]*National Institute of Advanced Industrial Science and Technology, Tsukuba, Ibaraki 305-8565, Japan*
[2]*Institut de Recherches sur la Catalyse, 2 avenue Albert Einstein, 69626 Villeurbanne cedex, France*

Introduction

Catalyst preparation by the molten salt method has been shown to produce novel catalysts with high surface areas. In the preparation of molybdenum catalysts, the structures and the reaction mechanisms of the intermediates were not yet clarified. Because these intermediates do not have long-range ordered structures, we applied XAFS to the structural analyses involving composition determination of molybdate species in mixed KNO_3 and $NaNO_3$ salt [1]. In the previous study, we have clarified the changes in the composition of molybdate species during the catalyst preparation procedures [2].

In the present report, the reaction behavior of the preparation of unsupported molybdate catalysts in molten nitrate was investigated by *in situ* EXAFS. For this purpose, XAFS measurements were done using an *in situ* cell at various temperatures between 298 and 773 K.

Experimental

Unsupported molybdate catalysts were prepared from a MoO_3 precursor (5mg) with 150mg of $NaNO_3$ in a quartz reactor. The amount of molten nitrate corresponds to a 10-20 fold molar excess. The mixture was heated up to 773K being kept for 1h stepwise by 50 K during a XAFS measurement as Fig.1. The Mo K-edge XAFS measurements were performed at the Photon Factory (BL10B) using a Si(311) channel-cut crystal monochromator. Fourier transformation was performed for Δk=80 nm^{-1} of Mo K-edge EXAFS. The phase shift and backscattering amplitude factor were corrected by using the calculated values of FEFF8 for Mo as an absorber and O as a scatter in crystalline Na_2MoO_4 .$2H_2O$.

Results and discussion

Figure 1 shows XANES spectra. of Mo K-edge of MoO_3/$NaNO_3$ at 298 – 773 K plotted vs. time. A disorder of the spectra was found at melting point. The edge shape was changed from that of MoO_3 to that of MoO_4^{2-} at the melting point indicating the change of dominant species.

Figure 2 shows the Fourier transforms of Mo K-edge EXAFS of MoO_3/$NaNO_3$ measured at 298-773K. The peak at 0.36 nm is assigned to Mo-Mo scattering of the MoO_3 structure. This indicates that the local structure of MoO_3 precursor remains intact before melting. With increasing temperature, the intensities of the peaks at 0.36 nm decrease, whereas the intensities of the peaks at 0.18 nm corresponding to Mo-O scattering in the highly symmetrical tetragonal MoO_4^{2-} structure increase. These

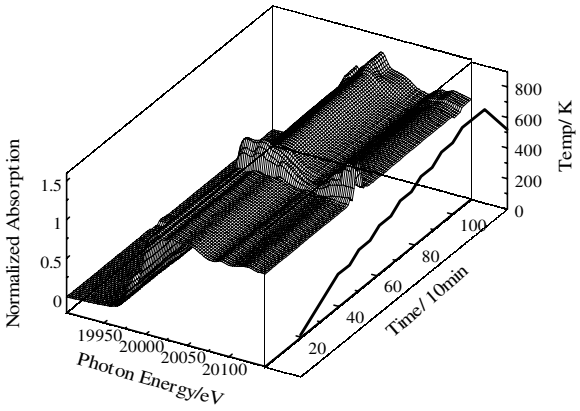

Fig.1 *in situ* XANES spectra. of Mo K-edge of MoO_3/$NaNO_3$ at 298 – 773 K.

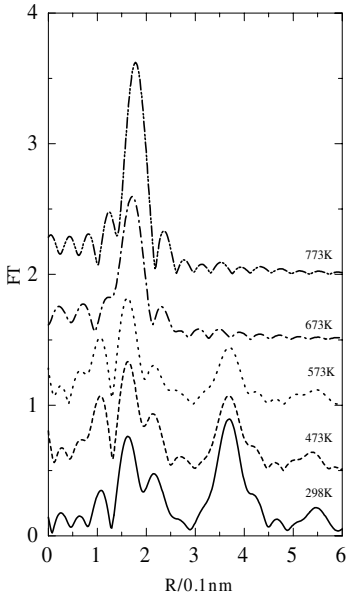

Fig.2 Fourier transforms of Mo K-edge EXAFS of MoO_3/$NaNO_3$ measured at 298-773K.

results show that the MoO_3 precursor transforms into MoO_4^{2-} with increasing temperature.

References

[1] N. Matsubayashi *et al.*, J. Phys IV France, **7(2)**, 1179 (1997).
[2] N. Matsubayashi *et al.*, *Journal of Synchrotron Radiation*, **8**, 610 (2001).
* n-matsubayashi@aist.go.jp

10C/2001P014

Structure of bicelle formed by mixed surfactants

Kenji Kubota*[1], Kousirou Taya[1], Rio Kita[2], Kenji Ochiai[1] and Kaori Wakamatsu[1]
[1]Faculty of Engineering, Gunma Unive., Kiryu, Gunma 376-8515, Japan
[2] Supramolecular Science Laboratory, RIKEN (The Institute of Physical and Chemical Research), Wako, Saitama 351-0198, Japan

Introduction

Bilayered mixed micelle, known as bicelle, is a molecular assembly in which the long-chain phospholipid-rich disc-shaped bilayered structure is stabilized by the regular alignments of surfactant (short chain phospholipid or detergent) on the periphery of the disc. Therefore, bicelle is a suitable model membrane system and is useful for the physicochemical and biochemical studies of membrane proteins. CHAPSO is a twitterionic detergent having the steroid group similar to bile salts, and its solubility is fairly high with CMC being ca.8mM. Though it has generally been expected that the mixture of DMPC and CHAPSO forms bicelles, the structure of phospholipid-CHAPSO mixture has not been studied in detail. The detailed structure of bicelles containing CHAPSO was determined by SAXS measurements combined with model calculations of scattering functions taking into account the spatial variation of electron densities.

Experimental

L-α-Dimyristoylphosphatidylcholine (DMPC) used for the preparation of the mixed micellar solutions were purchased from Avanti Polar Lipids Inc. (Alabaster, AL) and was used without further purifications. Detergent, (cholamidopropyl) dimethylammonio-2-hydroxy-1-propanesulfonate (CHAPSO) was obtained from DOJINDO (Kumamoto, Japan), and was of 96 % purity. The respectively dispersed solutions of DMPC and CHAPSO were mixed to make the final solutions for the measurements by employing ultrasonication. Dynamic light scattering measurements were also carried out using a homemade spectrometer and an ALV-5000 multiple-tau digital correlator to obtain the correlation functions of scattered light $g^{(2)}(t)$. Vertically polarized Ar ion laser operated at the wavelength of 488.0 nm was used as the incident beam. Hydrodynamic radius was calculated by using the Einstein-Stokes equation. Small angle X-ray scattering measurements were performed by BL-10C station of KEK-PF (λ_0 = 0.149 nm). All the measurements were carried out at 30°C [1].

Results and Discussion

Typical result of the scattering function (q = 1.0, 50 mM, and at 30°C) is shown in Fig. 1. Here, the solid curve is calculated for a model structure of DMPC/CHAPSO bicelle by introducing the spatial variation of electron densities (details are described below). By the method of Guinier plot, radius of gyration R_g was determined at the small scattering vector region. The obtained R_g was 3.39 nm for Fig. 1. In the present case, it was necessary to simulate the scattering function based on the model structure of the assemblies to determine the detailed three-dimensional structure. Scattering functions were calculated for several model structures, such as a bicelle (bilayered disc) with three or five layers of electron density variation along the disc normal and periphery (rim), rotational ellipsoid, sphere (micelle or vesicle), rod (or cylinder), and so on. The solid curve in Fig. 1 is obtained for the model of the bicelle structure with five layers of electron densities. The fitting is quite good with this model, and calculations with other model failed to give such an agreeable result. The resultant thickness of the bicelle composed of DMPC and CHAPSO is ca. 4.4 nm in good agreement with the reported values for the lamellar thickness. Such a spatial profile suggests that the bilayered assembly of DMPC is edge-stabilized by two CHAPSO molecules aligned in the direction of the disc normal, and that CHAPSO molecules are located also in the bilayered surfaces with the sterol pseudoplane oriented parallel to the surface. The three OH groups of sterol ring which are located on one face of the pseudoplane are considered to direct toward the outside of the bicelle with the other (hydrophobic) face oriented toward the hydrophobic interior. That is, the mixture of DMPC and CHAPSO forms the commonly expected bicelle structure at q = 1.0. This model picture is similar to that of phospholipid/bile salt mixture, although the packing state of CHAPSO molecules in the present bicelles differs from those proposed so far.

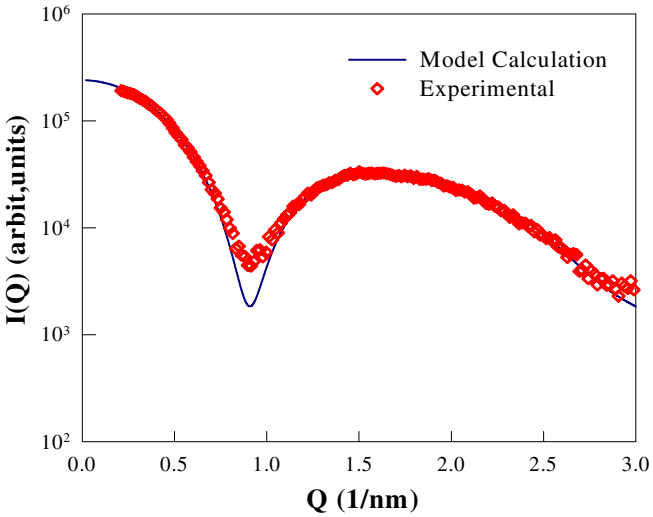

Fig. 1 Scattering profile (q = 1.0, 50 mM at 30°C).

References

[1] K.Taya, K. Kubota, K. Ochiai and K. Wakamatsu, Trans. M. R. S. Japan, in press (2002).

* kkubota@bce.gunma-u.ac.jp

4C,16A2/2001S2-002

Resonant x-ray scattering study on the filled skutterudite $PrFe_4P_{12}$

K. ISHII[*1], T. INAMI[1], Y. MURAKAMI[1,4], L. HAO[2], K. IWASA[2], M. KOHGI [2], Y. AOKI[2], H. SUGAWARA[2], H. SATO[2], S. IMADA[3], H. NAKAO[4], Y. WAKABAYASHI[5] H. SAWA[5]

[1]Synchrotron Radiation Research Center, JAERI, Mikazuki-cho, Hyogo 679-5148, JAPAN
[2]Department of Physics, Tokyo Metropolitan University, Hachioji, Tokyo 192-0397, JAPAN
[3]Department of Material Physics, Osaka University, Osaka 650-8531, JAPAN
[4]Department of Physics, Tohoku University, Sendai 980-8578, JAPAN
[5]Photon Factory, Institute of Materials Structure Science, Tsukuba 305-0801, JAPAN

Introduction

The filled skutterudites RT_4X_{12} (R = rare earth, T = Fe, Ru, and Os, X = P, As, and Sb), which crystallize in a *bcc* structure, exhibit a wide variety of electronic properties, such as superconductivity, magnetic order, and metal-insulator transition. Among them, the interest in $PrFe_4P_{12}$ is an anomalous ordered state at low temperature. The phase transition at T_A = 6.5 K is confirmed by the specific heat measurement [1], but no magnetic reflection was observed in neutron powder diffraction [2]. On the other hand, lattice distortion which is characterized by the modulation wave vector of $\mathbf{q} = [1, 0, 0]$ was observed below T_A in recent X-ray diffraction study [3], and magnetic field induced antiferromagnetic moment with the same characteristic wave vector **q** as above was also observed at the temperatures below T_A by neutron diffraction experiment [4]. These facts strongly suggest that the phase transition at T_A is accompanied by an antiferroquadrupolar ordering. This ordered state is suppressed by magnetic field, and a heavy-fermion-like behavior appears, which is evidenced by large electronic specific heat coefficient and large cyclotron effective mass. Here we report the resonant x-ray scattering (RXS) experiments at the Pr-L_{III} absorption edge to investigate the ordered state of $PrFe_4P_{12}$. RXS is a combined technique of diffraction and spectroscopy, and can elucidate a spatially ordered electronic states, such as charge, magnetic, and orbital order.

Experimental

Single crystals of $PrFe_4P_{12}$ were grown by a tin-flux method. X-ray scattering experiments were carried out at beamline 4C and 16A2 at Photon Factory, KEK. We measured three reflections, (300), (111), and (210) which are forbidden in the *bcc* structure above T_A and become allowed below T_A due to the lattice distortion.

Results and Discussion

Figure 1 shows fluorescence and scattering intensity of (111) reflection near the Pr-L_{III} absorption edge. Two resonant features were observed around 5.965 eV and 6.000 eV. We also observed the resonance in (300) and (210) reflections. The scattering amplitude of the superlattice reflections at the absorption edge of Pr consists of two components, the lattice distortion and the resonant scattering of Pr. If both components are finite, interference term appears in the intensity. The assumption that Pr atoms do not change the position at the phase transition is reasonable in the structural model proposed experimentally [3] and theoretically [5]. Based on this assumption, resonant scattering term for the odd number of $h + k + l$ corresponds to the difference of anomalous scattering factor between two Pr atoms in the *bcc* unit cell. Anomalous scattering factor is closely related to the electronic states of resonating atom. Therefore our result suggests a spatial ordering of two different electronic states of Pr atom, which is probably an antiferroquadrupolar ordering, appears below T_A.

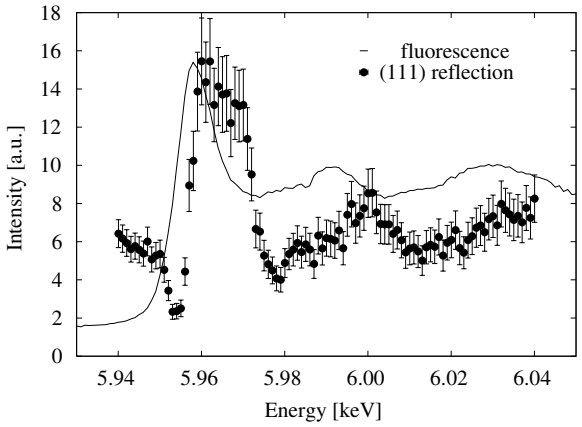

Figure 1: Energy dependence of fluorescence yield and (111) reflection

References

[1] T. D. Matsuda *et al*., Physica B **281-282**, 220 (2000).
[2] L. Keller *et al*., J. Alloys Compd. **323-324**, 516 (2001).
[3] K. Iwasa *et al*., Physica B **312-313**, 834 (2002).
[4] L. Hao *et al*., to be published .
[5] S. H. Curnoe *et al*., Physica B **312-313**, 837 (2002).

*kenji@spring8.or.jp

4C, 16A2/2001S2-002

Resonant X-ray studies of orbital ordering systems

Youichi Murakami*[1,2], Hironori Nakao[1],Takeshi Matsumura[1], Kazuma Hirota[1]
Yusuke Wakabayashi[3], Hiroshi Sawa[3], Hiroyuki Ohsumi[4], Masato, Kubota[5], Takahisa Arima[5,6]
Makoto Izumi[7], Yasujiro Taguchi[3], Yoshinori Tokura[5,7], Fumitoshi Iga[8]
[1]Department of Physics, Tohoku University, Sendai 980-8578, Japan
[2]Synchrotron Radiation Research Center, JAERI, Sayo, 679-5148, Japan
[3]KEK-PF, Tsukuba, Ibaraki 305-0801, Japan
[4]Japan Synchrotron Radiation Research Institute, Sayo 679-5198, Japan
[5]ERATO, Tsukuba 305-8562, Japan
[6]Institute of Materials Science, University of Tsukuba, Tsukuba 305-8573, Japan
[7]University of Tokyo, Tokyo 113-8656, Japan
Department of Quantum Matter, ADSM, Hiroshima University, Higasihiroshima 739-8526, Japan

Introduction

We have developed a technique to detect the orbital ordering, that is, the resonant x-ray scattering. This technique is a combined technique of diffraction and spectroscopy. We have not only studied the microscopic mechanism of the scattering but also applied this technique to interesting systems and achieved new results. This year we have searched a new direction of "Orbital Physics" and accomplished some discoveries.

Experimental Results

Charge and Orbital Ordering of $La_{2-2x}Sr_{1+2x}Mn_2O_7$

In the recent study of manganites, the microscopic phase separation has been reported and discussed in connection with the huge magnetoresistance. Recently it has also been observed by the neutron scattering that two phases with different spin states, CE- and A-type antiferromagnetic phases, coexist in highly-doped region of bi-layered manganites $La_{2-2x}Sr_{1+2x}Mn_2O_7$ (x = 0.5 – 0.6). In order to study this phase separation and the charge-orbital ordering of the CE-type phase we have carried out the resonant x-ray scattering using synchrotron radiation. The resonant peaks have been detected at the superlattice spots in the sample with x = 0.5, 0.525, 0.55, 0.575 and 0.6. The resonant scattering intensities systematically decrease with increasing x. However, the correlation lengths remain longer than 2000 Å in all samples. It is noted that the superlattice positions (1+Δ, 1+Δ, 0) for the orbital ordering show lock-in behaviour and are shifted from Δ= 0.25 to 0.22 with increasing x. The phase separation and the microscopic model of the charge and orbital ordering will be discussed from these results.

Charge and Orbital Ordering in $Nd_{1-x}Sr_{1+x}MnO_4$

The charge and orbital ordering of a layered perovskite $La_{1-x}Sr_{1+x}MnO_4$ has been studied as the typical sample of these orderings. However, the sample with x > 0.5 has seldom been investigated owing to the chemical phase separation. Recently, by substituting Nd for La, the single crystals $Nd_{1-x}Sr_{1+x}MnO_4$ (0.5 < x < 1) could be grown. We have studied the ordering state of the sample with x = 0.67 and 0.75 using the resonant x-ray scattering. The superlattice spots with modulation wave vector q = (Δ, Δ, 0), Δ = 1/8, 1/4 (1/6, 1/3) have been observed in the samples with x=0.75 (0.67). These results show that the charge and orbital structure has the unite cell of $4\sqrt{2}a \times \sqrt{2}a \times c$ ($3\sqrt{2}a \times \sqrt{2}a \times c$).

Quadrupolar Ordering in RB_2C_2 (R = Dy, Ho)

We have performed the resonant x-ray scattering experiment of DyB_2C_2 and HoB_2C_2, where the antiferroquadrupolar ordering play important roles. The superlattice reflections that appear below the transition temperatures have been investigated by measuring the incident energy , polarization, scattering vector, azimuthal angle and temperature dependences at the L3 absorption edge of Dy and Ho. The results are theoretically analyzed with a model of the antiferroquadrupolar order: the azimuthal angle dependences are well explained. The quadrupolar and magnetic contributions to the scattering intensities are also separated: it is deduced that the magnitude of the ordered quadrupolarmoments of HoB_2C_2 is much smaller than that of DyB_2C_2.

Microscopic mechanism of the resonant x-ray scattering

The microscopic mechanism of the resonant x-ray scattering still remains controversial in the t_{2g} perovskite systems. We have tried to elucidate the mechanism by systematic study in $Y_{1-x}Ca_xTiO_3$. It has been found that the signal observed includes the small signal from the tilting and distortion of the TiO-octahedrons at the absorption main edge of Ti, while the pre-edge signal is purely ascribed to the orbital ordering.

* murakami@iiyo.phys.tohoku.ac.jp

17A, 17C/2001Y003

Stress measurement of tetragonal $Pb(Zr_{1-x}Ti_x)O_3$ thin films grown on Pt electrode

Kenji NOMURA and Naoki AWAJI

Fujitsu Laboratories Ltd., 10-1 Morinosato-Wakamiya, Atsugi 243-0197 Japan.

Introduction

Owing to the many potential in applications in nonvolatile memory devices, ferroelectric thin films of $Pb(Zr_{1-x}Ti_x)O_3$ (PZT) have been studied intensively in recent years. The presence of stress in the ferroelectric thin films can be expected to influence the electrical properties of an integrated ferroelectric capacitor.

In this study, we examined the stress in PZT and Pt films for the PZT/Pt/Ti structure by X-ray diffraction.

Experimental and Results

The X-ray diffraction was carried out at BL-17A with the wave length of λ =1.1 Å. In this study, we used a PZT film produced using a conventional sol-gel technique on Pt/Ti bottom electrode. The PZT and Pt films have (111) and randomly oriented crystals. The X-ray profiles measured at χ from 0° to 86° around tetragonal PZT(111) and Pt(111) peaks are shown in Fig. 1. In order to measure the stress in the PZT thin film with accuracy, the PZT(111) peak was used because the PZT(111) peak do not split in the tetragonal phase. The stress (σ) in the film can be calculated from the equation (1).

$$\sigma = -\frac{E}{2(1+\nu)} \cdot \frac{1}{\tan\theta_0} \cdot \frac{\pi}{180} \cdot \frac{\Delta(2\theta)}{\Delta(\sin^2\chi)} \qquad (1)$$

E, ν and $2\theta_0$ are the Young's modulus, the Poisson ratio and the Bragg angle without stress the of the film material, respectively. The values of E, ν and $2\theta_0$ in the PZT and Pt films are shown in Table. 1. Each peak in Fig. 1 was fitted using Gauss function to obtain the peak position, and the peak positions ($2\theta_{PZT(111)}$ and $2\theta_{Pt(111)}$) of PZT(111) and Pt(111) were plotted as a function of $\sin^2\chi$ as shown in Fig. 2. In the figure, the solid line shows the result of fitting using the equation $2\theta = A \sin^2\chi + B$, where A is $\Delta(2\theta) / \Delta(\sin^2\chi)$ in equation (1). Both the PZT film and the Pt film were under two-dimensional tensile stress. The stresses in PZT and Pt films calculated from the equation (1) were 345 and 46 (MPa), respectively.

In the future, the process dependence of the stress in the PZT films will be measured in order to clear the correlation between the stress and the electrical property.

Table. 1 The values of E, ν and $2\theta_0$ in PZT and Pt films.

	E(MPa)	ν	$2\theta_0$(°)
PZT	34000	0.350	27.211
Pt	168000	0.377	28.107

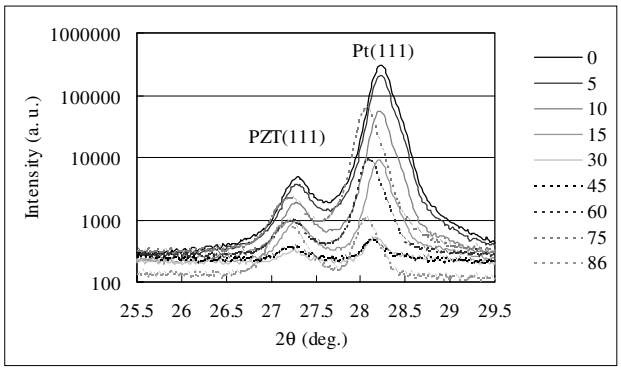

Fig. 1. The X-ray profiles measured at χ from 0° to 86° around PZT(111) and Pt(111) peaks.

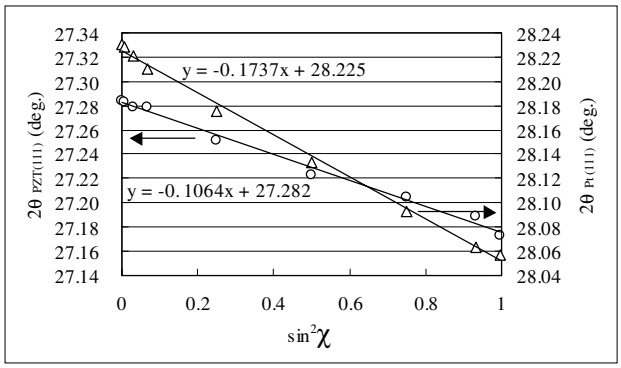

Fig. 2. The peak positions of PZT(111) and Pt(111) measured at χ from 0° to 86°.

E-mail: knomura@flab.fujitsu.co.jp

15B/2001C001

Anisotropy of substructure in secondary recrystallized grain in 3%Si-Fe

Yoshiyuki Ushigami*[1], Shuich Nakamura1[1],Noriaki Ota[2] and Masao Kimura[3]
[1]Steel Research Laboratories , Nippon Steel Corporation, 20-1 Shintomi, Futtsu, Chiba 293-8511
[2]Nippon Steel Technoresearch Corporation,20-1 Shintomi, Futtsu, Chiba 293-0011
[3]Advanced Technology Research Laboratories, Nippon Steel Corporation, 20-1 Shintomi, Futtsu, Chiba 293-8511

Introduction

It is reported that most of single crystals contain substructures, which depend on their production methods. Dynamic observation has revealed that subboundaries develop in the secondary recrystallized grains during grain growth stage [1-2]. Subboundaries are terminated at the growth front of the secondary recrystallized grain and develop successively along the grain growth direction absorbing dislocations, which generate by grain growth (Fig.1). TEM analysis has shown that these subboundaries consist of edge dislocations. Thus, it is deduced that these subboundaries should have orientation dependence and might have anisotropic distribution.

Experimental procedure

To analyze the distribution of the subboundaries, white x-ray topographs were taken with the reflected Berg-Barrett method. Synchrotron x-ray beam was incident to the sample at a glancing angle and asymmetrically diffracted beams were recorded by x-ray film to observe the wide range of the specimen (40×60 mm).

Results and discussions

Fig.2 shows the whole range of {110}<001> secondary grain. Subboundaries develop radially from the central nucleation site. It can be seen that the distribution of these subboundaries is anisotropic; subboundarties develop densely in the transverse <110> direction in comparison with the <001>direction.

It is well known that the Burger's vector of 3%Si-Fe crystal is <111> and that the slip planes are {110} and {211}. Thus, the subboundaries, which consist of edge dislocations, are expected to grow in the dislocation lines of <211> and <110>. It is also requested that the dislocation lines should be in the low angel region in the sheet for the continuity of subboundaries. Fig.3 shows the distribution of these dislocation lines which lie within 20 degrees to the sheet plane of the {110}<001> grain. It is clear that the distribution of dislocation lines is dense in the transverse direction and this corresponds to that of subboundaries. It has been clarified that the substructure is anisotropic and this anisotropy can be explained by the above dislocation model.

References

[1]Y.Ushigami, Y.Suga, N.Takahashi, K.Kawasaki, Y.Chikaura and H.Kii, J. Mater. Eng. **13**, 113 (1991)
[2]Y. Ushigami, K. Kawasaki, K. Murakami, Y. Okazaki, T. Kubota and Y. Chikaura: Proc. 11th Intern. Conf. on Textures of Materials, 560, (1996)
*ushigami@yawata.nsc.co.jp

Figure 1 Schematic diagram of the mechanism of subboundary formation during grain growth.

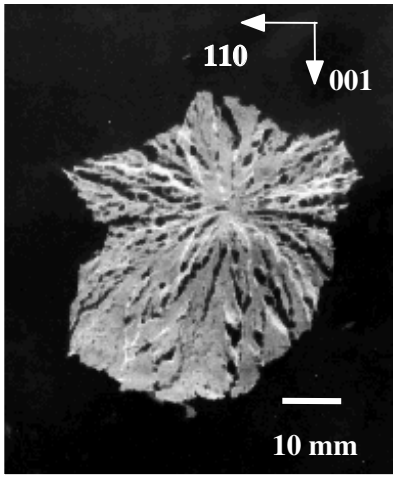

Figure 2 X-ray topograph of {110}<001> secondary recrystallized grain.

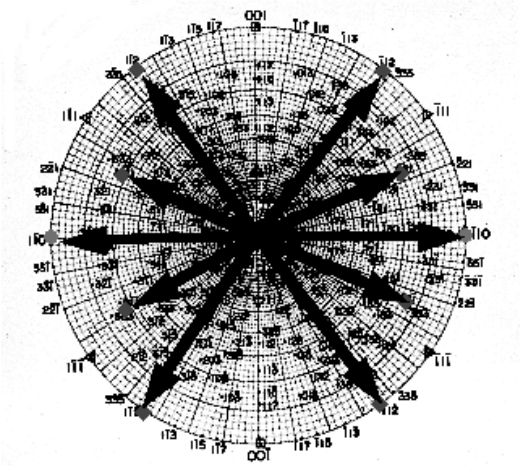

Figure 3 Distribution of <110> and <211> dislocation lines in {110}<001> secondary grain.

12C/2001C001

$Fe(O,OH)_6$ network nanostructure of rusts formed on weathering steel

Masao KIMURA*[1], Tamaki SUZUKI[1], Hiroshi KIHIRA[2]
[1] Adv. Tech. Res. Lab., Nippon Steel Corp., Futtsu, Chiba, 293-8511, Japan
[2] Steel Res. Lab., Nippon Steel Corp., Futtsu, Chiba, 293-8511, Japan

Introduction

Improvement of the corrosion resistance of steel without coating is very important from the viewpoint of life-cycle assessments of materials. Surprisingly "weathering steel" containing a 0.3-0.7 mass% Cr and Cu, forms a protective rust layer after a few years of corrosion under atmosphere and shows a good corrosion resistance.

In order to make clear the corrosion resistance mechanism, the atomic level structure of rust is of great interest. The rust mainly consists of FeOOH, typically α-FeOOH and γ-FeOOH. Their structures are composed of FeO_6 octahedrons and intercalated hydrogen (Fig.1). In this study, the change of nanostructures of rusts during corrosion was investigated using x-ray absorption fine structure (XAFS) with a special attention to effects of additional elements.

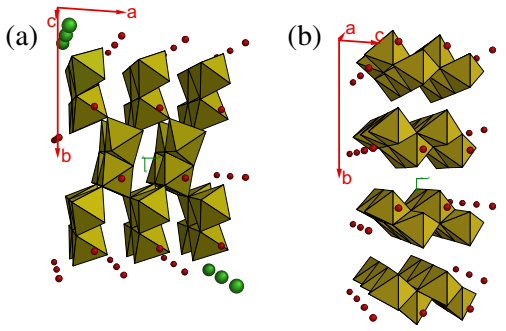

Fig.1 Crystal structures of (a)α-FeOOH and (b)γ-FeOOH.

Experiments

Fe-5 mass % Cr alloy (CR) were prepared and corrodes in sea water and in air for different periods. Rusts formed on the steel surface were analyzed by XAFS, XRD and TEM. Colloidal rusts, which was formed at the sample surface in seawater for several days, were analyzed by a special XAFS cell for a liquid sample. XAFS spectra of rusts formed on the sample surface exposed for a long time were measured in the reflection geometry using a 19-element SSD[1]. XAFS measurement were carried out at BL-12C at PF, KEK, Tsukuba, Japan.

Results and Discussion

Figure 2 shows radial distribution functions (RDF) of rusts formed on the surface under different conditions: 1) CR2W(WET): the colloidal rust formed after corrosion for 2 weeks in seawater, 2) CR2W(DRY): the dried rust of 1), and 3) CR15Y: the rust formed on the CR surface exposed to air indoors for 15 years. The RDF for crystalline α-FeOOH is also shown in Fig.2. The first peaks located at about 0.15 nm in the RDF's are attributed to the first nearest neighbor (1st NN) correlation of Fe-O. The peaks at about 0.27 and 0.32 nm in RDF's correspond to 2nd NN and 3rd NN correlation of Fe-Fe and Fe-O, respectively. As shown by the 1st NN peaks in all rust samples, the octahedron of $Fe(O,OH)_6$ units are formed in these rusts. However, the heights of the 2nd NN and the 3rd NN peaks in the rusts are weaker than those in α-FeOOH. This suggests that the periodic arrangement of $Fe(O,OH)_6$ units is slightly disordered, compared to that of crystalline α-FeOOH having a long-range order.

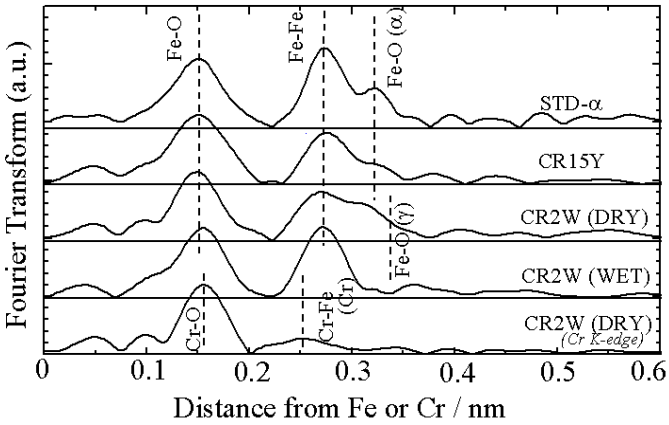

Fig.2 RDF around Fe and Cr of the rusts.

Small but significant differences among these samples were found in the 3rd NN peak region; the 3rd NN peak height in CR15Y is higher than that in CR2W(DRY) and CR2W(WET). In addition, the 3rd NN peak positions in CR2W(WET) and CR2W(DRY) seem to be close to that in γ-FeOOH, while the 3rd NN peak position of CR15Y is near that in α-FeOOH. These results suggest that the $Fe(O,OH)_6$ network of the rust changes depending on corrosion conditions such as its atmosphere and exposing time.

RDF around Cr shows a significant difference. The position of the 2nd NN peak is about 11% shorter than that of around Fe, indicating that Cr occupies a different site in the $Fe(O,OH)_6$ network in the rust.

Additional elements are expected to cause slight but significant differences in evolution of the $Fe(O,OH)_6$ network during corrosion, resulting in different morphology at the final stage. [2].

We would like to thank Profs. M. Nomura and T. Matsushita at PF for their great supports for experiments.

References

[1] M. Nomura: J. Synchrotron Rad., **5,** 851 (1998).
[2] M. Kimura et al: J. Japan Inst. Metals, **66,** 166 (2002).

* kimura@re.nsc.co.jp

15A/2001C006

In-situ observation of heat/draw deformation behavior of *isotactic* polypropylenes by SAXS measurements

Takashi SAKURAI[1*], Tatsuya KASAHARA[1], Noboru YAMAGUCHI[1], Kohji TASHIRO[2] and Yoshiyuki AMEMIYA[3]

[1]Petrochemicals Research Laboratory, Sumitomo Chemical Co., Ltd., 2-1 Kitasode Sodegaura City, Chiba 299-0295, Japan

[2]Graduate School of Science, Osaka University, Toyonaka City, Osaka 560-0043, Japan

[3]Graduate School of Frontier Sciences, Univ. of Tokyo, Hongo, Bunkyo, Tokyo 113-8656, Japan

Introduction

It is well known that the drawability of *isotactic* polypropylene (iPP) is affected significantly by various factors such as drawing temperature, microtacticity and sample molecular weight (MW). Among these factors, the effect of the MW distribution (MWD) on the drawability has not yet been well understood.

The purpose of this study is to examine the effects of MWD and MW on the drawability during heating and drawing process. The structural changes during the heating/drawing process of iPP with different MWD have been investigated by using small-angle X-ray scattering (SAXS) technique.

Experimental

Three types of samples were used, i.e., iPP polymerized by conventional Ziegler catalysts (zPP), the fraction insoluble in boiling heptane (BHIS) and the fraction insoluble in boiling octane (BOIS). They are different in MWD, MD and microtacticity.

The samples were cut from the sheet and shaped to the dimensions shown in Figure 1. The specimen was uniaxially stretched with a strain rate of 20 mm/min at 393K. The draw ratio (DR) was determined from the separation of marks put on the specimen.

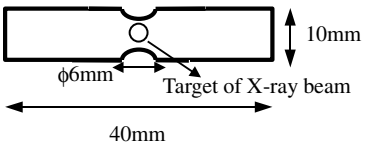

Fig.1 Dimensions of specimen

The SAXS measurements were conducted at the BL-15A beam line. For tracing the structural change in the specimen during drawing, time-resolved two-dimensional (2D) SAXS patterns were measured with 2-sec time slices by using a CCD X-ray detector [1,2].

Results and Discussion

Figure 2 shows 2D SAXS patterns of zPP and BOIS at DR=6. The 2D SAXS pattern of the zPP exhibited a two-bar pattern with the scattering maximum on the meridian and the streak-like pattern on the equator. Different from the case of zPP, the equatorial scattering of BHIS was found to become weaker in intensity with increasing DR. In case of BOIS, the equatorial scattering pattern was found to disappear with drawing.

Figure 3 shows the changes of the long period as a function of draw ratio. The long period increased linearly with the draw ratio, and this increasing rate was in order of zPP < BHIS < BOIS.

These experimental results suggest that the deformation behavior, which causes an increase in stress during the heating/drawing process, depends on MWD and microtacticity of the sample.

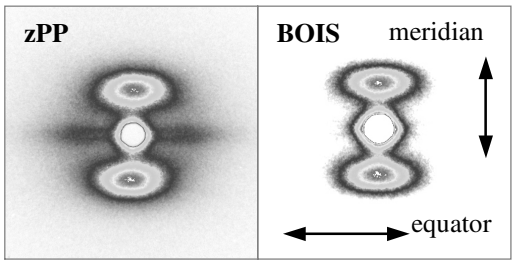

Fig.2 2D SAXS patterns of zPP and BOIS. Drawing rate =6.0

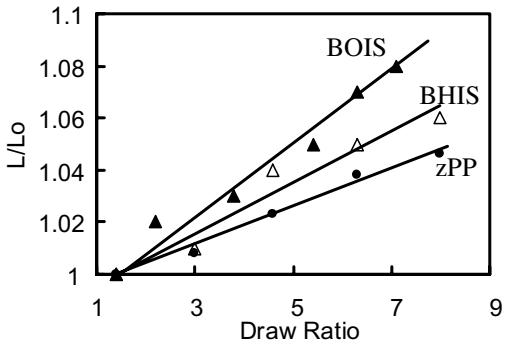

Fig.3 Changes of the long period as a function of draw ratio.

References

[1] Y. Amemiya et al., *Rev. Sci. Instrum.* **66**, 2290 (1995).

[2] K. Ito et al., Jpn. J. *Synchrotron Rad.* Vol.13, No.5, 372 (2000).

* sakurait2@sc.sumitomo-chem.co.jp